LA-UR-90-4355

C.1

Title: Performance of the LANSCE-WNR Facility as an Intense Pulsed Neutron Source for Neutron Nuclear Physics

Author(s): A. F. Michaudon and S. A. Wender

TABLE OF CONTENTS

PERFORMANCE OF THE LANSCE-WNR FACILITY AS AN INTENSE PULSED NEUTRON SOURCE FOR NEUTRON NUCLEAR PHYSICS

A. F. Michaudon and S. A. Wender

ABSTRACT

The Los Alamos Meson Physics Facility (LAMPF), which was built for medium-energy physics experiments, can also take advantage of its beam of 800-MeV hydrogen negative ions for the production of intense neutron beams. This is the reason why part of the LAMPF beam of hydrogen negative ions is now used for neutron production at the Weapons Nuclear Research (WNR) facility and at the Manuel Lujan, Jr. Neutron Scattering Center (LANSCE) in conjunction with a proton storage ring (PSR). This report focuses attention on the performance of the LANSCE-WNR facility for neutron nuclear physics from 1 eV to 800 MeV. Comparison is also made with the Oak Ridge Electron Linear Accelerator (ORELA), which is another facility used essentially for neutron-nuclear physics. Whereas LANSCE and WNR provide higher neutron fluxes than ORELA at the lower and higher ends of the 1-eV to 800-MeV energy range, respectively, the opposite situation prevails in the middle of this range. Proposals to upgrade LANSCE and WNR, using the same LAMPF beam, are put forward. If these proposals were implemented, the LANSCE-WNR facility would surpass all the other neutron-nuclear-physics facilities in the world by several orders of magnitude over the entire 1-eV to 800-MeV energy range.

I. INTRODUCTION

Neutrons, unlike protons or electrons, can only be produced by means of nuclear reactions. Spallation reactions induced by high-energy protons play a special role in the production of intense neutron beams because, for a given neutron output, they require less energy dissipation in the target than other reactions. Thus, the Los Alamos Meson Physics Facility (LAMPF),[1] which accelerates high-current proton beams up to 800 MeV and was initially built for

medium-energy physics experiments, can also be used for the production of intense neutron beams. For this reason, after the initial construction of LAMPF, part of its beam of hydrogen negative ions (H^-) was used for neutron production, first at the Weapons Nuclear Research (WNR) facility and then at the Manuel Lujan, Jr. Neutron Scattering Center (LANSCE) in conjunction with a proton storage ring (PSR).

The LANSCE-WNR facility[2] is a very versatile, multipurpose, intense pulsed neutron source. Most experiments are carried out at low energies (below 1 eV) at LANSCE in the field of condensed-matter physics. This report focuses attention only on the performance of LANSCE-WNR for neutron-nuclear physics above thermal neutron energies. This encompasses a wide energy range of about nine decades, from 1 eV to almost 800 MeV.

A brief description of LAMPF, LANSCE, and WNR is first presented in this report together with that of the Oak Ridge Electron Linear Accelerator (ORELA),[3] which is another intense pulsed neutron source that uses neutron-producing reactions induced by an electron beam (Chapter II). The principles of neutron time-of-flight (TOF) spectroscopy are then summarized because this method is extensively used at LANSCE-WNR and ORELA for neutron nuclear physics (Chapter III). These principles provide the background for calculations of the neutron flux as a function of energy produced at these facilities under different conditions of experimental resolution (Chapter IV). Some conclusions are drawn from these calculations, and proposals for improvements to the LANSCE-WNR facility are given (Chapter V). The interest in using a lead slowing-down spectrometer with the proton beam produced by the PSR is also discussed in Chapter V. Finally, a general conclusion is presented in Chapter VI.

The information about these facilities, quoted and used in this report, is sometimes approximate because the few reliable figures available are not often given in publications. Sometimes, pieces of information were not consistent with one another and had to be slightly altered to obtain a consistent set of values. An additional complication results from facility modifications that were not adequately documented.

The results obtained in this report should therefore be considered as a starting point for further studies. Any new information can easily be fed into the programs used for the calculations presented in Chapter IV. These results can thus be updated at any time. However, any future modifications should not greatly alter the conclusions of the present study.

II. GENERAL DESCRIPTION OF THE LANSCE, WNR, AND ORELA FACILITIES

A. Introduction

This section starts with the description of LAMPF, where a H^- beam is accelerated to 800 MeV before it is used for neutron production. The extraction of this H^- beam from LAMPF is then described together with its transport to LANSCE (with time compression in the PSR) and to WNR. The time structure of the charged-particle beam impinging on the targets is given for both facilities with a description of the target-moderator systems used for neutron production. Finally, the layout of the flight paths extending away from the targets is briefly sketched. For completeness, a similar description is also given for ORELA.

B. LAMPF

The LAMPF linear accelerator (linac) is a versatile machine that can accelerate, simultaneously or independently, pulsed beams of protons (H^+) and negative hydrogen ions, whether unpolarized (H^-) or polarized (P^-), with various energies and time structures. Each pulse (described below) may consist of one of these three ion species, or of two of them, provided they have opposite charges. This means that beams of H^- and P^- cannot be accelerated together in the same pulse.

The ion source injection energy is 750 keV. Following the ion source, the beam is chopped and bunched into the phase acceptance of the linac. The beam is then accelerated to 100 MeV in the 62-m-long, 201-MHz drift-tube section. This section is followed by a side-coupled-cavity section, operating at 805 MHz, which produces the final acceleration of the beam whose energy can be varied from one pulse to the other with a maximum of 800 MeV.

The maximum average current that can be obtained is approximately 1 mA for the proton beam. The current of the H^- beam is limited to a lower value when it is accelerated simultaneously with 1 mA of proton beam. Both the LANSCE and the WNR targets use a H^- beam of 800 MeV.

The time structure of the LAMPF beam presently consists of 625-μs* pulses (called macropulses) at a repetition rate of 120 Hz. Each macropulse is composed either of protons, associated or not with negative ions, or of negative ions alone. Within each macropulse are micropulses that are less than 100 ps wide. There are

---

* now 825-μs (October 1990).

approximately 10^8 to 2×10^8 protons in a micropulse; we shall assume 10^8 protons per micropulse in the following. The smallest micropulse spacing is 5 ns, which corresponds to the basic frequency of the linac. This is the so-called unchopped beam mode, in contrast with the chopped beam mode in which the separation between micropulses may be increased, as discussed below.

The distribution of beam to the various LAMPF experimental areas is sketched in Fig. 1. Following acceleration, the protons are separated from the negative ions with a permanent magnet. The high-current proton beam is transported to area "A" for pion production. The negative ions are transported either to line "D" where they are used to feed the neutron production sources (LANSCE and WNR) or to line "X" where they are used for medium-energy nuclear physics studies. A "switchyard" kicker magnet deflects the beam to line "D" when it is pulsed on. The negative ions go directly to line "X" when the "switchyard" kicker is not activated. Presently, this kicker magnet is limited to a maximum of 60 pulses per second with no adjacent pulses closer than 16.7 ms, but there is no fundamental limitation to upgrade this kicker magnet and to increase its pulse rate up to 120 pulses per second, if necessary.

The LAMPF linac can accelerate successive macropulses of different energies (up to 800 MeV). Only 800-MeV macropulses can be transported to area "A," the PSR and the WNR, whereas line "X" can accommodate negative-ion macropulses of different energies at 800 MeV and below, depending on the experimental requirements. Another mode of operation, which involves proton beam energies below 800 MeV, is possible at the WNR but is not considered here. We describe below the most usual operation of LAMPF.

The PSR uses H^- unchopped macropulses at a rate of 20 Hz. No associated proton macropulses are transported to area "A" because of beam loading considerations. The distribution of the remaining 100 H^- macropulses per second between line "D" and line "X" depends on the energy used by line "X" and on the capability of the switchyard kicker.

When line "X" is operated at 800 MeV, these 100 negative-ion macropulses per second are divided between the line "X" and the WNR by the "switchyard" kicker. The 100 proton macropulses per second that are associated with these negative-ion ones are transported to line "A."

When line "X" is operated below 800 MeV ("off-energy" operation), the proton macropulses associated with line "X" negative-ion macropulses cannot be transported to area "A" because they have an energy different from 800 MeV. But the other H^- macropulses of

800 MeV, not used by line "X," can be transported to WNR through the switchyard kicker. When 800-MeV-chopped H^- macropulses are used by WNR, the associated proton macropulses can be transported to area "A".

In all cases, the maximum macropulse rate now available to line "D" is 60 Hz, as limited by the switchyard kicker. In these conditions, the maximum macropulse rate left to WNR is 40 Hz when LANSCE is operated at its maximum rate of 20 Hz. This value of 40 Hz will be used in this paper, but it is known that it could be increased by an improvement of the switchyard kicker.

C. LANSCE

1. Beam transport

The LANSCE target area[4] is designed for thermal and epithermal neutron production. When the Ring Injection Kicker is energized, the H^- beam is injected in the PSR where it is stripped to a H^+ beam and compressed in time. When the magnet is switched off, the beam is transported through the "bypass" beam line to the WNR target area.

2. Time structure of the proton beam

For PSR operation, a 450-μs H^- macropulse, containing micropulses spaced every 5 ns, is injected into the PSR. This macropulse is chopped at the injection end of the accelerator to produce a 90-ns gap every 360 ns (the circulation time for the beam in the PSR). The macropulse is wrapped around the PSR until at the end of the macropulse, the accumulated contents of the PSR is transported to the neutron-production target.

Presently, the PSR produces pulses at a rate of 20 Hz. The shape of the proton burst ejected from the PSR is approximately an isosceles triangle, with a base width of 250 ns. With these operating parameters, the average beam current to the LANSCE target is approximately 60 μA.**

3. Target-moderator system

The LANSCE target[4] has been designed to optimize thermal and epithermal neutron production and to reduce the contribution of high-energy neutrons. The spallation neutrons are produced following bombardment of two tungsten targets situated one after the other along the vertical proton beam coming from the PSR. These

** now 80 μA (October 1990).

two tungsten targets have a diameter of 20 cm and a length of 7 cm (27 cm) for the upper (lower) target. They are separated by a 14-cm void, which is surrounded by moderators and reflectors. The reflector system consists of beryllium and nickel. The flight paths face the moderators, which are located at the level of the void region between these two targets to minimize the transport of high-energy neutrons. The moderating material is water for those flight paths used for neutron-nuclear physics. The neutron-production target is surrounded by a cylindrical biological shield of 7 m in outer radius.

4. Flight paths

Figure 2 shows the general layout of the LANSCE production target and its associated flight paths. The length of the flight paths dedicated to nuclear physics ranges from approximately 7 to 55 m.

D. WNR

1. Beam transport

Those macropulses transported through line "D" and not injected into the PSR are transported to the WNR, with a maximum rate of 40 Hz, through the bypass beam line where they are stripped to H^+ before bombarding the WNR target (called target 4 in Fig. 1).

2. Time structure of the proton beam

For TOF experiments, it is necessary to have widely spaced microbursts (see Chapter III).

In one mode of operation, the beam from the ion source is chopped into an approximately 20-ns pulse before injection into the accelerator. This 20-ns pulse, which contains approximately 3×10^8 protons, is bunched into the phase acceptance of the linac. The time between such micropulses can be set in increments of 360 ns, but this increment can be modified if necessary (see Sec. V.D). Typical micropulse spacings are 1.8 μs. In this case, because the acceptance of the linac is only 20 ns per micropulse, only 20 ns per 1.8 μs (≃ 1%) of the ion source is used, with each micropulse containing 3×10^8 protons.

In another operating mode, which is more useful for obtaining long proton burst widths, the buncher is not used. In this case, the proton beam consists of a train of micropulses (of 10^8 protons per micropulse) separated by 5 ns. The length of the pulse train depends on the chopper width, which is adjustable. The time between these pulse trains is adjustable in increments of 360 ns.

These beam conditions are shown graphically in Fig. 3.

3. Target-moderator system

The WNR target area is designed for high-energy neutron production from below 1 MeV to over 400 MeV. The neutrons are produced in spallation reactions following bombardment of the target by the 800-MeV proton beam. The energy spectrum of neutrons is continuous, and the TOF technique is used to determine the energy of the incident neutron.

The neutron-production target presently consists of a tungsten cylinder, 7.5 cm long and 3 cm in diameter, with a thin water-cooling jacket surrounding it. This target length corresponds to a 200-MeV loss of the incident proton beam. The shape of the neutron spectrum depends on the angle of the neutron beam with respect to the proton beam. Greater intensities are obtained at forward angles. The neutron-production target is located inside a 2-m-diam, 1-m-high vacuum chamber. This vacuum chamber is surrounded by a massive shield consisting of steel balls and magnetite concrete. The average density of this shielding material is approximately 5.6 g/cm^3. Penetrations allow neutrons to go through the shield at angles of ± 90°, ± 30°, ±15°, and 60°. These holes are closed with mechanical shutters that allow for independent control of each flight path.

4. Flight paths

Figure 4 shows the layout of the experimental yard. Table 1 lists the characteristics of the various neutron flight paths that are available at the WNR. These flight paths are all above ground and have lengths ranging from 8 to 90 m.

E. ORELA

1. Linear accelerator

At ORELA, the neutrons are produced from bursts of electrons that are first extracted from a cathode and preaccelerated by a 120-kV gun before they are fully accelerated in a traveling-wave linac. The radio frequency (rf) of this wave is f_{rf} = 1,300 MHz (in the so-called L-band), and the power is fed into the accelerating guide by four klystrons that provide a total peak power of 96 MW with a time average of 270 kW. After the electrons are injected in the accelerating guide by the gun, they are bunched in short micropulses, micropulses are then accelerated by the traveling electric field over a length of 16.5 m to a maximum energy of 140

MeV. These micropulses are taken together over a time gate width Δt_b set by the electron gun to form a burst. The linac operates in the "stored-energy" mode with an rf filling time of 1.85 μs and a maximum electron peak current in the burst of 15 A. The average electron beam power cannot exceed 50 kW.[3]

TABLE 1

CHARACTERISTICS OF WNR FLIGHT PATHS

Angle[a] (degrees)	Maximum Length (m)	Present Experimental Program
90° L	10	(n,α), (n,p), ...reactions.
30° L	40	High-resolution gamma-ray studies, total cross sections.
15° L	90	High-energy (n,p) reaction studies.
15° R	18	High-energy gamma rays.
30° R	40	Weapons-related detector studies. (To be implemented in FY 91).
60° R	20	Fission physics.
90° R	8	Facility neutron monitor.

[a]The angle is given relative to the direction of the incident proton beam. The letters L and R mean at the left or at the right of the traveling incident proton beam, respectively.

2. Time structure of the electron beam

The electron beam of ORELA consists of a series of bursts having a time width Δt_b and a repetition frequency f_b. Each burst consists of microbursts having a time width of 70 ps separated by 0.77 ns (Fig. 3). No further use is made of the fine structure of these microbursts after their acceleration.

The time width Δt_b can be varied between 2 and 1,000 ns, but as a consequence of the "stored-energy" mode of operation of the linac, no more energy can be fed into the electron bursts for time widths greater than 24 ns. Therefore, for TOF spectroscopy that requires short bursts (as explained in Chapter III), only burst widths equal to or shorter than 24 ns are considered.

The peak power P_e (in joules per nanosecond) in the electron beam during a burst (averaged over the microstructure) is plotted as a function of the burst time width Δt_b in Fig. 5. This graph is an adaptation of a curve supplied by Oak Ridge National Laboratory (ORNL),[5] modified between 12 ns and 24 ns to obtain a full energy of $J_b = 50$ J at $\Delta t_b = 24$ ns. Below about 4 ns, these results are probably not very reliable. Facilitating the calculations required an approximation of the power P_e as follows:

$$P_e = \frac{47}{12} - \frac{11 \times \Delta t_b}{144}, \qquad \text{for } 24 \text{ ns} > \Delta t_b > 12 \text{ ns}; \qquad (1)$$

$$P_e = 3, \qquad \text{for } 12 \text{ ns} > \Delta t_b > 4 \text{ ns; and}$$

$$P_e = \frac{3 \times \Delta t_b}{4}, \qquad \text{for } 4 \text{ ns} > \Delta t_b > 2 \text{ ns},$$

where P_e is expressed in joules per nanosecond, and Δt_b is expressed in nanoseconds.

The repetition frequency f_b can be varied between 5 and 1,000 Hz, and the maximum average power of 50 kW is reached with 24-ns bursts at $f_b = 1{,}000$ Hz.

3. Target-moderator system

Two targets are possible at ORELA: a tantalum-water target, which is used most of the time, and a beryllium target, which is used occasionally for high-energy neutrons.[6]

The tantalum-water target, which consists in a stack of 0.07- to 0.266-in.-thick tantalum plates, produces an intense beam of bremsstrahlung when bombarded by the electron beam. These gamma rays produce fast neutrons in the same tantalum plates via (γ,n) reactions, and the energy spectrum of these neutrons has a Maxwellian-type shape with a mean energy of about 1 MeV. The large power of the electron beam is dissipated in a small volume of the tantalum plates where it is removed by a flow of water circulating through these plates. At the same time, this water serves also to moderate most of the fast neutrons down to thermal and

epithermal energies. Both the fast neutrons and the moderated neutrons can be used in TOF spectroscopy.

For high-energy neutron production a large block of beryllium metal is preferred to the tantalum target because of its greater neutron yield at high energy. The neutron yield is also increased by inserting a thin tantalum converter in front of the beryllium block to more efficiently convert the electron beam energy into bremsstrahlung.

In addition to the production of the neutrons, ORELA also emits an intense burst of bremsstrahlung gamma rays (a gamma flash) at the time the electron beam hits the target. This parasitic gamma flash can create serious difficulties for some experiments (for example, when they are based on gamma-ray detection).

4. Flight paths

The neutron-producing target is surrounded by a concrete bunker for biological shielding. Several holes used for viewing this target from the detectors located outside the bunker are bored into this shielding. In total, the facility comprises 10 evacuated flight paths (most of them are underground) with 18 measurement stations. The maximum flight-path length is 200 m and the minimum length imposed by the bunker is 8.9 m.[3]

A general layout of the ORELA facility is given in Fig. 6.

F. Summary

It is interesting to summarize the maximum intensity of the fast neutrons and the time structure of the charged-particle beams produced by these facilities.

The maximum average fast-neutron production rate is

- 10^{14} neutrons s^{-1} at ORELA, at a full power of 50 kW, and

- $1.25 \times 10^5 \times 10^8 \times 40 \times 15 = 7.5 \times 10^{15}$ neutrons s^{-1} at WNR. (This production rate is based on the assumption, hypothetical at the present time, that the 625-μs macrobursts consist of 1.25×10^5 microbursts of 10^8 protons each in the unbunched mode, at a repetition frequency of 40 Hz, and with a yield of 15 neutrons per incident proton.)

The maximum average fast-neutron production rate is

- $6.25 \times 10^{18} \times 60 \times 10^{-6} \times 15 = 5.6 \times 10^{15}$ neutrons s^{-1} at LANSCE. (This production rate assumes an average proton current of 60 μA and a similar yield of 15 neutrons per incident proton.)

Therefore, LANSCE and WNR are clearly superior to ORELA by factors of 56 and 75, respectively, as far as the average fast-neutron production rate is concerned.

A neutron intensity as high as 10^{17} neutrons s^{-1} would be obtained with the full 1-mA LAMPF beam, about 10^3 times more intense than that of ORELA.

The time structure can be described, at least partially, by the duty cycles D_c averaged over any possible fine structure. They are quite different for these facilities:

- $D_c = 10^3 \times 24 \times 10^{-9} = 2.4 \times 10^{-5}$ for ORELA at the full power of 50 kW (24-ns bursts at f_b = 1,000 Hz),

- $D_c = 625 \times 10^{-6} \times 40 = 2.5\%$ for WNR (625-μs macrobursts at 40 Hz), and

- $D_c = 125 \times 10^{-9} \times 20 = 2.5 \times 10^{-6}$ for LANSCE (125-ns proton bursts at 20 Hz).

As we shall see later, the full beams of these facilities are not always utilized for neutron TOF, especially for WNR, which is not presently operated at this high duty cycle and therefore at this high neutron intensity because of the requirements of the TOF method and also because of some technical limitations. If it were, the loading of the H^- beam in the LAMPF linac would result in a reduction in the current of the associated proton beam. But its future possible use is nevertheless considered in Sec. V.D.

A low duty cycle is essential for a neutron TOF facility (see Chapter III). This is the case of ORELA, which was initially constructed for that purpose. The situation for the LANSCE-WNR facility is entirely different. LAMPF was initially constructed for experiments requiring, on the contrary, a high duty cycle. Therefore, though LAMPF has a higher neutron output than ORELA, it is penalized by its time structure, as discussed below. The situation was greatly improved by the construction of a PSR for LANSCE, which led to a low duty cycle, but this low duty cycle is matched to low-energy work by having a low repetition frequency and a broad proton pulse.

WNR, in the absence of a time-compression device, can improve its time structure by using only some of the microbursts and throwing away the other ones at the expense of average intensity. The consequences of these properties will be examined below.

III. FUNDAMENTALS OF NEUTRON TIME-OF-FLIGHT SPECTROSCOPY

A. Introduction

The neutron TOF method requires the use of a pulsed neutron source with a neutron energy spectrum that can be either monoenergetic or broadband as provided by the white neutron sources described above. In the latter case, the incident neutron energy is determined by the time it takes the neutron to traverse the distance (or flight-path length) between the neutron source and the detector. As explained below, the neutron TOF method is more efficient if the neutron source delivers neutron bursts as intense and short as possible. The repetition frequency of the neutron bursts must be as high as possible to increase the detector count rate, provided that the overlap at the detector position between neutrons of different bursts remains at a low level. Different methods (discussed in Chapter IV) can be used to reduce the effect of this neutron overlap.

B. Basic formulas

The neutron TOF can be derived from the basic relation between the kinetic energy E_n and the momentum p_n of the neutron. Because the energy range being considered is quite wide and covers energies that are not negligible compared with the neutron rest-mass energy $M_n c^2$, a relativistic treatment is necessary. This exact relativistic treatment is given in Appendix A and was used in the calculations. But the classical nonrelativistic expressions given in this section are accurate enough for the following discussions and will be used for that purpose unless stated otherwise.

From the expression

$$E_n = \frac{p_n^2}{2M_n}, \tag{2}$$

one obtains

$$\frac{t_n}{L} = \frac{1}{v_n} = \frac{1}{c} \times \sqrt{\frac{M_n c^2}{2E_n}} = \frac{72.298}{\sqrt{E_n(eV)}} (\mu s/m), \tag{3}$$

where t_n is the neutron TOF over a distance L, v_n is the neutron velocity, and c is the velocity of light.

The energy spread ΔE_n associated with a time spread Δt_n is obtained by differentiating both sides of Eq. 3. One then obtains

$$\Delta E_n = 2c\sqrt{\frac{2}{M_n c^2}} \times E_n^{3/2} \times \frac{\Delta t_n}{L} = 0.02766 \times E_n^{3/2} \times \frac{\Delta t_n}{L}, \qquad (4)$$

where ΔE_n and E_n are in eV, and $\frac{\Delta t_n}{L}$ is in microseconds per meter.

This expression shows that the energy spread ΔE_n at a given energy E_n depends only on the ratio $R = (\frac{\Delta t_n}{L})$, called the nominal resolution, which is generally used to define the resolution of a neutron TOF spectrometer.

If the neutron emission at the source at a given energy E_n is $N_b(E_n)$ n/b/eV/sr (neutrons per burst, per eV, and per steradian), then the neutron flux Φ_n at the detector position is

$$\Phi_n = 10^{-4} \times \frac{N_b}{L^2} \times f_b \ (n/cm^2/s/eV), \qquad (5)$$

where L is expressed in meters and f_b is the number of bursts per second.

For a given nominal resolution R, the neutron flux is therefore given by the following expression:

$$\Phi_n = 10^{-4} \times R^2 \times [\frac{N_b \times f_b}{(\Delta t_n)^2}] \ (n/cm^2/s/eV) \qquad (6)$$

and is determined entirely by the quantity $A = [\frac{N_b \times f_b}{(\Delta t_n)^2}]$, which shows why short bursts are important for obtaining high neutron fluxes.

The exact gain in using short bursts depends on the variations of N_b and f_b with Δt_n. There are no general rules and these variations have to be studied case by case. Also the time resolution Δt_n is a combination of the charged-particle burst time width Δt_b and the neutron time spread Δt_{tm} in the target-moderator system as discussed in Sec. III.C. The neutron production N_b varies with Δt_b in a way that depends on the accelerator and on the value for Δt_b. The variation of N_b with Δt_n is even more complicated. The repetition frequency f_b is also influenced by the choice of Δt_n, because for a

given nominal resolution R, any change in Δt_n is automatically reflected in a similar change in L. In favorable cases, such as at low energy, f_b varies as 1/L, i.e., as $(1/\Delta t_n)$, until it reaches the maximum repetition frequency of the accelerator (see Sec. IV.C). In most cases, the quantity $A = [\frac{N_b \times f_b}{(\Delta t_n)^2}]$ increases with decreasing Δt_n, at best as rapidly as $(1/\Delta t_n)^3$.

In addition to an increased neutron flux, the use of shorter bursts leads to shorter flight paths and hence to a smaller size, a reduced cost, and an easier use of the TOF facility.

Therefore, the best neutron source for high-resolution TOF spectroscopy should provide very intense and short bursts at the highest possible repetition frequency compatible with the experiments to be performed.

C. Time resolution

A precise determination of the neutron TOF is essential for high-resolution measurements. Time uncertainties occur at two levels: (1) at the neutron source and (2) at the detector (including the channel width of the TOF analysis). Here, we consider the time uncertainties at the source level only and ignore them at the detector level. We also ignore the distance uncertainties, including the possible inclination of the flight path relative to the normal to the moderator (discussed in Sec. IV.G.5). All of these uncertainties should be taken into account when determining the overall resolution function of an experiment.

At the source, the time resolution is made up of three components: (1) the shape and the width of the charged-particle burst, (2) the time spread of the charged particles in the target as they induce the neutron-producing nuclear reactions, and (3) the time spread of the neutrons inside the target-moderator system before they leave the exit plane of this system. The nuclear-reaction times are usually much shorter than all these time uncertainties and can therefore be neglected.

Each of these effects has a time distribution (or time resolution) and the overall time resolution function at the source is obtained by convoluting all of these resolution functions with each other. Each resolution function i has a standard deviation σ_i, and the standard deviation σ_t of the overall resolution function at the source level is the square root of the quadratic combination of the standard deviations σ_i of these resolution functions. The shape of the overall resolution function depends on the shapes of these individual

resolution functions. If they are all Gaussian, the overall shape is also Gaussian. If they are not Gaussian, the overall shape has to be calculated by the operation of convolution. Unless one of the individual resolution functions is very asymmetric, e.g., with a long tail, the shape of the overall resolution function is usually assumed to be Gaussian.

Traditionally, neutron spectroscopists express the width of the resolution function not in terms of its standard deviation σ_E but rather in terms of its full width at half maximum (FWHM), which is a source of ambiguity because the exact shape of the resolution function is usually not known, and, consequently, the relation between the FWHM and σ cannot be determined. If that shape is taken to be Gaussian, as is generally assumed, then FWHM = 2.35 × σ_E.

D. Doppler effect

Another source of uncertainty in TOF measurements comes from the thermal motion of the atoms in the sample. This motion can be increased or reduced by raising or lowering the sample temperature, but it can never be suppressed even when cooling the sample to very low temperatures. In most cases, especially at room temperature, this motion plays a role similar to that of a resolution function, is called Doppler broadening, and has a Gaussian shape of standard deviation σ_D given by the following relation:

$$\sigma_D = \sqrt{\frac{2E_n \times k_B \times T_{eff}}{A}}, \qquad (7)$$

where k_B is the Boltzmann constant, T_{eff} is the effective temperature of the sample,[7] and A is the mass number of the struck nucleus.

The value of T_{eff} is a function of the actual temperature T and of the phonon spectrum of the sample. For most samples at room temperature, T_{eff} is very close to T. Therefore, for the sake of simplicity, we assume in this report that T_{eff} = T.

Traditionally, neutron spectroscopists express the Doppler broadening in terms of a so-called "Doppler width" Δ, which is defined as $\Delta = \sigma_D \times \sqrt{2}$.

In Chapter IV, we use $\sigma_D = 0.0227 \times \sqrt{E_n}$ (also for the sake of simplicity), which is calculated at room temperature for a medium-mass nucleus (T_{eff} = T = 300 K and A = 100).

IV. PERFORMANCE OF THE LANSCE-WNR FACILITY: COMPARISON WITH ORELA

A. Introduction

There is no universal way to describe the performance of a neutron TOF facility. It is also difficult and controversial to compare two facilities even if they are used for similar experiments because comparisons, like the performances, depend on the nature of the experiments. There is a great variety of experiments with several techniques possible for the same measurement. Yet, the difficulty of the task should not prevent us from attempting to approach this problem in a broad manner. It is not our intention here to try to tackle one specific experiment but rather to provide a base that may be useful in assessing the merit of a neutron TOF facility. In doing so, we expect that the results obtained represent a kind of gross average over a large number of different experiments.

In this context it seems that a useful figure to know is the neutron flux at the detector position, irrespective of the experiment, as a function of neutron energy and for a given resolution.

The choice of the resolution function is a delicate matter because it can easily change the performance of a facility or the comparison between facilities or even render some experiments impossible. For this reason, "realistic" resolution profiles, defined as the variations of ΔE_n (or the standard deviation σ_E) with E_n, are proposed and discussed in Sec. IV.B. Though some arbitrariness in setting such profiles always exists, they still are very useful in mapping the possibilities of neutron TOF facilities. The principles of the calculations of the neutron flux versus neutron energy for the resolution profiles defined previously are explained in Sec. IV.C. The results of these calculations are given in Secs. IV.D-IV.F and discussed in Sec. IV.G. Possibilities for upgrading LANSCE and WNR are given in Chapter V, with relevant calculations obtained in the same manner.

B. Resolution profiles

In order to determine the resolution that is needed in a neutron-physics experiment, the shape of a typical neutron cross section for a medium-mass or heavy nucleus must be considered.

At very low energy (thermal energies or just above) the cross section decreases steadily with increasing E_n. At higher energy, up to a value that varies from nucleus to nucleus but is typically of the order of a few hundreds of eV to a few keV, the cross section consists of sharp and well-separated resonances. At higher energies, the

resonances start to overlap each other because their natural width Γ increases with energy independently of the experimental conditions. But, the experimental resolution and the Doppler effect, both of which increase with neutron energy, also broaden the measured resonances. This is the region of overlapping resonances where these resonances can no longer be separated but rather where their overlap increases with neutron energy, resulting in smaller and smaller fluctuations of the cross section. At higher energy, the cross section becomes smooth and level; this is the continuum region.

The behavior of such a cross section and the variation of the energy resolution with neutron energy are guidelines for the definition of resolution profiles (RPs). In the following, we make the distinction between high-resolution and coarse-resolution measurements.

1. High resolution

At the low-energy end, in the region of well-separated resonances, the resolution function has to be compared with the natural widths Γ of these resonances and with the Doppler broadening. Extracting the resonance parameters, e.g., by a shape analysis of these resonances, requires a width smaller than the natural width Γ for both the resolution function and Doppler broadening. But there is no need for the resolution function to be much narrower than the Doppler broadening. Therefore, in this energy region, one can assume that resonance analysis requires

$$\sigma_E = 0.3 \times \sigma_D \simeq 6.8 \times 10^{-3} \times E_n^{\frac{1}{2}}, \qquad (8)$$

where σ_E is the standard deviation of the energy resolution function. Both σ_E and E_n are expressed in eV.

This means that the contribution of the resolution function is only about 10% in the overall quadratic combination of the resolution function and the Doppler broadening.

This requirement can easily be met at low energies but becomes more and more stringent with increasing energies because, as a consequence of Eq. 4, the condition (Eq. 8) results in the following relation for the nominal resolution (σ_t/L):

$$\frac{\sigma_t(\mu s)}{L(m)} = \frac{0.246}{E_n(eV)}. \qquad (9)$$

In this energy region, the neutrons need to be moderated, and for most spectrometers, the time resolution is dominated by the moderation time, with a typical $\sigma_t(\mu s)$ value of about $0.8\sqrt{E_n(eV)}$. The flight-path length that is needed for the measurement then is

$$L(m) = 3.24 \times \sqrt{E_n(eV)} . \qquad (10)$$

With a flight path of 100 m, this means that the condition (Eq. 8) cannot be met above about 1 keV.

Above this energy and for most cases, the time resolution is still dominated by the moderation time until it becomes comparable with or smaller than the minimum charged-particle width Δt_b. On the other hand, the length of the flight path cannot usually be extended beyond a few hundred meters. Therefore, in this energy region, a reasonable resolution profile can be obtained by choosing $\sigma_t(\mu s) = 0.8\sqrt{E_n(eV)}$, as before, and L = 100 m. When these values are inserted in (Eq. 4), one obtains

$$\sigma_E \simeq 2 \times 10^{-4} \times E_n. \qquad (11)$$

At higher energies (in the continuum region), the time resolution is no longer limited by the moderation time but rather by the minimum duration of the charged-particle burst, which is typically about 1 ns (σ_t = 0.42 ns for a Gaussian shape). High-resolution measurements can be made with flight-path lengths of about 100 m. This leads to a nominal resolution of about 0.01 ns/m. Once the values for σ_t and L are inserted in Eq. 4, one obtains

$$\sigma_E \simeq 10^{-7} \times E_n^{3/2}. \qquad (12)$$

Therefore, this high-resolution profile consists of three energy regions:

(1) *at low energy*, in the resolved-resonance region,

$$\sigma_E \simeq 6.8 \times 10^{-3} \times E_n^{1/2};$$

(2) *at intermediate energy*, in the unresolved-resonance region,

$$\sigma_E \simeq 2 \times 10^{-4} \times E_n; \text{ and}$$

(3) *at high energy*, in the continuum region,

$$\sigma_E \simeq 10^{-7} \times E_n^{3/2}.$$

This profile can be written as one single formula over the whole energy range:

$$\sigma_E = \mathrm{MAX}(6.8 \times 10^{-3} \times E_n^{1/2},\ 2 \times 10^{-4} \times E_n,\ 10^{-7} \times E_n^{3/2}). \qquad (13)$$

2. Coarse resolution

In the same manner as above, it is possible to define a resolution profile for measurements made with a coarse resolution.

At low energy, in contrast with the high-resolution case, these measurements are not made to determine resonance parameters. The goal is rather to measure compound-nucleus decay properties in the resonances such as, for example, capture gamma-ray cascades or fission fragments. For these measurements with low count rates, the neutron flux is more important than the resolution. A resolution width smaller than the Doppler width is not necessary. On the contrary, one can tolerate a resolution width greater than the Doppler width to increase the neutron flux. The amount to which the resolution width can be increased is of course debatable and varies case by case. In the absence of specific information, we assume in the following that the resolution width can be three times greater than the Doppler width, i.e., ten times bigger than for the high-resolution case.

For the other energy regions, we assume, in the same manner, that the resolution function is ten times wider than for the high-resolution case.

The resolution profile over the entire energy region can then be written as

$$\sigma_E = \mathrm{MAX}(6.8 \times 10^{-2} \times E_n^{1/2},\ 2 \times 10^{-3} \times E_n,\ 10^{-6} \times E_n^{3/2}). \qquad (14)$$

These two resolution profiles, called RP1 and RP2 for high resolution and coarse resolution, respectively, are tabulated in Table 2 and plotted in Fig. 7.

Other resolution profiles could of course be defined depending on the experiment to be performed, but the two profiles defined above can already help assess the properties of neutron TOF spectrometers.

TABLE 2

WIDTHS OF THE RESOLUTION FUNCTIONS FOR RP1 AND RP2

E_n (eV)	σ_E[a] (eV) RP1	FWHM[b] (eV) RP1	σ_E[c] (eV) RP2	FWHM[d] (eV) RP2	σ_D[e] (eV)
1.00E+00	6.80E-03	1.60E-02	6.80E-02	1.60E-01	2.27E-02
1.00E+01	2.15E-02	5.05E-02	2.15E-01	5.05E-01	7.19E-02
1.00E+02	6.80E-02	1.60E-01	6.80E-01	1.60E+00	2.27E-01
1.00E+03	2.15E-01	5.05E-01	2.15E+00	5.05E+00	7.19E-01
1.00E+04	2.00E+00	4.70E+00	2.00E+01	4.70E+01	2.27E+00
1.00E+05	2.00E+01	4.70E+01	2.00E+02	4.70E+02	7.19E+00
1.00E+06	2.00E+02	4.70E+02	2.00E+03	4.70E+03	2.27E+01
1.00E+07	3.16E+03	7.43E+03	3.16E+04	7.43E+04	7.19E+01
1.00E+08	1.00E+05	2.35E+05	1.00E+06	2.35E+06	2.27E+02
1.00E+09	3.16E+06	7.43E+06	3.16E+07	7.43E+07	7.19E+02

[a]Standard deviation of the energy resolution function for RP1, as given by Eq. 13 in the text.

[b]FWHM of the same resolution function as in (a), supposing it is a Gaussian function.

[c]Standard deviation of the energy resolution function for RP2, as given by Eq. 14 in the text.

[d]FWHM of the same resolution function as in (c), supposing it is a Gaussian function.

[e]Standard deviation of the Doppler effect, as calculated with T_{eff} = 300 K and A = 100 (see Sec. III.D).

C. Principles of the calculations

The calculations carried out below assume that the measurements are made at 90^0 relative to the direction of the charged-particle beam. This provides the best experimental conditions because it minimizes the distance uncertainties at the source level. The effect of using neutron beams inclined relative to the normal to the charged-particle beam is discussed in Sec. IV.G.5.

In order to calculate the neutron flux at the detector position as a function of neutron energy and for a given resolution profile, the following procedure has been used for each energy value:

(1a) Note the standard deviation σ_{tm} of the neutron time spread in the target-moderator system assuming that the charged-particle burst is a δ–function in time.

(2a) Optimize, accordingly, the duration of the charged-particle burst whenever possible. For simplicity, the standard deviation, σ_b, of this burst is made equal to σ_{tm} within the possibilities of the accelerator, or shorter if there is no resulting loss in intensity.

(3a) Calculate the standard deviation σ_t of the overall time resolution function from the quadratic combination of σ_{tm} and of σ_b obtained in procedures (1a) and (2a) , respectively.

(4a) Determine the neutron output per burst, N_b, for the burst duration having σ_b for a standard deviation.

(5a) Calculate the necessary flight-path length, L, from the known values of σ_t and σ_E using Eq. 4. If the L value obtained is shorter than the minimum value L_m of the facility, then set L = L_m and make new calculations with a modified procedure (see below). No upper limit is fixed on L, but the values obtained with this method are discussed in Sec. IV.G.

(6a) Determine the number of bursts per second f_b. An upper limit is the maximum repetition rate f_M of the facility. But the value of f_b must also take into account the effect of neutron-frame overlap, which depends on the experiment to be performed. In the absence of specific information, we consider two general cases: (1) at low energy and (2) at high energy.

(1) *At low energy*, one can use the so-called filter method in which a slab of material having a cross section with a strong $1/v_n$ component is placed across the neutron beam. The thickness of the slab and the repetition frequency can be determined by imposing for example a 10% attenuation at energy E_n caused by the $(1/v_n)$ component for the neutrons from the last burst and a 90% attenuation for those of lower energy emitted by the preceding burst but detected in the same time gate. One thus obtains the following relation in the classical approximation that is sufficient at low energy:

$$f_b\,(\mathrm{Hz}) = 625 \times \frac{\sqrt{E_n(\mathrm{eV})}}{L(\mathrm{m})}\,. \qquad (15)$$

(2) *At higher energy*, above 10 or 100 keV, the $(1/v_n)$ filter method is not applicable because the $1/v_n$ cross-section component becomes smaller with increasing energy than the other components. But for certain experiments (e.g., those using proton-recoil detection), another method, called the threshold method, can be used. In this case, a threshold is set on the energy of the recoiling proton (or another associated particle) in such a way that the neutrons emitted by the preceding burst do not have enough energy to be detected. In setting the repetition rate to

$$f_b\,(\mathrm{Hz}) = (1.25 \times t_n)^{-1}, \qquad (16)$$

there is a factor of about 5 in the energies of the neutrons detected at the TOF t_n when they are emitted at two successive bursts. This is more than sufficient to ensure rejection of the unwanted neutrons.

In the calculations, we assume that the filter method can be used up to 100 keV, and the threshold method can be used at 1 MeV and above.

(7a) Calculate the neutron flux Φ_n at the distance L using the relation

$$\Phi_n = N_b \times f_b \times 10^{-4} \times (1/L^2) \qquad (17)$$

in which all the quantities are known. For simplicity, no attenuation of the neutron flux along the flight path has been taken into account.

If the flight-path length calculated in procedure (5a) is shorter than L_m ($L < L_m$), the following modified procedure must be followed:

(1b) Follow the procedure as in (1a).

(2b) Calculate a new value of σ_t, called σ_{Lm}, from σ_E (given by the resolution profile) and L_m.

(3b) Optimize the charged-particle burst time width using the quadratic combination of the standard deviations obtained in procedures (1b) and (2b).

(4b) Calculate the actual standard deviation σ_t by quadratic combination of the values obtained in procedures (1b) and (3b).

(5b) Determine the neutron output per burst for the width obtained in procedure (3b).

(6b) Calculate the repetition rate as in procedure (6a) using L_m instead of L whenever necessary.

(7b) Calculate the neutron flux as in procedure (7a).

The procedures just defined are applied below to calculate the performances of LANSCE, WNR, and ORELA.

D. Results of the calculations for LANSCE

The characteristics of the moderated neutron beam coming from the LANSCE moderator used for nuclear physics, with a field of view of 12 × 12 cm^2, is calculated using the Monte Carlo method.[4]

The standard deviation σ_{tm} can be approximated by $\sigma_{tm}(ns) = 2800 \times E_n^{-0.394}$ and the neutron output by $N_{lk} = 4 \times 10^{-3} \times E_n^{-1}$ neutrons/eV/sr/incident proton (where E_n is in eV in these two expressions).

An upgraded version of LANSCE is also considered in which a simple bare-water moderator is used. The time spread is reduced to $\sigma_{tm}(ns) = 1{,}000\sqrt{E_n(eV)}$, but the same neutron output is assumed.

The proton burst has the shape of an isosceles triangle having an FWHM of 125 ns. The repetition frequency is fixed to 20 Hz. The average proton current is 60 μA.

The results obtained with these calculations are illustrated in Table 3 for LANSCE and for the resolution profile RP1. Also the various shapes of the resolution function calculated at different energies are given and discussed in Appendix B.

TABLE 3

NEUTRON FLUX CALCULATIONS FOR LANSCE AND FOR RP1

E_n (eV)	N_{lk} (n/sr/eV/p)	σ_{tm} (ns)	σ_b (ns)	σ_t (ns)	L (m)
1.00E+00	4.00E-03	2.80E+03	51	2.80E+03	7.00
1.00E+01	4.00E-04	1.13E+03	51	1.13E+03	23.11
1.00E+02	4.00E-05	4.56E+02	51	4.59E+02	93.78
1.00E+03	4.00E-06	1.84E+02	51	1.91E+02	390.35
1.00E+04	4.00E-07	7.43E+01	51	9.01E+01	626.13
1.00E+05	4.00E-08	3.00E+01	51	5.92E+01	1299.84
1.00E+06	4.00E-09	1.21E+01	51	5.24E+01	3645.77

E_n (eV)	f_b (Hz)	Φ_n (n/cm^2/eV/s)	N_b (n/sr/eV/burst)	t_n (μs)
1.00E+00	20	3.06E+06	7.50E+10	5.04E+02
1.00E+01	20	2.81E+04	7.50E+09	5.26E+02
1.00E+02	20	1.71E+02	7.50E+08	6.75E+02
1.00E+03	20	9.84E-01	7.50E+07	8.89E+02
1.00E+04	20	3.83E-02	7.50E+06	4.51E+02
1.00E+05	20	8.88E-04	7.50E+05	2.96E+02
1.00E+06	20	1.13E-05	7.50E+04	2.63E+02

E. Results of the calculations for WNR

The target used at WNR at the present time is a cylinder of tungsten (ϕ = 3 cm and l = 7.5 cm) surrounded by a thin 1.2-mm-thick water jacket used for cooling, but it plays a negligible role for neutron moderation. This target is used for the production of fast neutrons with energies above a few tens of keV.

In the calculations discussed below, six other different types of targets were considered: three for fast neutrons (bare targets) and three for moderated neutrons. These two sets of targets are called WNRB for fast neutrons and WNRM for moderated neutrons (Fig. 8). The detailed characteristics of these targets are given in Appendix C.

None of these targets has actually been tried experimentally yet or even optimized in the calculations, but their study provides a good illustration of the potential of WNR over the whole energy range.

Calculations of the neutron output (σ_{tm} and N_{lk}), using the Monte Carlo method, are made for all of these targets for neutrons emitted at 90^0 relative to the proton beam.[4]

The fine time structure in each proton burst depends on the mode of operation (bunched or unbunched) for the microbursts (Fig. 3). Each microburst has a shape close to a Gaussian with an FWHM of about 0.25 ns (σ_b = 0.106 ns).

The number of protons in each microburst is 10^8 in the unbunched mode and 3×10^8 in the bunched mode (Sec. II.D.2).

The number of microbursts N_μ taken in each proton burst is determined to match the moderation time. When two or more microbursts are used, the proton burst is assumed to have a rectangular shape with a duration $\Delta t_b = (N_\mu - 1) \times 5$ ns (unbunched mode). This leads to a standard deviation $\sigma_b = \Delta t_b/(2\sqrt{3})$ that should be as close as possible to that of the neutron time spread in the target-moderator system. The unbunched mode of operation is preferred for $\Delta t_b \geq 20$ ns because it gives a higher neutron output than the bunched one for the same burst duration. But when the moderation time leads to $\Delta t_b < 20$ ns, then one single microburst in the bunched mode is preferable.

The repetition frequency of the experiment depends on the time structure of the proton beam (Fig. 3) and has to be considered with some care. The maximum repetition rate of the 625-μs macrobursts is 40 Hz. This maximum repetition rate of the experiment can also be used at low energy when only one burst of N_μ microbursts is extracted from each macroburst. But at high energy, the neutron frame overlap is less stringent and several bursts of N_μ microbursts can be accommodated in each macroburst. During the duration of the macroburst, the repetition rate of the bursts is given by f_b as defined in Sec. IV.C, but the number of pulses (semiperiodic) per second is neither f_b nor 40 Hz, but rather $40 \times 625 \times 10^{-6} \times f_b$. In short, the repetition rate of the experiment, called F_b for WNR, depends on the value of f_b. The following three cases need to be considered:

- $f_b(\text{Hz}) < 40$, (18)
  in this case, $F_b = f_b$;

- $40 < f_b(\text{Hz}) < (10^6/625)$,
  in this case, F_b = 40 Hz; and

- $(10^6/625) < f_b(\text{Hz})$,

in this case, $F_b = 40 \times 625 \times 10^{-6} \times f_b = 0.025 \times f_b$.

The calculations were carried out using these figures for all targets, for the resolution profiles RP1 and RP2, and for a circular field of view (FOV) of 10 cm in diameter (the maximum FOV available outside the target room).

The results obtained are illustrated in Tables 4 and 5 for the targets WNR3 and WNR4 (with a thickness of 5 cm), respectively (see Appendix C).

TABLE 4

NEUTRON FLUX CALCULATIONS FOR WNR3 AND FOR RP1

E_n (eV)	N_{lk} (n/sr/MeV/p)	σ_{tm} (ns)	N_μ	σ_t (ns)	L (m)
1.00E+04	4.01E-01	2.56E+01	18	3.54E+01	492.45
1.00E+05	5.50E-01	8.81E+00	7	1.24E+01	542.70
1.00E+06	2.83E-01	1.59E+00	1	1.59E+00	221.13
1.00E+07	9.13E-03	1.91E-01	1	2.18E-01	61.18
5.00E+07	7.91E-04	1.20E-01	1	1.60E-01	46.29
1.00E+08	2.60E-04	1.10E-01	1	1.53E-01	45.90
2.00E+08	4.53E-05	1.04E-01	1	1.48E-01	48.08
3.16E+08	5.98E-06	1.00E-01	1	1.46E-01	51.21

E_n (eV)	F_b (Hz)	Φ_n (n/cm^2/eV/s)	N_b (n/sr/eV/burst)	t_n (μs)
1.00E+04	40	1.19E-05	7.22E+02	3.54E+02
1.00E+05	40	5.23E-06	3.85E+02	1.24E+02
1.00E+06	1280	2.22E-04	8.49E+01	1.59E+01
1.00E+07	14280	1.04E-03	2.74E+00	1.40E+00
5.00E+07	40840	4.52E-04	2.37E-01	4.90E-01
1.00E+08	56120	2.08E-04	7.80E-02	3.56E-01
2.00E+08	70800	4.16E-05	1.36E-02	2.82E-01
3.16E+08	77880	5.33E-06	1.79E-03	2.57E-01

F. Results of the calculations for ORELA

The vast majority of the experiments carried out at ORELA make use of the tantalum-water target briefly described in Sec. II.E.3.

TABLE 5

NEUTRON FLUX CALCULATIONS FOR WNR4
AND FOR RP1

E_n (eV)	N_{lk} (n/sr/MeV/p)	σ_{tm} (ns)	N_μ	σ_t (ns)	L (m)
1.00E+00	3.94E+03	1.10E+03	1122	1.96E+03	8.00
1.00E+01	5.26E+02	2.88E+02	199	4.07E+02	16.63
1.00E+02	7.86E+01	1.00E+02	69	1.41E+02	57.66
1.00E+03	1.08E+01	3.44E+01	23	4.78E+01	195.27
1.00E+04	1.79E+00	1.21E+01	8	1.68E+01	232.81
1.00E+05	4.56E-01	4.21E+00	1	4.21E+00	184.38
1.00E+06	1.70E-01	1.19E+00	1	1.20E+00	166.65
1.00E+07	8.62E-03	2.07E-01	1	2.33E-01	65.13

E_n (eV)	F_b (Hz)	Φ_n (n/cm^2/eV/s)	N_b (n/sr/eV/burst)	t_n (μs)
1.00E+00	40	2.76E+04	4.42E+08	5.76E+02
1.00E+01	40	1.51E+02	1.05E+07	3.78E+02
1.00E+02	40	6.53E-01	5.42E+05	4.15E+02
1.00E+03	40	2.61E-03	2.48E+04	4.45E+02
1.00E+04	40	1.06E-04	1.43E+03	1.68E+02
1.00E+05	40	1.60E-05	1.37E+02	4.21E+01
1.00E+06	1680	3.08E-04	5.10E+01	1.20E+01
1.00E+07	13400	8.17E-04	2.59E+00	1.49E+00

Yet, for completeness, we also include in these calculations the possibility of using a thick beryllium target for fast neutrons because it may prove more efficient than the tantalum target for the production of high-energy neutrons above 2 MeV. In this section, we therefore consider these two targets.

1. Tantalum target

For moderated neutrons, up to a few hundreds of keV, the neutron spectrum obtained from measurements can be approximated by the following relation:

$$N_b \times f_b = 1.9 \times 10^{10} \times E_n^{-0.75} \quad \text{neutrons/sr/eV/s}, \qquad (19)$$

where E_n is in eV for the maximum power of 50 kW.[8]

At the ORELA electron energy, the neutron output is proportional to the beam power. Therefore, the number of neutrons

per burst, N_b, can be expressed in terms of the energy in the electron burst. One then obtains

$$N_b = 3.8 \times 10^5 \times E_n^{-0.75} \quad n/sr/eV/J. \qquad (20)$$

In this expression, the energy dependence $E_n^{-0.75}$ is probably overestimated. More recent experiments and calculations seem to be more in favor of a $E_n^{-0.81}$ dependence.[5] Though the difference looks small, it can have a noticeable effect over a wide energy range (as much as a factor of 2 over 100 keV).

The moderation time in this energy region has been calculated by the Monte Carlo method and verified experimentally in a few cases.[6] The FWHM of the time distribution, expressed in terms of a distance uncertainty ΔL, obeys the following relation:

$$\Delta L = 18.8 - 0.283 \times (\mathrm{Ln}\ E_n) + 0.116 \times (\mathrm{Ln}\ E_n)^2, \qquad (21)$$

where ΔL is expressed in millimeters and E_n is expressed in eV.

This expression for ΔL can be transformed into the standard deviation σ_m of the time distribution, assuming that the time distribution has the form x^2e^{-x} (with $x = t/\tau$, where τ is the mean collision time). One then obtains

$$\sigma_m = [784 - 11.8 \times (\mathrm{Ln}\ E_n) + 4.84 \times (\mathrm{Ln}\ E_n)^2] \times E_n^{-1/2}, \qquad (22)$$

where σ_m is expressed in nanoseconds and E_n is expressed in eV.

This relation in fact holds up to 10 keV only, but in the absence of better knowledge, we used it up to 100 keV (bearing in mind that there might be fairly large uncertainties beyond 10 keV).

In addition one has to take into account the transit times of the electrons, the photons, and the fast neutrons inside the target. In the absence of any information on these effects, we assumed that they were equivalent to a Gaussian having an FWHM of 1 ns (σ_s = 0.423 ns).

Therefore, for moderated neutrons, one has

$$\sigma_{tm} = (\sigma_m^2 + \sigma_s^2)^{1/2}. \qquad (23)$$

For fast neutrons, the neutron production has been calculated with the electron-photon cascade method for thick tantalum targets.[9] The calculations made with this method for a

semi-infinite slab having a 20-rad-length thickness (1-rad length in tantalum is equal to 0.3823 cm) are in agreement with measurements carried out with the tantalum target from 1 to 20 MeV (Fig. 9).[10] For completeness, the neutron spectrum above 20 MeV, where no experimental data exist, is derived from the calculations (Fig. 10).[9]

The neutron time distribution of fast neutrons above 1 MeV must take into account the transit times of the electrons, the photons, and the fast neutrons inside the target mentioned above but not the moderation time, which is neglected. Therefore, for fast neutrons, one assumes somewhat arbitrarily that $\sigma_{tm} = 0.423$ ns.

In all cases, whether it is for moderated or fast neutrons, the electron burst is supposed to have a rectangular shape with a time width Δt_b of 2 to 24 ns ($\sigma_b = \frac{\Delta t_b}{2\sqrt{3}}$).

2. Beryllium target

This target is considered for fast neutrons only. Although no experimental data on the neutron spectrum exist, calculations that use the electron-photon cascade method are available.[9] The results of these calculations can be seen in Fig. 10. Our calculations have used these results obtained with 1 rad-length thickness (1 rad-length thickness in beryllium is equal to 36.75 cm), though the target actually used is certainly shorter. On the other hand, the bremsstrahlung is made in a tantalum radiator where it is more efficient than in beryllium. Therefore, the tantalum radiator may compensate for the use of a short target.

The standard deviation of the time distribution is assumed to be the same as for the tantalum target.

The calculations for the tantalum and the beryllium targets were made for the resolution profiles RP1 and RP2. An illustration of the calculations is given in Table 6 for the tantalum target and for RP1.

G. Discussion of the results

1. General presentation of the results

To facilitate the discussion of the above calculations, the results are plotted in the form of the neutron flux Φ_n, the TOF distance L, and the repetition frequency f_b (or F_b) as a function of the neutron energy E_n for each resolution profile RP1 and RP2 (Figs. 11-24).

TABLE 6

NEUTRON FLUX CALCULATIONS FOR ORELA AND FOR RP1

E_n (eV)	N_{lk} (n/sr/eV/J)	σ_{tm} (ns)	Δt_b (ns)	σ_t (ns)	L (m)
1.00E+00	3.80E+05	7.84E+02	24	7.84E+02	8.90
1.00E+01	6.76E+04	2.47E+02	24	2.48E+02	10.11
1.00E+02	1.20E+04	8.32E+01	24	8.35E+01	34.12
1.00E+03	2.14E+03	2.95E+01	24	3.03E+01	123.90
1.00E+04	3.80E+02	1.09E+01	24	1.29E+01	179.05
1.00E+05	6.76E+01	4.10E+00	14	5.80E+00	254.75
1.00E+06	8.32E+01	4.23E-01	2	7.15E-01	99.47
2.00E+06	2.08E+01	4.23E-01	2	7.15E-01	140.78
4.00E+06	2.90E+00	4.23E-01	2	7.15E-01	199.41
1.00E+07	3.32E-01	4.23E-01	2	7.15E-01	200.38
2.00E+07	1.24E-02	4.23E-01	2	7.15E-01	201.98
4.00E+07	6.24E-03	4.23E-01	2	7.15E-01	205.21

E_n (eV)	f_b (Hz)	Φ_n (n/cm^2/eV/s)	J_b (J)	N_b (n/sr/eV/burst)	t_n (μs)
1.00E+00	70	1.68E+03	50	1.90E+07	6.41E+02
1.00E+01	195	6.45E+02	50	3.38E+06	2.30E+02
1.00E+02	183	9.45E+00	50	6.01E+05	2.46E+02
1.00E+03	160	1.11E-01	50	1.07E+05	2.82E+02
1.00E+04	349	2.07E-02	50	1.90E+04	1.29E+02
1.00E+05	1000	4.19E-03	40	2.72E+03	5.80E+01
1.00E+06	1000	2.52E-03	3	2.49E+02	7.17E+00
2.00E+06	1000	3.14E-04	3	6.23E+01	7.18E+00
4.00E+06	1000	2.19E-05	3	8.69E+00	7.20E+00
1.00E+07	1000	2.48E-06	3	9.95E-01	4.60E+00
2.00E+07	1000	9.11E-08	3	3.72E-02	3.30E+00
4.00E+07	1000	4.44E-08	3	1.87E-02	2.41E+00

These plots are made in two series, one (called A) for the facilities as they now exist (LANSCE; WNR, equipped with the bare target WNR0; and ORELA, used with a tantalum target) and another one (called B) for the same facilities with a moderate upgrade.

Other more important upgrades are considered in Chapter V.

These plots are made (1) for the maximum FOVs for experiments (not for the maximum FOVs corresponding to the full

size of the target-moderator systems) and (2) for flight paths at right angles relative to the direction of the charged-particle beam.

The effect of reducing the FOV is discussed in Sec. IV.G.4. and the consequences of using different inclinations of the neutron beams relative to that of the charged-particle beam are examined in Sec. IV.G.5.

2. Comparison of the A-plots

(a) *A-plots of the neutron flux.* The A-plots of the neutron flux, $\Phi_n(E_n)$, versus neutron energy for the resolution profiles RP1 and RP2 (Figs. 11 and 14, respectively) have the same general pattern. At low energy, LANSCE is superior, then ORELA takes over in the middle of the energy range, and, finally, WNR (equipped with the WNR0 target) takes over at the high-energy end. The exact boundaries between these different zones depend on the conditions of the comparison.

These results can easily be explained by the fast neutron production and the time structure discussed in Chapter II.

At low energy, LANSCE is superior to ORELA, by a factor larger than 10^3 at 1 eV because of its higher neutron production and its low duty cycle. At this low energy, LANSCE is not penalized by its relatively broad proton burst and its low repetition frequency, whereas ORELA cannot take advantage of its narrow bursts and its high repetition rate. The advantage of LANSCE over ORELA would be even greater for some experiments if the shape, not the standard deviation, were taken into account (see Appendix B).

The advantage of LANSCE over ORELA decreases with increasing neutron energy until ORELA overtakes LANSCE at intermediate energies. ORELA can then use its narrow bursts and its high repetition rate, whereas LANSCE is penalized by its broad burst and is obliged to compensate for that by using very long and unrealistic flight paths that result in very small solid angles. WNR, equipped with target WNR0, cannot be used below 10 keV because of the almost complete absence of neutron moderation. Above this energy, and up to MeV energies, WNR is much penalized by its low repetition frequency and its high rejection of microbursts. For example, at 100 keV, WNR takes only one out of the 3.125×10^4 microbursts in each macropulse, and the repetition frequency is still only 40 Hz as compared with a repetition frequency of 1,000 Hz for ORELA.

At high energy, LANSCE has a lower flux than ORELA above 100 keV and cannot be used at such energies because of unrealistic flight-path lengths (see Sec. IV.G.2.b.). WNR has the

advantage over ORELA because its neutron spectrum is harder and the time resolution of its microbursts is very good. Also the less stringent neutron overlap above 1 MeV makes the use of high repetition rates possible. Yet, even in the high-energy region, WNR is far from using its full potential because it does not use most of its microbursts.

(b) *A-plots of the time-of-flight distance.* The A-plots of the TOF distance, L, versus neutron energy for the resolution profiles RP1 and RP2 (Figs. 12 and 15, respectively) illustrate the limitations imposed by the short available distances, especially at LANSCE. The maximum distance presently available is 55 m at LANSCE and 90 m at WNR (this last one is not at a right angle relative to the proton beam). This limits the measurements at LANSCE to about 40 eV for RP1 (resonance analysis) and 5 keV for RP2. Such limitations do not exist, at least not to such an extent, at ORELA. Therefore, resonance spectroscopy can be carried out in much better conditions at ORELA, but LANSCE is a much better facility for the study of compound-nucleus decay properties in low-energy resonances. The limitations imposed by the short available flight paths are less stringent for WNR, though the inclinations of the flight paths introduce other deteriorations of the resolution function discussed in Sec. IV.G.5.

(c) *A-plots of the repetition frequency.* The A-plots of the repetition frequency, f_b (or F_b for WNR), versus neutron energy for the resolution profiles RP1 and RP2 (Figs. 13 and 16, respectively), illustrate the modes of operation of these three facilities. The repetition frequency for LANSCE is always equal to 20 Hz. It is low enough to avoid any neutron overlap, even at low energy, and consequently leads to no loss of neutron flux over the whole energy range where it can be used. The maximum repetition frequency for ORELA, f_b = 1,000 Hz, cannot be used at low energy, at least not until 100 keV for RP1 and 1 keV for RP2. This explains partially why ORELA is penalized at low energy compared with LANSCE. WNR is even more penalized by neutron overlap. Below 1 MeV and for RP1, WNR can use only the macroburst repetition frequency of 40 Hz. Still for RP1, it is only at 1 MeV and above that WNR can increase its repetition frequency to higher and higher values with increasing neutron energy, culminating to f_b = 85,480 Hz at 316 MeV. The same situation is met for RP2, though not as severely as for RP1. For RP2, the repetition frequency is already 80 Hz at 10 keV and reaches the value f_b= 498,000 Hz at 316 MeV. This behavior of the repetition

frequency for WNR explains partially why WNR gradually overtakes ORELA with increasing energy.

The numerical values for the A-plots are given in Tables 7 and 8 for RP1 and RP2, respectively.

3. Comparison of the B-plots

The B-plots illustrate the improvements in the characteristics of the facilities brought about by the moderate upgrades described below.

For LANSCE, the upgrade would include a slightly different moderator, provided it is compatible with the needs of other users. For WNR, the upgrade would include different targets with and without moderators. Because many different targets have been studied, the plots of $\Phi_n(E_n)$ are restricted to the envelopes of the results for targets WNRM and WNRB. Therefore, the plot $\phi_n(E_n)$ for WNRB is the envelope of the results for targets WNR1, WNR2, and WNR3, and, in the same manner, the plot $\Phi_n(E_n)$ for WNRM is the envelope of the results for targets WNR4, WNR5, and WNR6. The distances L for WNRB and WNRM are chosen and plotted accordingly. For ORELA, the upgrade includes the possibility of using a beryllium target at high energy, above 2 MeV.

(a) *B-plots of the neutron flux.* The general pattern of the neutron flux, $\Phi_n(E_n)$, versus neutron energy for the resolution profiles RP1 and RP2 (Figs. 17 and 20, respectively) is very similar to that of the A-plots.

At low energy, LANSCE still has a greater advantage over ORELA because of the reduction of the LANSCE moderation time. But this advantage is cancelled at energies where this moderation time becomes shorter than the duration of the proton burst (above about 1 keV). WNR, equipped with WNRM targets, can be used at low energy but with a lower flux than both LANSCE and ORELA (at least above a few eV for RP1 and a few tens of eV for RP2, for this latter facility).

At higher energies, the upgrade of the facilities does not drastically change the conclusions already drawn from the A-plots.

Comparing the performances of the various targets studied for WNR can be of interest. To this aim, plots have been made for the resolution profile RP1 of the maximum and of the minimum neutron fluxes $\Phi_n(E_n)$ as a function of neutron energy

TABLE 7

NEUTRON FLUX, FLIGHT PATH LENGTH, AND REPETITION RATE CALCULATIONS FOR ORELA, LANSCE, AND WNR (CASE A) AND FOR RP1

E_n (eV)	Φ_n (n/cm^2/eV/s)	L (m)	f_b (Hz)	Φ_n (n/cm^2/eV/s)	L (m)	f_b (Hz)
	ORELA	ORELA	ORELA	LANSCE	LANSCE	LANSCE
1.00E+00	1.68E+03	8.90	70	3.06E+06	7.00	20
1.00E+01	6.45E+02	10.11	195	2.81E+04	23.11	20
1.00E+02	9.45E+00	34.12	183	1.71E+02	93.78	20
1.00E+03	1.11E-01	123.90	160	9.84E-01	390.35	20
1.00E+04	2.07E-02	179.05	349	3.83E-02	626.13	20
1.00E+05	4.19E-03	254.75	1000	8.88E-04	1299.84	20
1.00E+06	2.52E-03	99.47	1000	1.13E-05	3645.77	20
2.00E+06	3.14E-04	140.78	1000			
4.00E+06	2.19E-05	199.41	1000			
1.00E+07	2.48E-06	200.38	1000			
2.00E+07	9.11E-08	201.98	1000			
4.00E+07	4.44E-08	205.21	1000			

E_n (eV)	Φ_n (n/cm^2/eV/s)	L (m)	F_b (Hz)
	WNR	WNR	WNR
1.00E+04	1.67E-05	237.84	40
1.00E+05	8.67E-06	176.85	40
1.00E+06	8.53E-04	114.95	2440
2.00E+06			
4.00E+06			
1.00E+07	1.48E-03	50.08	17440
2.00E+07			
4.00E+07			
5.00E+07	5.69E-04	40.39	46800
1.00E+08	2.46E-04	41.21	62520
2.00E+08	4.24E-05	43.59	78120
3.16E+08	5.60E-06	46.67	85480

TABLE 8

NEUTRON FLUX, FLIGHT PATH LENGTH, AND REPETITION RATE CALCULATIONS FOR ORELA, LANSCE, AND WNR (CASE A) AND FOR RP2

E_n (eV)	Φ_n (n/cm^2/eV/s)	L (m)	f_b (Hz)	Φ_n (n/cm^2/eV/s)	L (m)	f_b (Hz)
	ORELA	ORELA	ORELA	LANSCE	LANSCE	LANSCE
1.00E+00	1.68E+03	8.90	70	3.06E+06	7.00	20
1.00E+01	9.47E+02	8.90	222	3.06E+05	7.00	20
1.00E+02	5.32E+02	8.90	702	1.71E+04	9.38	20
1.00E+03	6.96E+01	12.39	1000	9.84E+01	39.03	20
1.00E+04	5.92E+00	17.90	1000	3.83E+00	62.61	20
1.00E+05	4.19E-01	25.47	1000	8.88E-02	129.98	20
1.00E+06	2.52E-01	9.95	1000	1.13E-03	364.58	20
2.00E+06	3.14E-02	14.08	1000			
4.00E+06	2.19E-03	19.94	1000			
1.00E+07	2.48E-04	20.04	1000			
2.00E+07	9.11E-06	20.20	1000			
4.00E+07	4.44E-06	20.52	1000			

E_n (eV)	Φ_n (n/cm^2/eV/s)	L (m)	F_b (Hz)
	WNR	WNR	WNR
1.00E+04	3.33E-03	23.78	80
1.00E+05	2.60E-02	11.18	480
1.00E+06	2.51E+00	8.00	34720
2.00E+06			
4.00E+06			
1.00E+07	3.62E-01	8.00	108960
2.00E+07			
4.00E+07			
5.00E+07	7.32E-02	8.00	236200
1.00E+08	3.37E-02	8.00	321960
2.00E+08	6.86E-03	8.00	425520
3.16E+08	1.11E-03	8.00	498560

separately for all WNRM and WNRB targets that were studied (Figs. 17 and 18, respectively).

The performances are very similar below 1 keV for targets equipped with moderators, but differences up to a factor of about 10 show up above this energy (Fig. 17).

A rather opposite situation is observed for bare targets. Differences of up to a factor of about 6 are noticed below 10 MeV, but the performances of the targets are very similar above this energy. It can be remarked that the target WNR0 now used at WNR gives results very close, if not identical, to the maximum values (Fig. 18). Therefore, this target can be improved only with great difficulty.

(b) *B-plots of the time-of-flight distance.* The B-plots of the TOF distance, $L(E_n)$, versus neutron energy for the resolution profiles RP1 and RP2 (Figs. 18 and 21, respectively) illustrate at low energy the shorter flight paths that can be used for LANSCE and WNR. Below a few keV all three facilities need about the same flight-path lengths. Above this energy, LANSCE is again obliged to use longer flight paths because of its too broad proton pulse.

(c) *B-plots of the repetition frequency.* The B-plots of the repetition frequency, f_b (or F_b for WNR), versus neutron energy for the resolution profiles RP1 and RP2 (Figs. 19 and 22, respectively) have the same general behavior as those of the A-plots, and the same comments as those of Sec. IV.7.b can be made.

The numerical values used in the B-plots are given in Tables 9 and 10 for RP1 and RP2, respectively.

4. Field of view

The effect of the FOV was not studied in detail for all possible configurations. Qualitatively, any reduction in the FOV will not only decrease the neutron leakage but may also shorten the time spread. The latter may compensate for the former for TOF experiments, but the exact gain (or loss) has to be studied case by case.

As an illustration, the variation in neutron leakage with the radius of the FOV, presumed to be circular, is given in Fig. 25 for 10-keV neutrons emitted by target WNR4 (with a thickness of 5 cm). The neutron leakage with a 10-cm-diam FOV (maximum available at WNR) is about 45% that leakage in the absence of collimation.

The effect of the FOV on the neutron flux at the sample position was also calculated as a function of neutron energy using the same target WNR4 as above for resolution profile RP1 and for two

TABLE 9

NEUTRON FLUX, FLIGHT PATH LENGTH, AND REPETITION RATE CALCULATIONS FOR ORELA, LANSCE, AND WNR (CASE B) AND FOR RP1

E_n (eV)	Φ_n (n/cm^2/eV/s)	L (m)	f_b (Hz)	Φ_n (n/cm^2/eV/s)	L (m)	f_b (Hz)
	ORELA	ORELA	ORELA	LANSCE	LANSCE	LANSCE
1.00E+00	1.68E+03	8.90	70	3.06E+06	7.00	20
1.00E+01	6.45E+02	10.11	195	3.06E+05	7.00	20
1.00E+02	9.45E+00	34.12	183	2.85E+03	22.93	20
1.00E+03	1.11E-01	123.90	160	9.98E+00	122.59	20
1.00E+04	2.07E-02	179.05	349	1.15E-01	360.99	20
1.00E+05	4.19E-03	254.75	1000	1.19E-03	1122.50	20
1.00E+06	2.52E-03	99.47	1000	1.19E-05	3547.82	20
2.00E+06	1.07E-04	140.78	1000			
4.00E+06	2.19E-05	199.41	1000			
1.00E+07	6.79E-06	200.38	1000			
2.00E+07	1.22E-06	201.98	1000			
4.00E+07	2.36E-07	205.21	1000			
5.00E+07						
1.00E+08	5.39E-09	214.99	1000			

E_n (eV)	Φ_n (n/cm^2/eV/s)	L (m)	f_b (Hz)	Φ_n (n/cm^2/eV/s)	L (m)	f_b (Hz)
	WNRB	WNRB	WNRB	WNRM	WNRM	WNRM
1.00E+00				5.81E+04	8.00	40
1.00E+01				2.48E+02	16.89	40
1.00E+02				9.42E-01	53.67	40
1.00E+03				3.67E-03	176.54	40
1.00E+04	1.19E-05	492.45	40	7.78E-04	296.23	40
1.00E+05	1.03E-05	172.68	40	1.60E-05	184.88	40
1.00E+06	1.16E-03	111.92	2520	7.35E-04	268.59	1040
2.00E+06				8.17E-04	65.13	13400
4.00E+06						
1.00E+07	1.46E-03	53.99	16160			
2.00E+07						
4.00E+07						
5.00E+07	4.94E-04	44.79	42200			
1.00E+08	2.08E-04	45.90	56120			
2.00E+08	4.16E-05	48.08	70800			
3.16E+08	5.33E-06	51.21	77880			

TABLE 10

NEUTRON FLUX, FLIGHT PATH LENGTH, AND REPETITION RATE CALCULATIONS FOR ORELA, LANSCE, AND WNR (CASE B) AND FOR RP2

E_n (eV)	Φ_n (n/cm^2/eV/s)	L (m)	f_b (Hz)	Φ_n (n/cm^2/eV/s)	L (m)	f_b (Hz)
	ORELA	ORELA	ORELA	LANSCE	LANSCE	LANSCE
1.00E+00	1.68E+03	8.90	70	3.06E+06	7.00	20
1.00E+01	9.47E+02	8.90	222	3.06E+05	7.00	20
1.00E+02	5.32E+02	8.90	702	3.06E+04	7.00	20
1.00E+03	6.96E+01	12.39	1000	9.98E+02	12.26	20
1.00E+04	5.92E+00	17.90	1000	1.15E+01	36.10	20
1.00E+05	4.19E-01	25.47	1000	1.19E-01	112.25	20
1.00E+06	2.52E-01	9.95	1000	1.19E-03	354.78	20
2.00E+06	1.07E-02	14.08	1000			
4.00E+06	2.19E-03	19.94	1000			
1.00E+07	6.79E-04	20.04	1000			
2.00E+07	1.22E-04	20.20	1000			
4.00E+07	2.36E-05	20.52	1000			
5.00E+07						
1.00E+08	5.39E-07	21.50	1000			

E_n (eV)	Φ_n (n/cm^2/eV/s)	L (m)	f_b (Hz)	Φ_n (n/cm^2/eV/s)	L (m)	f_b (Hz)
	WNRB	WNRB	WNRB	WNRM	WNRM	WNRM
1.00E+00				6.46E+05	8.00	40
1.00E+01				7.32E+03	8.00	40
1.00E+02				7.88E+01	8.00	40
1.00E+03				3.67E-01	17.65	40
1.00E+04	2.14E-03	26.81	80	1.56E-01	29.62	80
1.00E+05	3.10E-02	10.92	480	1.12E-02	18.49	280
1.00E+06	4.61E+00	8.00	34720	7.32E-01	26.86	10360
2.00E+06				4.40E-01	8.00	108960
4.00E+06						
1.00E+07	4.66E-01	8.00	108960			
2.00E+07						
4.00E+07						
5.00E+07	8.76E-02	8.00	236200			
1.00E+08	3.95E-02	8.00	321960			
2.00E+08	9.04E-03	8.00	425520			
3.16E+08	1.42E-03	8.00	498560			

FOVs: 30×30 cm^2 and Φ = 10 cm. The results of the calculations made, using the same methods as before, are plotted in Fig. 26 in the form of the ratio of the neutron leakages, the neutron time spreads, and the neutron fluxes for both FOVs. It can be seen that using the Φ = 10 cm FOV instead of the 30 × 30 cm^2 one has the following consequences: (1) the neutron leakage is reduced by a factor that decreases with neutron energy from about 3.4 at 1 eV to about 1.5 at 1 MeV, (2) the standard deviation of the time distribution is practically not altered except above 100 keV, where it is slightly reduced, and (3) the neutron flux is consequently reduced in about the same manner as the neutron leakage.

The effect of the FOV can also be studied in the same manner for fast neutrons. As an illustration, the calculations were made with the bare target WNR3 and the results are plotted in Fig. 27. The neutron leakage is reduced by a factor that is almost 2 at low energy and decreases with increasing energy. The standard deviation of the time distribution is also reduced (much more than in the case of moderated neutrons) by as much as 2.2 at 10 MeV. As a consequence, the behavior of the neutron flux for fast neutrons is more complicated than that for moderated neutrons. Although the flux for fast neutrons is decreased below 400 keV, it increases above that energy by a factor as high as 5.7 at 10 MeV.

Therefore, although reducing the FOV apparently decreases the neutron flux for moderated neutrons and for fast neutrons below 1 MeV, it can be an advantage for fast neutrons above that energy.

It may be of interest to note from the inspection of Figs. 26 and 27 that similar conclusions could have been drawn by using the figure of merit

$$\mathrm{FOM} = \frac{N_b}{\sigma_t^2}, \tag{24}$$

where N_b is the neutron leakage and σ_t the usual standard deviation of the neutron time distribution, as previously defined by one of the authors.[11]

5. Inclination of the flight path

Changing the inclination of the flight path relative to the direction of the proton beam has two consequences: (1) modification of the neutron spectrum and (2) deterioration of the resolution function compared with what it is at right angles.

The neutrons emitted from the bombardment of a tungsten target by 800-MeV protons come from two types of interactions: (1) direct processes and (2) evaporation and fission. The former

component has a hard spectrum that extends to almost 800 MeV and is peaked forward, whereas the latter has a softer spectrum and is isotropic. Moving the flight path from a right angle to a forward angle will therefore harden the spectrum, as illustrated in Fig. 28 for the bare target WNR0 used at the present time. This procedure is in fact the only possibility for making measurements above 400 MeV. For moderated neutrons, the change is not very important.

When the flight path is inclined relative to the normal to the exit face of the target-moderator system, neutrons originating from different points of this system travel different distances before reaching the detector. This is the so-called distance uncertainty, called ΔL. The energy uncertainty ΔE that results from it is

$$\Delta E = 2 \times \Delta L \times \frac{E}{L}. \qquad (25)$$

It is often more convenient to convert this distance uncertainty ΔL into a time uncertainty Δt to compare it with the real time uncertainties discussed previously. One then obtains

$$\Delta t\,(\mu s) = \Delta L \times t_n = \Delta L(cm) \times 0.723/\sqrt{E_n(eV)}. \qquad (26)$$

This expression has the same energy dependence as that for a moderation time. It can be applied when there is no space-time correlation in the neutron leakage as is roughly the case for moderated neutrons we shall consider first.

For a circular FOV of diameter Φ, the distance uncertainty can be easily calculated, assuming that a uniform neutron leakage occurs over the whole moderator surface corresponding to the FOV. For a flight path inclined to an angle Θ relative to the normal to the moderator, the standard deviation σ_t of the time spread associated with this distance uncertainty is

$$\sigma_t\,(\mu s) = 0.723/\sqrt{E_n(eV)} \times \frac{\Phi(cm)}{4} \times \cos\Theta. \qquad (27)$$

For a flight path inclined to $\Theta = 45^0$, and for an FOV of $\Phi = 10$ cm (the maximum available at WNR), this standard deviation amounts to

$$\sigma_t\,(\mu s) = 1.278/\sqrt{E_n(eV)}. \qquad (28)$$

This standard deviation is about 50% more important than a typical moderation time. It can be reduced using a smaller FOV by an amount equal to the square of the reduction of the distance uncertainty. Neutron intensity is, of course, reduced by this approach. This solution may be an interesting method to achieve a given energy resolution with a shorter flight path.

The situation is more subtle for fast neutrons because there is actually a space-time correlation in the neutron emission as an effect of the finite time it takes the incoming protons to cross the target. This effect is not seen at right angles relative to the incoming proton beam but shows up at different angles. It turns out that this effect is beneficial at forward angles because there is a kind of compensation between the proton and the neutron travel times. The neutrons produced near the front end of the target appear earlier but with a travel time longer than those produced later near the other end of the target; this may compensate for the difference in the neutron production times (at least partially). The travel-time compensation is total if the knocked-on neutrons are emitted in the same direction and with the same energy as the incident protons.

V. POSSIBLE UPGRADES

A. Introduction

This chapter presents a summary of possible upgrades of ORELA, LANSCE, and WNR, previously discussed in this paper. It discusses also more important upgrades for LANSCE and for WNR (namely the use of a proton storage ring), as well as the installation of a lead slowing-down spectrometer at the LANSCE-WNR facility.

B. ORELA

The ORELA facility is difficult to upgrade, because it was from the outset very well designed for neutron TOF experiments. No important upgrade can be envisaged without major changes in the facility. For example, the increase in power of the electron beam would require major changes in the accelerator itself. A gain of 2 in the electron beam power would imply doubling the linac (accelerator guide and klystrons). A possible improvement could be envisaged at the injection level, for example, with a photo-injector using a laser beam. Very intense and short electron bursts might be accelerated in this manner. But no information is available on this possibility, which seems very futuristic at the present time, as well as on other possible upgrades of which we are not aware.

C. LANSCE

Several improvements can be made to improve the LANSCE performance for epithermal neutrons used with the TOF method. At the source level, it may be possible to reduce the proton burst width at the exit of the PSR, not by modifying the PSR, but by changing the proton load inside the ring. A study has been requested to measure the reduction in the proton current I_p that would occur when the proton pulse width Δt_b is decreased, while the repetition rate is kept the same. If the decrease in I_b is not too important, it may be advantageous to run the PSR at a lower current to acquire a gain in time resolution and then make measurements at shorter distances for a given energy resolution. It is possible also that the repetition rate may be increased while decreasing the proton current and the pulse width, but this possibility is not considered here.

As an illustration, we can assume somewhat arbitrarily that there is a linear relationship between I_p and Δt_b (FWHM), with a cut-off at 12.5 ns (10% the present value), below which the peak current drops to zero. This means that the current I_p has the following form:

$$I_{p\ (\mu A)} = 60 \times \frac{\Delta t_b(ns)}{125}, \quad \text{for } 12.5 < \Delta t_b < 125; \text{ and} \qquad (29)$$

$$I_{p\ (\mu A)} = 0, \quad \text{for } \Delta t_b < 12.5, \text{ and } \Delta t_b > 125.$$

The improvement that would result from the reduction of the pulse width is given in Figs. 29-34, using the numerical values given in Tables 11 and 12 for RP1 and RP2, respectively.

Also at the source level, a target-moderator system with a shorter time spread would make an interesting design, especially one with a shorter tail. In addition, the repetition rate could be increased above the present value of 20 Hz, which is small compared with 120 Hz--the LAMPF repetition rate.

Another improvement above a neutron energy of about 100 eV would be to increase the length of the flight paths. LANSCE has a very large intensity, but unfortunately a burst width that is too large. Even if it is improved as suggested above, the LANSCE burst width cannot compete with those of fast-pulsed machines such as ORELA. But LANSCE can overcome this disadvantage by using longer flight paths because its higher neutron intensity can compensate for smaller solid angles. It is unfortunate that the LANSCE flight paths are shorter than those of ORELA, whereas its burst width is longer. Therefore, longer flight paths would significantly improve LANSCE's potential use.

TABLE 11

NEUTRON FLUX, FLIGHT PATH LENGTH, AND REPETITION RATE CALCULATIONS FOR ORELA, LANSCE, AND WNR (CASE C) AND FOR RP1

E_n (eV)	Φ_n (n/cm^2/eV/s)	L (m)	f_b (Hz)	Φ_n (n/cm^2/eV/s)	L (m)	f_b (Hz)
	ORELA	ORELA	ORELA	LANSCE	LANSCE	LANSCE
1.00E+00	1.68E+03	8.90	70	3.06E+06	7.00	20
1.00E+01	6.45E+02	10.11	195	3.06E+05	7.00	20
1.00E+02	9.45E+00	34.12	183	2.85E+03	22.93	20
1.00E+03	1.11E-01	123.90	160	1.11E+01	91.36	20
1.00E+04	2.07E-02	179.05	349	3.05E-01	98.23	20
1.00E+05	4.19E-03	254.75	1000	8.63E-03	131.82	20
1.00E+06	2.52E-03	99.47	1000	1.15E-04	361.47	20
2.00E+06	1.07E-04	140.78	1000			
4.00E+06	2.19E-05	199.41	1000			
1.00E+07	6.79E-06	200.38	1000			
2.00E+07	1.22E-06	201.98	1000			
4.00E+07	2.36E-07	205.21	1000			
5.00E+07						
1.00E+08	5.39E-09	214.99	1000			

E_n (eV)	Φ_n (n/cm^2/eV/s)	L (m)	f_b (Hz)	Φ_n (n/cm^2/eV/s)	L (m)	f_b (Hz)
	WNRB (Ring)	WNRB (Ring)	WNRB (Ring)	WNRM (Ring)	WNRM (Ring)	WNRM (Ring)
1.00E+00				4.85E+06	8.00	78
1.00E+01				7.09E+05	10.09	196
1.00E+02				6.21E+03	38.16	164
1.00E+03				7.02E+01	125.85	157
1.00E+04	6.10E-01	198.37	240	4.48E+01	218.14	240
1.00E+05	1.07E+00	173.08	240	1.66E+00	185.26	240
1.00E+06	1.73E+00	117.95	240	2.89E+00	271.16	240
2.00E+06				1.09E-01	99.33	240
4.00E+06						
1.00E+07	1.29E-01	92.41	240			
2.00E+07						
4.00E+07						
5.00E+07	1.22E-02	89.44	240			
1.00E+08	3.79E-03	92.97	240			
2.00E+08	5.76E-04	99.13	240			
3.16E+08	6.60E-05	107.38	240			

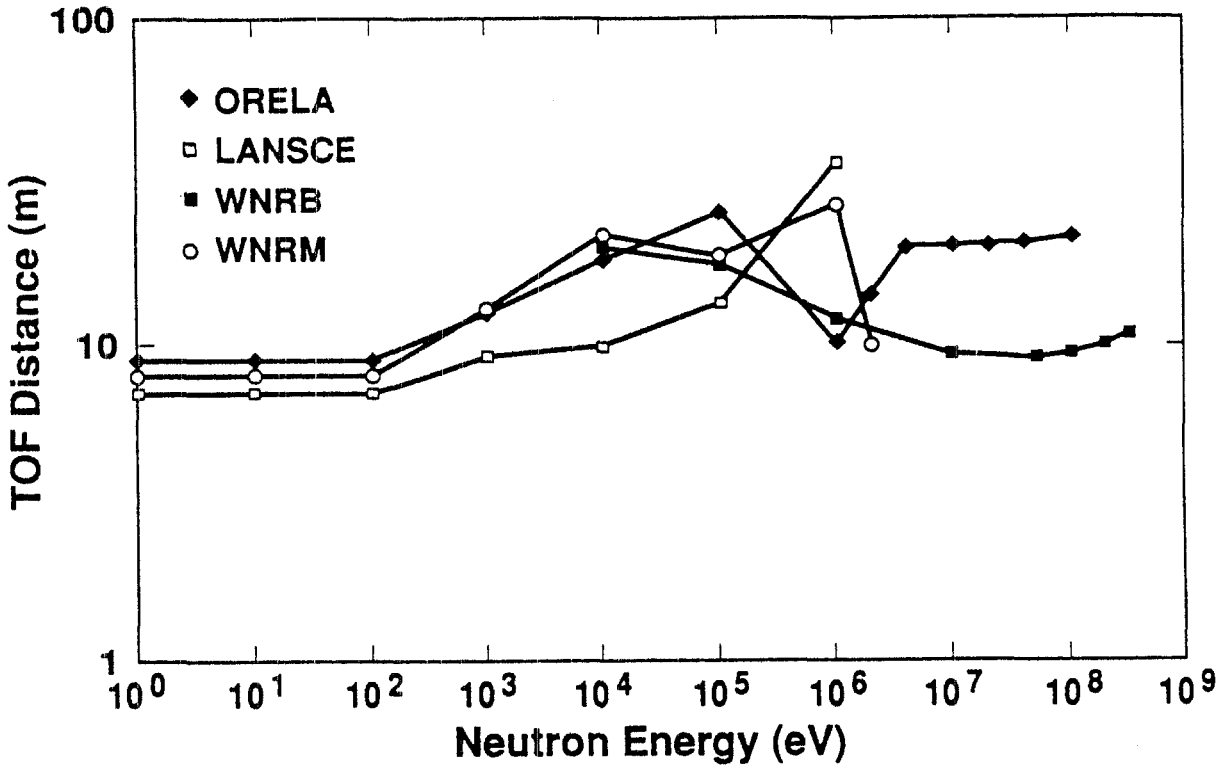

Fig. 33. TOF distance as a function of neutron energy for the resolution profile RP2 (Fig. 7) and for the three facilities: ORELA, LANSCE, and WNR, upgraded as described in the text (C-plot).

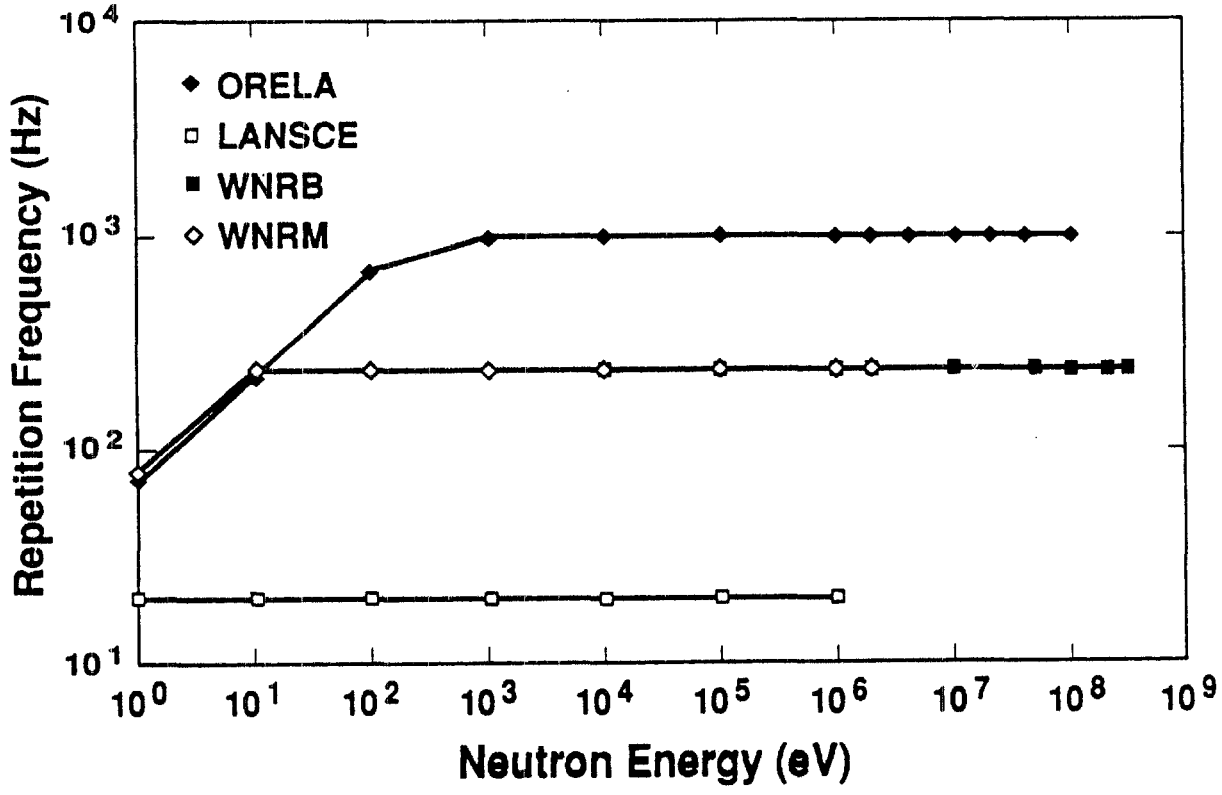

Fig. 34. Repetition frequency as a function of neutron energy for the resolution profile RP2 (Fig. 7) and for the three facilities: ORELA, LANSCE, and WNR, upgraded as described in the text (C-plot).

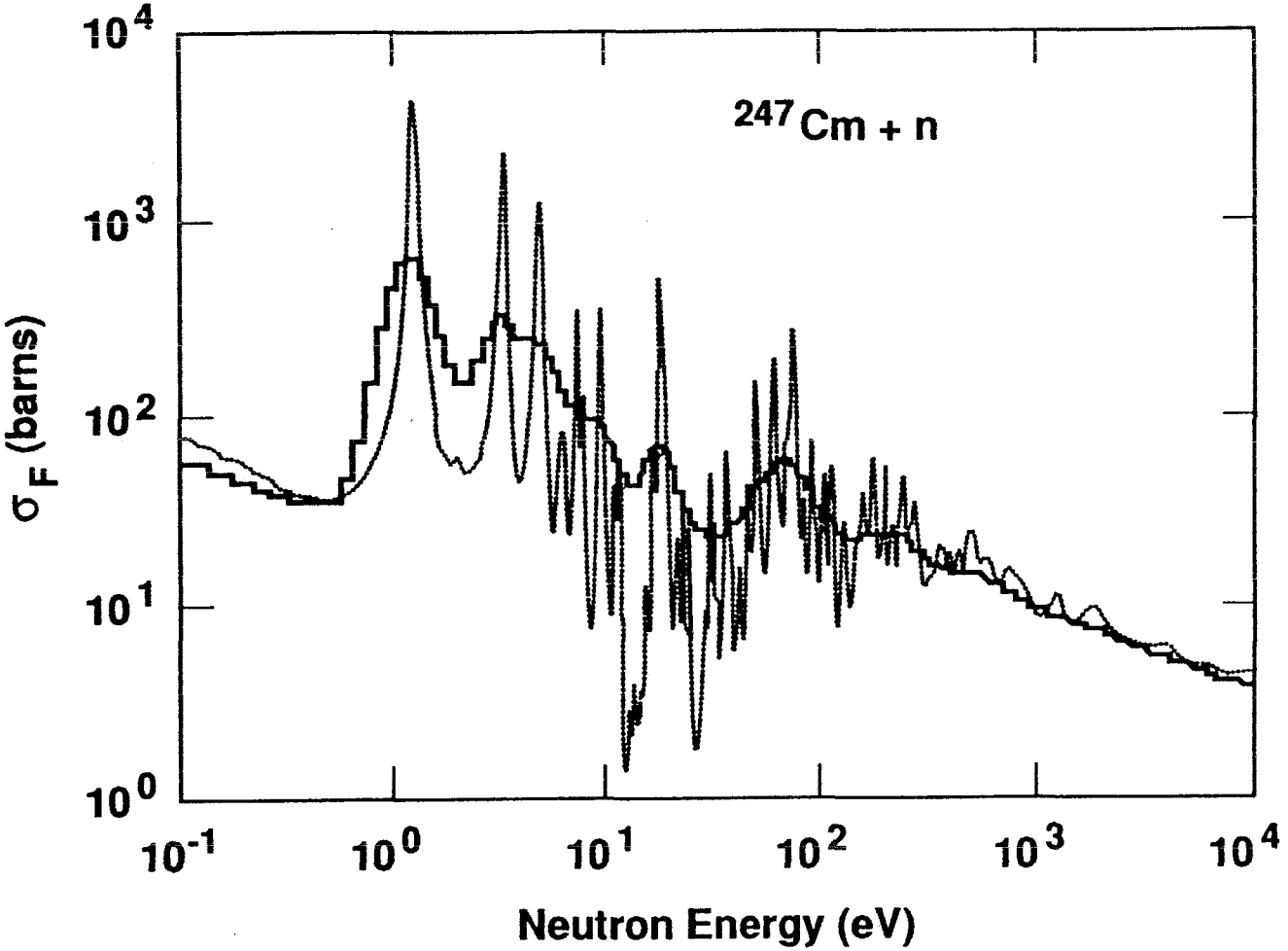

Fig. 35. Neutron-induced fission cross section of ^{247}Cm between 0.1 eV and 10 keV, as measured with the same fission chamber with the RINS at RPI (solid line) and in a conventional geometry at LANSCE (dotted line).[15]

TABLE 12

NEUTRON FLUX, FLIGHT PATH LENGTH, AND REPETITION RATE CALCULATIONS FOR ORELA, LANSCE, AND WNR (CASE C) AND FOR RP2

E_n (eV)	Φ_n (n/cm^2/eV/s)	L (m)	f_b (Hz)	Φ_n (n/cm^2/eV/s)	L (m)	f_b (Hz)
	ORELA	ORELA	ORELA	LANSCE	LANSCE	LANSCE
1.00E+00	1.68E+03	8.90	70	3.06E+06	7.00	20
1.00E+01	9.47E+02	8.90	222	3.06E+05	7.00	20
1.00E+02	5.32E+02	8.90	702	3.06E+04	7.00	20
1.00E+03	6.96E+01	12.39	1000	1.11E+03	9.14	20
1.00E+04	5.92E+00	17.90	1000	3.05E+01	9.82	20
1.00E+05	4.19E-01	25.47	1000	8.63E-01	13.18	20
1.00E+06	2.52E-01	9.95	1000	1.15E-02	36.15	20
2.00E+06	1.07E-02	14.08	1000			
4.00E+06	2.19E-03	19.94	1000			
1.00E+07	6.79E-04	20.04	1000			
2.00E+07	1.22E-04	20.20	1000			
4.00E+07	2.36E-05	20.52	1000			
5.00E+07						
1.00E+08	5.39E-07	21.50	1000			

E_n (eV)	Φ_n (n/cm^2/eV/s)	L (m)	f_b (Hz)	Φ_n (n/cm^2/eV/s)	L (m)	f_b (Hz)
	WNRB (Ring)	WNRB (Ring)	WNRB (Ring)	WNRM (Ring)	WNRM (Ring)	WNRM (Ring)
1.00E+00				4.85E+06	8.00	78
1.00E+01				1.71E+06	8.00	240
1.00E+02				2.09E+05	8.00	240
1.00E+03				1.07E+04	12.58	240
1.00E+04	6.10E+01	19.84	240	4.48E+03	21.81	240
1.00E+05	1.07E+02	17.31	240	1.66E+02	18.53	240
1.00E+06	1.73E+02	11.79	240	2.89E+02	27.12	240
2.00E+06				1.09E+01	9.93	240
4.00E+06						
1.00E+07	1.29E+01	9.24	240			
2.00E+07						
4.00E+07						
5.00E+07	1.22E+00	8.94	240			
1.00E+08	3.79E-01	9.30	240			
2.00E+08	5.76E-02	9.91	240			
3.16E+08	6.60E-03	10.74	240			

D. WNR

There is a region in energy where the LANSCE-WNR complex cannot compete with ORELA. The low-energy end of this gap is in the 100-eV to 1-keV region because of the limitations of LANSCE discussed above. The high-energy end of this gap is in the MeV region because WNR is penalized by its time structure at lower energies. WNR takes over above a few MeV because (1) its neutron spectrum is much harder than that of ORELA, (2) the width of the WNR microbursts is much smaller than that of the ORELA bursts, and (3) the number of microbursts per second at WNR can be increased above the ORELA maximum repetition frequency of 1,000 Hz. But even in this energy range, WNR could do better with a more suitable time structure. Several improvements to WNR can therefore be suggested.

(1) WNR could be equipped with a target-moderator system to produce moderated neutrons. This possibility has already been anticipated because two target mechanisms are already available. This simple addition would enable users to make measurements with reasonable accuracy below about 100 keV, though with a lower flux as at ORELA.

(2) More attention should be given to those flight paths at right angles that are the best suited for high-resolution measurements, especially with moderated neutrons. At the present time, most of the WNR flight paths are predominantly at forward angles. This is justified for measurements with very high-energy neutrons. But for measurements at lower energies, smaller inclination angles Θ are preferable. Although two flight paths exist at right angles, their lengths are very short (7 and 8 m) and should be extended, though the extension may be limited for practical reasons.

(3) The repetition rate of the macrobursts could be increased beyond its present value of 40 Hz by simply upgrading the switchyard kicker.

(4) The main improvement should be made on the time structure, which is not suited for TOF experiments over a wide neutron energy range. Although the time structure was greatly improved with the PSR for LANSCE, its use, as was discussed above, is restricted to low energies. A similar improvement could be considered for WNR,

whereby a PSR would preserve the original fine structure of the proton beam. A similar project was already contemplated several years ago as the short-bunch mode of operation for PSR.[12] As an illustration, we can make an estimate of the gain in neutron flux that could be expected from the ring we have in mind. This can provide at least a basis from which the experts can make a feasibility study from a concrete request.

In order to estimate the gain in neutron flux that could be obtained, the following assumptions are tentatively made.

(1) The repetition frequency of the WNR macrobursts is kept to 40 Hz for consistency with the previous calculations.

(2) The LAMPF linac is operated in the bunched mode with a time interval of 60 ns between two successive micropulses (instead of a minimum of 360 ns at the present time). These $\frac{6.25 \times 10^5}{60} \simeq 10^4$ micropulses in each macropulse are stored in the ring during the whole duration of the macropulse. The consequences of the H^- beam loading in the linac are not considered here.

(3) The storage of these micropulses is synchronized in such a way that they are stacked one on the other in six pulses. Therefore, at the end of the macroburst, there are six bursts in the ring, each one resulting from the stacking of 1.7×10^3 micropulses separated by 60 ns.

(4) The storage is such that the microstructure is preserved, with each of the six pulses in the ring having a duration of about 1 ns.

(5) The storage can last as long as the time duration between two macrobursts: 24.375 ms.

(6) These stored pulses can be ejected at regular 4-ms intervals during this time duration of 24.375 ms.

The net result of this storage is that WNR would run with 1-ns microbursts, each one consisting of 5.2×10^{12} protons at a repetition rate of $40 \times 6 = 240$ Hz.

The results that would be obtained with such a ring installed at WNR are given in the same manner as previously in Figs. 29-34 using the numerical values presented in Tables 11 and 12 for RP1 and RP2, respectively.

The improvement that would be obtained in neutron flux with the use of such a PSR is spectacular over the whole energy range.

For example, for RP1 and for moderated neutrons, the gain in neutron flux with the use of a PSR would be very substantial and increase steadily with neutron energy, from 83 at 1 eV to about 5.7×10^4 at 100 keV. Equipped with a PSR, WNR would then match LANSCE at very low energy and even provide a bigger neutron flux at higher energy by a factor of 6 at 1 keV. With a PSR, WNR would provide neutron fluxes higher than those of ORELA by 2 to 3 orders of magnitude over the entire range of moderated neutrons.

Also for RP1, but for fast neutrons, the use of a PSR would greatly improve the WNR capability over the whole neutron energy range. Improvements would range from 5 orders of magnitude in the 100-keV region to about a factor of 12 in the 100-MeV region. The great advantage, at high energy, of the existing WNR over LANSCE and ORELA would then be enhanced.

Similar conclusions can be drawn for RP2.

Therefore, the use of a PSR at WNR would give this facility a tremendous upgrade that would make it by far the best TOF facility in the world for neutron-nuclear physics. WNR equipped with a PSR would be far superior to ORELA even in the 1-keV to 1-MeV range where ORELA has some advantage at the present time. The great value of undertaking a feasibility study of such a ring is evident.

It should be pointed out that the above assumptions may have to be changed, taking into account the results of the feasibility study and also a more thorough assessment of the experimental requirements.

E. Lead slowing-down spectrometer

The use of the neutron TOF method described above is very powerful, especially because it makes possible simultaneous measurements over a very wide energy range with a great number of energy points and great precision. But this TOF method uses only those neutrons that are emitted into a very small solid angle and therefore wastes a great number of neutrons.

Another approach consists in using the slowing-down properties of neutrons inside a given medium of large dimensions. When a pulsed point source of neutrons of a given energy is placed in this medium, the neutrons migrate away from the source while

being moderated. At a given distance from the source, a correlation exists between the time of arrival of the neutrons and their energy. The heavier the material surrounding the source is, the more pronounced this correlation becomes.

It can be shown that, when a very short burst of fast neutrons is injected at a given time in an infinite medium of nuclei having mass number A, the slowed-down neutrons have the following time properties:

$$\langle x \rangle = \frac{3A \times (A + 1)}{3A - 1} \quad \text{and} \tag{30}$$

$$\mathrm{Var}(x) = \langle x^2 \rangle - \langle x \rangle^2 = \frac{3(A + 1)^2 \times (2A - 1)}{(3A - 1)^2}, \tag{31}$$

where $x = \frac{v_n \times t_n}{l_n}$ (v_n and t_n are the velocity and the slowing-down time of the neutron, respectively), and l_n is the mean free path, assumed to be constant at low energy.[11]

Eqs. 30 and 31 show that the relative width of the time distribution function is given by

$$\frac{\sqrt{\mathrm{Var}(x)}}{\langle x \rangle} = \sqrt{\frac{2}{3A}} \tag{32}$$

for $A >> 1$.

This expression shows the importance in using a heavy material such as lead, which, in addition, has a low-absorption cross section. The resolution that can be obtained in this manner is mediocre (about 30% in actual practice), but the great advantage is that the neutrons are kept in the moderating material, and, consequently, large neutron fluxes at the sample position are available.

Such a spectrometer is installed at the linac of the Rensselaer Polytechnic Institute (RPI) and is called the Rensselaer Intense Neutron Spectrometer (RINS). Experiments carried out with this spectrometer showed count rates superior by a factor of 10^3 to 10^4 to those obtained with the conventional TOF method at the shortest available distance.[13]

In measurements using the RINS, the relation between the energy E_n and the slowing-down time t_n is given by

$$E_n = \frac{165000}{(t_n + 0.3)^2}, \qquad (33)$$

where E_n and t_n are expressed in eV and in microseconds, respectively.

Equation 33 shows that a similar relation would hold for a conventional TOF measurement with a flight path of 5.6 m. However, a much better resolution would be obtained by conventional TOF methods.

Fission cross-section measurements of ^{247}Cm, ^{250}Cf, and ^{254}Es were recently made with the RINS.[14] As an illustration, the ^{247}Cm fission cross section thus obtained with a sample of 3.16 μg of ^{247}Cm is presented in Fig. 35.

From the count rates recorded with the RINS, it seemed that a more conventional TOF measurement (in beam geometry), made at LANSCE with the same fission chamber and a short flight path, would compete very well with the RINS results.

These considerations stimulated a recent measurement of the same fission cross sections at LANSCE with the same fission chamber and a flight path of 7.25 m (close to the shortest available distance). These results are illustrated in Fig. 35 where the ^{247}Cm fission cross section thus obtained is plotted as a function of the neutron energy.[14]

Comparison of the RINS and LANSCE data in Fig. 35 shows that the RINS can correctly detect the first resonances in the ^{247}Cm fission cross section. But, above these first resonances, the resonance structure in the RPI results is washed out by the poor resolution of the lead slowing-down spectrometer. On the contrary, the LANSCE results clearly show the existence of a detailed resonance structure and thus demonstrate the much better energy resolution (about 10 times better) obtained at LANSCE compared with that of RPI.

The count rates per burst are comparable for both measurements, whereas the average count rate at LANSCE is about 30% that at the RINS.

These measurements demonstrate the strong potential of LANSCE for making measurements in a conventional geometry with very small samples, in microgram or even submicrogram quantities. But these measurements demonstrate also the strong interest in using a lead slowing-down spectrometer with the PSR proton beam. Count rates still higher by 3 to 4 orders of magnitude would then be obtained. Measurements with even smaller samples would then become possible. For example, the fission cross-section measurements referred to above, made with microgram quantities,

could become possible with quantities as small as nanograms or even a fraction of a nanogram.[15]

It must be noted that the use of a lead slowing-down spectrometer with an electron linac such as that of RPI is limited in neutron flux not by the available electron beam power from the accelerator but by the heat produced mainly from the bremsstrahlung and dissipated in the lead spectrometer. Therefore it does not seem possible to increase the neutron flux in a lead slowing-down spectrometer with more powerful electron machines, such as ORELA. On the other hand, lead slowing-down spectrometers can be used with higher fluxes on proton machines, such as the LAMPF-PSR facility, that are free of bremsstrahlung. Higher neutron fluxes may be limited by other factors and a feasibility study would be necessary to clarify these questions.

VI. CONCLUSION

The use of the LAMPF 800-MeV proton beam has already proved to be an excellent method for neutron production via spallation reactions. The full 1-mA proton beam, if it were totally used for that purpose would yield about 10^{17} neutrons s^{-1}, a factor of 10^3 greater than at ORELA.

But LAMPF, which was initially designed for intermediate-energy physics experiments, has a time structure not suited for neutron TOF spectroscopy. Therefore, to take full advantage of the great potential of LAMPF for neutron nuclear physics, the facility's time structure should be modified.

A great step forward was already made toward the use of LAMPF for such neutron work with the construction of the PSR now in operation at LANSCE. The time structure of LANSCE equipped with the PSR is well suited for studies with low-energy neutrons in the field of condensed matter. It is also well suited for nuclear physics studies with epithermal neutrons up to near 1 keV, and it is clearly superior to ORELA in this energy range. Note that LANSCE may have been underestimated for some experiments because our calculations took into account the standard deviation, not the shape, of the resolution function. Above about 1 keV, LANSCE is penalized by the width of a proton burst that is too wide and also by its moderator which gives too wide a time distribution. The width of the proton burst delivered by the PSR may be reduced at the cost of decreasing the intensity, but measurements need to be made to substantiate this possibility, which is expected to provide a substantial gain. Compensating for the relatively broad proton pulse now available at

LANSCE would require increasing the length of the flight paths--but at a loss of intensity and with physical limitations that need to be considered. Also, the target-moderator system could be improved to provide a narrower time-resolution function.

The WNR target is not presently equipped with a moderator, and, consequently, cannot compete with ORELA below about 1 MeV. Therefore, the LANSCE-WNR complex now presents a gap in the 1-keV to 1-MeV range that restricts the possibilities of this facility. As an illustration, a high-precision measurement of the total cross section of lead below 50 keV--a measurement aimed at determining the electric polarizability of the neutron--was first made at Harwell and then repeated with better precision at ORELA; however, this measurement cannot currently be done at Los Alamos National Laboratory. Therefore, WNR should also have a target with a moderator. But even in that case, WNR would have a lower flux than ORELA, because the WNR time structure is based on that of LAMPF and, so, is not the best suited for conducting TOF studies. Neutron work is carried out with an enormous waste of intensity by the need to eliminate most of the microbursts.

With the existing time structure of LANSCE and WNR, the LANSCE-WNR complex is superior to ORELA below about 1 keV and above about 1 MeV, but ORELA overtakes in this 1-keV to 1-MeV interval and would still do so even if WNR is equipped with a target-moderator system. The study of many targets with moderators has demonstrated that the advantage of ORELA in this 1-keV to 1-MeV range cannot be overcome by a suitable WNR target.

Though WNR can be improved by the addition of a good target-moderator system and by the modification of the flight paths (length and orientation), the major upgrade would nevertheless be the improvement of the time structure by stacking the microbursts in a PSR that would preserve the existence of these microbursts. Gains as high as 4 or 5 orders of magnitude could then be obtained in some energy ranges (for example, around 100 keV to 1 MeV). WNR would then become the most intense neutron source in the world (equivalent to LANSCE at low energy) and would exceed ORELA by 2 to 3 orders of magnitude below 1 MeV and even more for energies greater than a few MeV.

Finally, the installation of a lead slowing-down spectrometer, using the proton beam from the PSR, would make some cross-section measurements possible with minute samples, as small as nanogram quantities for fission studies. This would open a new field of measurements with very rare or very radioactive samples for which no measurements are now possible on any existing neutron source.

For example, the fission cross section of the ^{235}U isomeric state ($T_{½}$ = 26 min, $J^{\pi} = ½^{+}$) could be measured for the first time in the resonance region.

In summary, the LANSCE-WNR complex is already a very good neutron source used over a very wide neutron energy range for many purposes. But it is not used at its full potential yet because the initial construction of LAMPF was not meant for that purpose. If the upgrades proposed above could come to fruition, then the LANSCE-WNR facility would become the best pulsed neutron facility in the world over a very wide energy range from subthermal neutron energy to almost 1 GeV. It would far exceed the best existing facilities by a factor that could be as high as 3 or 4 orders of magnitude in some energy regions.

Such a facility would play a very important and unmatched role in providing the basic neutron-nuclear scientific and technical data that will be needed for the development of nuclear energy, whether for the design and the operation of nuclear energy systems (fission and fusion) or for the fuel cycle (nuclear incineration of hazardous nuclear waste, for example). Nuclear-data needs may also arise from other developments like very intense spallation-neutron sources. Also, the availability of much greater neutron fluxes could trigger a renaissance of basic neutron physics over a very wide energy range.

Note that all the proposed upgrades presented in this report leave the LAMPF accelerator itself untouched. The proposed upgrades try simply to make a better use of the existing LAMPF proton beam. This means that the investment costs of these improvements would stay within reasonable limits.

ACKNOWLEDGEMENTS

The authors are very grateful to G. J. Russell for the supply of the Monte Carlo calculations that were essential for this study. The authors are also very much indebted to R. C. Haight, G. L. Morgan, and M. S. Moore for careful reading of the manuscript and for many useful comments.

REFERENCES

1. J. C. Allred, and B. Talley, "LAMPF," Los Alamos National Laboratory Internal Report, LA-UR-87-327, January 1987.
2. P. W. Lisowski, C. D. Bowman, G. J. Russell, and S. A. Wender, Nucl. Sci. and Eng. **106**, 208 (1990).
3. J. W. T. Dabbs, Invited Paper, Proceedings of the International Conference on Nuclear Cross Sections for Technology, Held at the University of Tennessee, Knoxville, Tennessee, USA, October 22-26, 1979, J. L. Fowler, C. H. Johnson, and C. D. Bowman, Eds., National Bureau of Standards Special Publication 594, 929 (September 1980).
4. G. J. Russell, Los Alamos National Laboratory Report, to be published (1990).
5. R. W. Peele, Private Communication (1990).
6. C. Coceva, R. Simonini, and D. K. Olsen, Nucl. Inst. and Methods, **211**, 459 (1983).
7. W. E. Lamb, Phys. Rev. **55**, 190 (1939).
8. L. W. Weston, Intralaboratory Correspondence, Oak Ridge National Laboratory (January 30, 1981).
9. R. G. Alsmiller, Jr., T. A. Gabriel, and M. P. Guthrie, Nucl. Sci. and Eng. **40**, 365 (1970).
10. C. E. Burgart, E. A. Stracker, T. A. Love, and R. M. Freestone, Nucl. Sci. and Eng. **42**, 421 (1970).
11. A. Michaudon, Reactor Science and Technology (J. Nucl. En., Parts A/B), **17**, 165 (1963).
12. G. F. Auchampaugh, Invited Paper, Proceedings of the International Conference on Nuclear Cross Sections for Technology, Held at the University of Tennessee, Knoxville, Tennessee, USA, October 22-26, 1979, J. L. Fowler, C. H. Johnson, and C. D. Bowman, Eds., National Bureau of Standards Special Publication 594, 920 (September 1980).
13. R. C. Block, R. E. Slovacek, Y. Nakagome, and R. W. Hoff, Proceedings of the International Conference "Fifty Years with Nuclear Fission," Held at Gaithersburg, Maryland, USA, April 26-28, 1989, J. W. Behrens, and A. D. Carlson, Eds., Published by the American Nuclear Society, 354 (1989).
14. Y. Danon, R. E. Slovacek, R. C. Block, R. W. Lougheed, R. W. Hoff, and M. S. Moore, submitted to Nucl. Sci. and Eng. (1990).

15. M. S. Moore, P. E. Koehler, A. Michaudon, A. Schelberg, Y. Danon, R. C. Block, R. E. Slovacek, R. W. Hoff, and R. W. Lougheed, Invited Paper, Seventh International Symposium on Capture Gamma-Ray Spectroscopy and Related Topics, Asilomar, Pacific Grove, California, October 14-19, 1990.

APPENDIX A

BASIC FORMULAS USED IN NEUTRON TIME-OF-FLIGHT SPECTROSCOPY

The neutron TOF can be derived from the basic relation between the kinetic energy E_n and the momentum p_n of the neutron. In a relativistic treatment, the neutron total energy E_T (including the rest-mass energy) is given by the following relation:

$$E_T = E_n + M_n c^2 = [\ (M_n c^2)^2 + (p_n c)^2\ ]^{1/2}. \qquad (A.1)$$

Elementary algebra gives the following relation between the TOF and the kinetic energy:

$$\frac{t_n}{L} = \frac{1}{v_n} = \frac{1}{c} \times [1 + \frac{(M_n c^2)^2}{E_n(E_n + 2M_n c^2)}\ ]^{1/2}, \qquad (A.2)$$

where t_n is the TOF of the neutron over a distance L.

The low-energy limit ($E_n \ll M_n c^2$) leads to the well-known expression

$$\frac{t_n}{L} = \frac{1}{c} \times \sqrt{\frac{M_n c^2}{2E_n}} = \frac{72.298}{\sqrt{E_n(eV)}} (\mu s/m). \qquad (A.3)$$

The relativistic correction R_t to the TOF, defined as the ratio of the relativistic to the classical values, is obtained by the ratio of Eqs. (A.2) and (A.3):

$$R_t = \frac{t_n(relativistic)}{t_n(classical)} = [2 \times \frac{E_n(E_n + 2M_n c^2) + (M_n c^2)^2}{(E_n + 2M_n c^2) \times M_n c^2}\ ]^{1/2}. \qquad (A.4)$$

When developed to first order at low energy, this expression reads

$$R_t = 1 + \frac{3}{4} \times \frac{E_n}{M_n c^2} + \ldots . \qquad (A.5)$$

The relativistic correction to the TOF is therefore about 1% for 14-MeV neutrons.

The energy spread ΔE_n associated with a time spread Δt_n is obtained by differentiating both sides of Eqs. (A.2) and (A.3) for the relativistic and classical cases, respectively. One then obtains

$$\Delta E_n = \frac{[E_n(E_n+2M_nc^2)+(M_nc^2)^2]^{1/2}\times[E_n(E_n+2M_nc^2)]^{3/2}}{(M_nc^2)^2\times(E_n + M_nc^2)} \times \frac{c\times\Delta t_n}{L} \qquad (A.6)$$

for the relativistic case, and

$$\Delta E_n = 2c\sqrt{\frac{2}{M_nc^2}} \times E_n^{3/2} \times \frac{\Delta t_n}{L} = 0.02766 \times E_n^{3/2} \times \frac{\Delta t_n}{L} \qquad (A.7)$$

for the classical case, where ΔE_n and E_n are in eV, and $\frac{\Delta t_n}{L}$ is in microseconds per meter.

The relativistic correction R_e to the energy spread, defined again as the ratio of the relativistic values to the classical values, is given by the ratio of Eqs. (A.6) and (A.7) as

$$R_e = \frac{\Delta E_n(\text{relativistic})}{\Delta E_n(\text{classical})} = \frac{[2E_n+M_nc^2]^{1/2}\times[E_n+2M_nc^2]^{3/2}}{2\sqrt{2}\times M_nc^2\times(E_n + M_nc2)}. \qquad (A.8)$$

When developed to first order at low energy, this relativistic correction then reads

$$R_e = 1 + \frac{3E_n}{4M_nc^2} + \ldots . \qquad (A.9)$$

The calculations presented in Chapter IV were made with the exact relativistic expressions.

APPENDIX B

SHAPES OF THE LANSCE TIME-RESOLUTION FUNCTIONS

The time profile of a burst of moderated neutrons emitted at LANSCE depends on the time distribution of the incident proton burst and the time response of the target-moderator system.

The shape of the proton burst, g(t), from the PSR is reasonably well approximated by an isosceles triangle with an FWHM of 125 ns (and a standard deviation σ_b = 51 ns). The response of the target-moderator system, f(t), with a standard deviation σ_{tm}, is derived from Monte Carlo calculations and depends on the geometry and composition of both the target and the moderator. The overall shape of the neutron burst, F(t), at the exit of the moderator is the convolution of the functions f(t) and g(t):

$$F(t) = \int g(t') * f(t' - t)\, dt'. \qquad (B.1)$$

We have calculated the function F(t), using Eq. B.1 and the known functions f(t) and g(t), for incident energies of 1 eV, 10 eV, 100 eV, 1 keV, 10 keV, and 100 keV. The standard deviation σ_t of the function F(t) can be obtained either by adding σ_b and σ_{tm} in quadrature, as in the text, or by numerical integration, using directly the function F(t) calculated with Eq. B.I. These two methods give very similar results, as expected. The values of σ_{tm} and of σ_t are given in Table B.I. This table illustrates that, below about 100 eV, the value of σ_t is dominated by that of σ_{tm}, which is greater than σ_b = 51 ns. At higher energies, the effect of the proton pulse becomes more and more important with energy.

An additional complication is that the function, F(t), is not a Gaussian at least at low energies. Frequently, this function is asymmetric with a tail that may extend to long times, and this tail may contribute significantly to the calculation of the standard deviation σ_t. In such cases, it is not correct to assume that the FWHM of F(t) is simply 2.34 × σ_t. When the function F(t) is very asymmetric, with a long tail, its FWHM may be significantly smaller than 2.34 × σ_t.

For simplification, let us assume that the asymmetric time-resolution function, F(t), can be assimilated to a Gaussian, having σ_g for standard deviation and a reduced flux, accompanied by a tail that takes the rest of the flux. The fraction of the neutron flux in the Gaussian part, relative to the total flux, is called f_I.

The effect of such an asymmetric shape of F(t) on a measurement is difficult to assess because it depends on the experiment. For example, if the study is made on a single well-isolated resonance, the asymmetric resolution function will broaden the shape of the resonance, and the observed shape will also be asymmetric. However, the FWHM of the measured shape will be very close to that obtained with the Gaussian part of the resolution function only. In addition to distorting the shape of the resonance, the tail will add some background in the measurement. For more complicated cases, such as for cross sections composed of closely spaced resonances, the effect of the tail is much more difficult to assess but can lead to serious difficulties when analyzing the data.

At best, we can consider that only the Gaussian part of F(t) plays a role in the estimate of the experimental resolution, with the tail ignored and considered as background only.

Listed in Table B.I are the values of σ_g derived from the shape of F(t) and the ratios $R = \sigma_t/\sigma_g$, which are always greater than one, as expected. If the tail can be neglected, the flight-path lengths calculated for LANSCE in this report should be decreased by the same factor R, and the flux at the end of these shorter flight paths should be multiplied by $N_I = R^2 \times f_I$ (also given in Table B.I).

Therefore, the calculations presented in the text may underestimate LANSCE, particularly at low energy. The amount of the underestimation is difficult to evaluate because it depends on the energy and on the experiment that is considered, but the values of N_I obtained in the above provide an upper limit of this amount.

TABLE B.I

E_n (ev)	σ_{tm} (μs)	σ_t (μs)	σ_g (μs)	σ_t/σ_g	f_I	N_I
1	1.8	1.9	0.73	2.6	0.86	5.7
10	1.1	1.2	0.27	4.3	0.79	14.4
10^2	0.48	0.55	0.13	4.4	0.81	15.4
10^3	0.20	0.21	0.08	2.7	0.81	5.7
10^4	0.068	0.086	0.071	1.2	0.96	1.4
10^5	0.022	0.065	0.061	1.1	1.0	1.1

APPENDIX C

CHARACTERISTICS OF TARGETS CONSIDERED FOR WNR

The targets considered for WNR are all made of tungsten with a total length of either 30 cm with a re-entrant hole of 5 cm or 25 cm without a re-entrant hole. These lengths have been chosen to match the range of 800-MeV protons in tungsten, which is about 25 cm. Such long target lengths give the maximum neutron output without penalty on the distance uncertainty because we consider neutron beams perpendicular to the proton beam only. But a long length may also increase the neutron time spread because of the time it takes the incident protons to cross the target. This last effect is discussed in Sec. IV.G.

The set of three WNRB targets consists of

(1) a cylinder having ϕ = 3 cm and l = 30 cm (called WNR1), which is very similar to the target being used now except for the length;

(2) a parallelepiped having a square cross section of 3 × 3 cm^2 and a length of 30 cm (called WNR2); and

(3) a slab having a thickness of 3 cm and a lateral area of 30 × 30 cm^2 across the direction of the flight path (called WNR3).

A re-entrant hole of 0.5 cm in diameter and 5 cm in depth has been bored in these three targets to increase the neutron production.

The set of three WNRM targets consists of

(1) a cylinder, which has ϕ = 3 cm and l = 25 cm, immersed in a water moderator that has a slab shape with an area of 30 × 30 cm^2 across the neutron beam and a thickness varying between 5 and 11 cm. This type of target is called WNR4.

(2) a cylinder, which has ϕ = 3 cm and l = 25 cm, immersed in a water moderator that has the shape of a parallelepiped of 9 × 30 cm^2 area across the neutron beam and a thickness of 9 cm. This type of target is called WNR5.

(3) a slab, which has a cross-sectional area of 30 × 30 cm^2 and a thickness of 3 cm, sandwiched between two slabs of water

of equal thicknesses with the same area of 30 × 30 cm^2. The overall thickness of this target-moderator system (called WNR6) varies between 7 and 11 cm.

All WNRM targets have a hole (3 cm in diameter and 5 cm in depth) either in the moderator (WNR4 and WNR5) or in the tungsten (WNR6) in their front side to increase the neutron production.

LIST OF SYMBOLS

c	Velocity of light.
f_b	Repetition frequency of the charged-particle bursts for ORELA and for LANSCE.
f_{rf}	Frequency of the radio wave for ORELA.
f_M	Maximum repetition frequency of the charged-particle burst.
p_n	Neutron momentum.
v_n	Neutron velocity.
t_n	Neutron TOF.
D_c	Duty cycle of the charged-particle burst, averaged over any possible microstructure.
E_n	Incident neutron energy.
F_b	Repetition frequency of the proton bursts for WNR.
I_p	Average current of the proton beam.
J_b	Energy in a charged-particle burst.
L	Length of the flight path.
L_m	Minimum value of the flight path length.
M_n	Neutron mass.
N_b	Neutron emission per burst, expressed in neutrons per burst, per eV, and per steradian.
N_{lk}	Neutron leakage from the source, expressed in neutrons per steradian, per MeV, and per incident proton for LANSCE and WNR and expressed in neutrons per steradian, per eV, and per joule of electron energy for ORELA.
N_μ	Number of microbursts in a charged-particle burst.
P_e	Peak power of the ORELA electron burst, averaged over the microstructure.
R	Nominal resolution in a TOF experiment, obtained as the ratio of the neutron time spread, Δt_n, to the flight-path length, L.
R_A	Maximum recoil energy of a nucleus with mass number, A, struck by a neutron of energy, E_n.
T_{eff}	Effective temperature used in the Doppler broadening in a TOF experiment made with a sample at temperature T.
ϕ	Diameter of the cylindrical tungsten target for WNR.
σ_b	Standard deviation of the charged-particle burst.
σ_i	Standard deviation of component, i, in the overall time-resolution function.
σ_m	Standard deviation of time distribution brought about by the moderator.
σ_t	Standard deviation of the time-distribution function.

σ_s Standard deviation of the transit times of the electrons, the photons, and the fast neutrons inside the ORELA target.

σ_{tm} Standard deviation of the neutron time spread in the target-moderator system, assuming that the charged-particle burst is a δ-function in time.

σ_D Standard deviation of the Doppler broadening.

τ Mean neutron collision time in the moderator.

σ_E Standard deviation of the energy-resolution function.

σ_{Lm} Value of σ_t obtained with a flight-path length, L_m.

Δ Doppler width.

Δt_b Charged-particle burst width.

Δt_n Neutron time spread.

Δt_{tm} Neutron time spread in the target-moderator system.

ΔE_n Neutron energy spread associated with time spread, Δt_n.

ΔL Distance uncertainty in a TOF experiment.

Φ Diameter of a circular FOV.

Φ_n Neutron flux.

Γ Natural width of a neutron resonance (FWHM).

Θ Inclination of the flight path relative to the normal to the moderator.

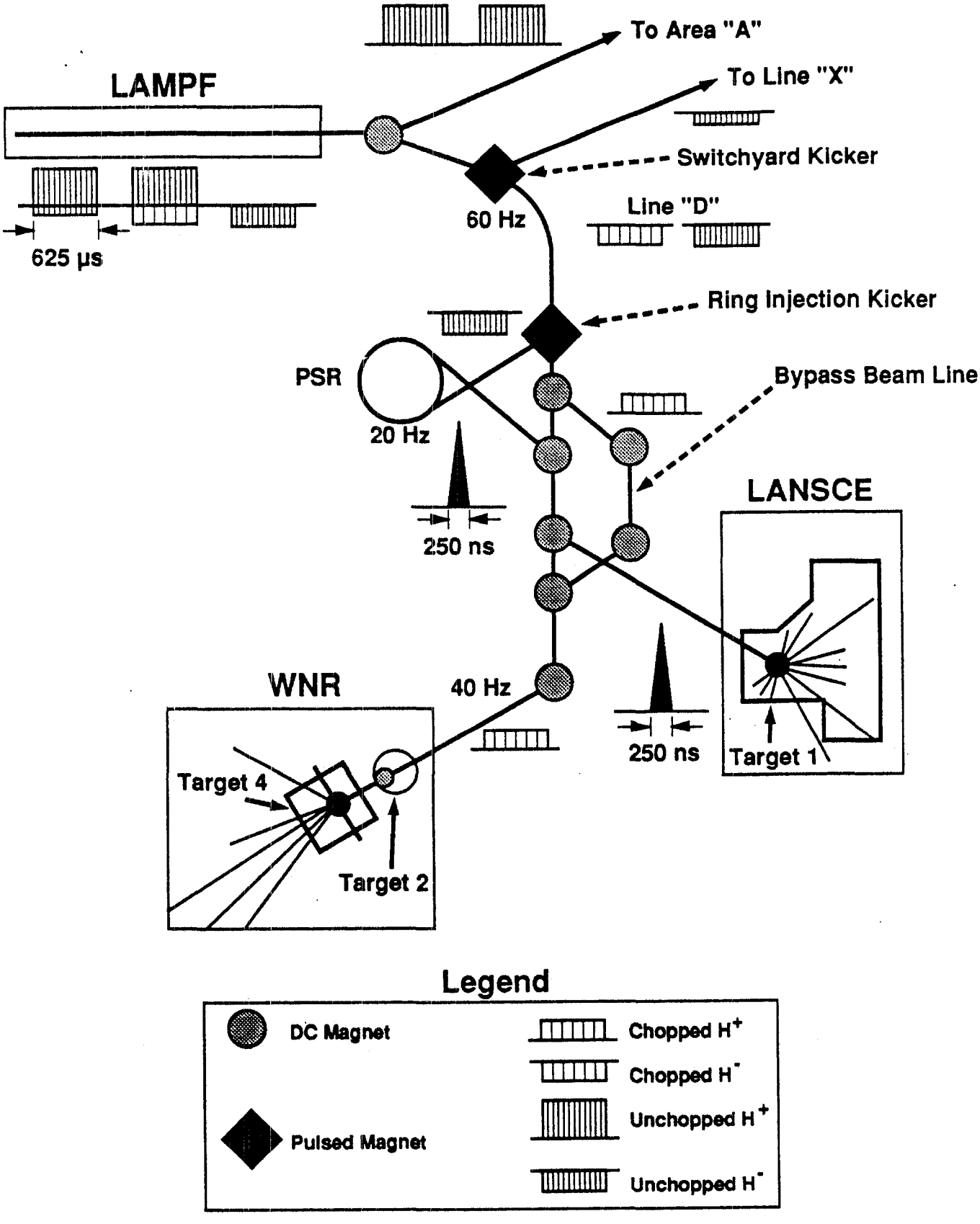

Fig.1. Simplified schematic of the LAMPF beam transport system. The macropulses are indicated as an illustration of the modes of operation of these facilities.

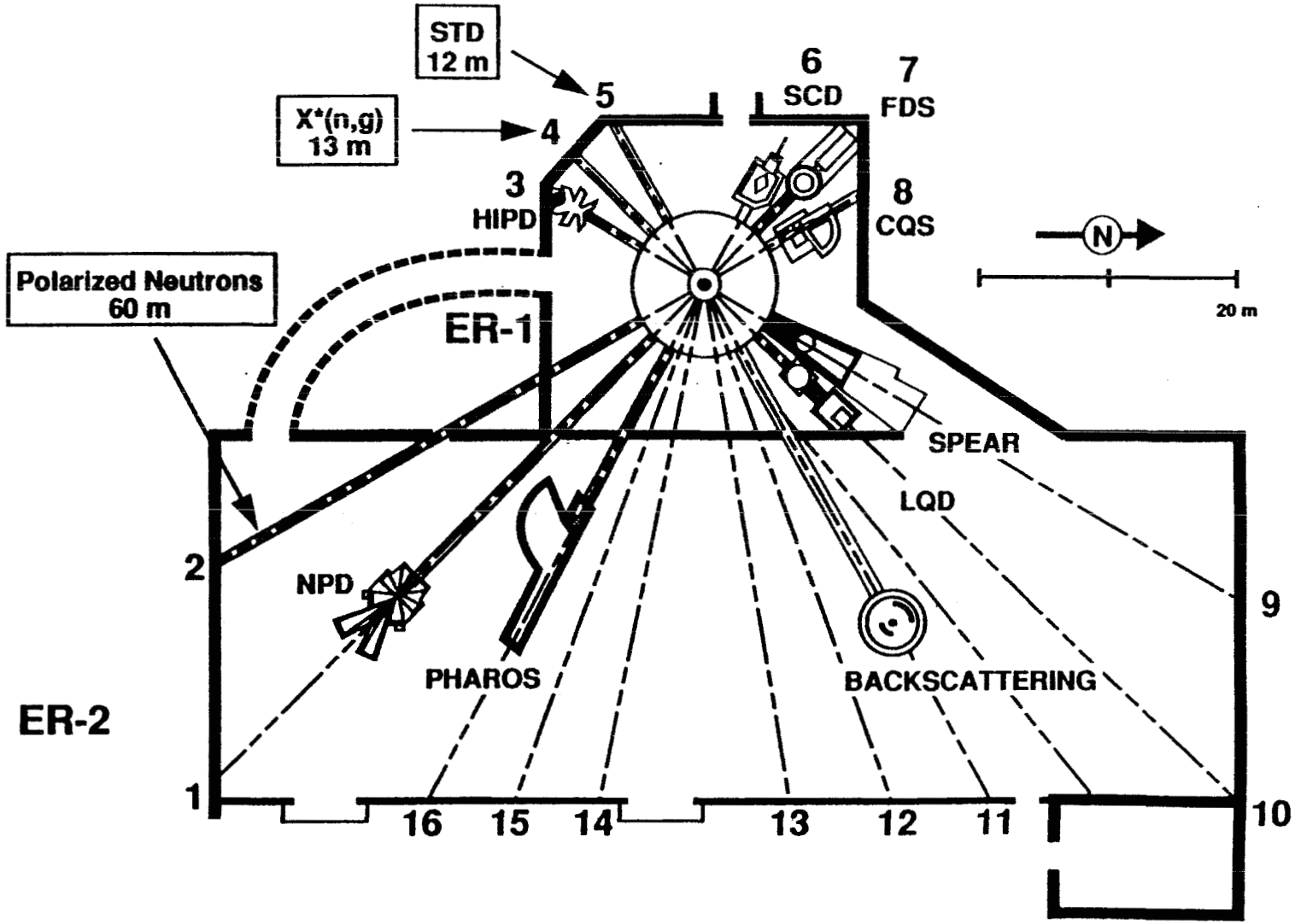

Fig. 2. Flight-path layout of the LANSCE target area. Flight paths labeled 2, 4, and 5 are dedicated to nuclear-physics experiments. Flight path 2 presently has a length of 60 m and is used for polarized neutron studies of parity violation. Flight path 4 has a 4π BaF_2 detector for capture measurements on radioactive samples. Flight path 5 is used for the study of transient phenomena by Bragg-edge diffraction. The other neutron beam lines are used for condensed-matter studies with spectrometers indicated for each beam line.

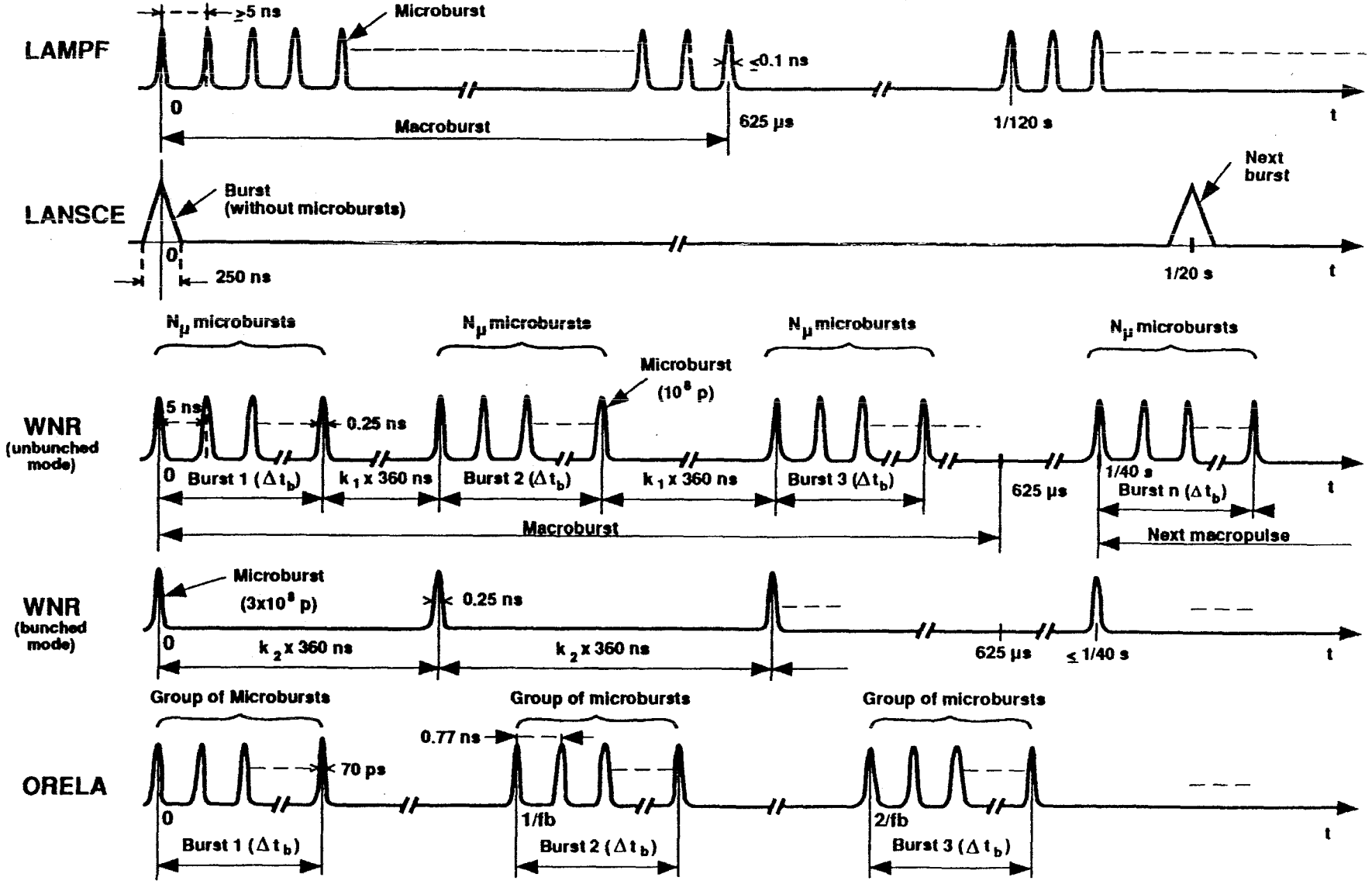

Fig. 3. Time structure of the charged-particle beams of the ORELA, LANSCE, and WNR facilities. *These figures are given as illustrations and are not drawn to scale.*

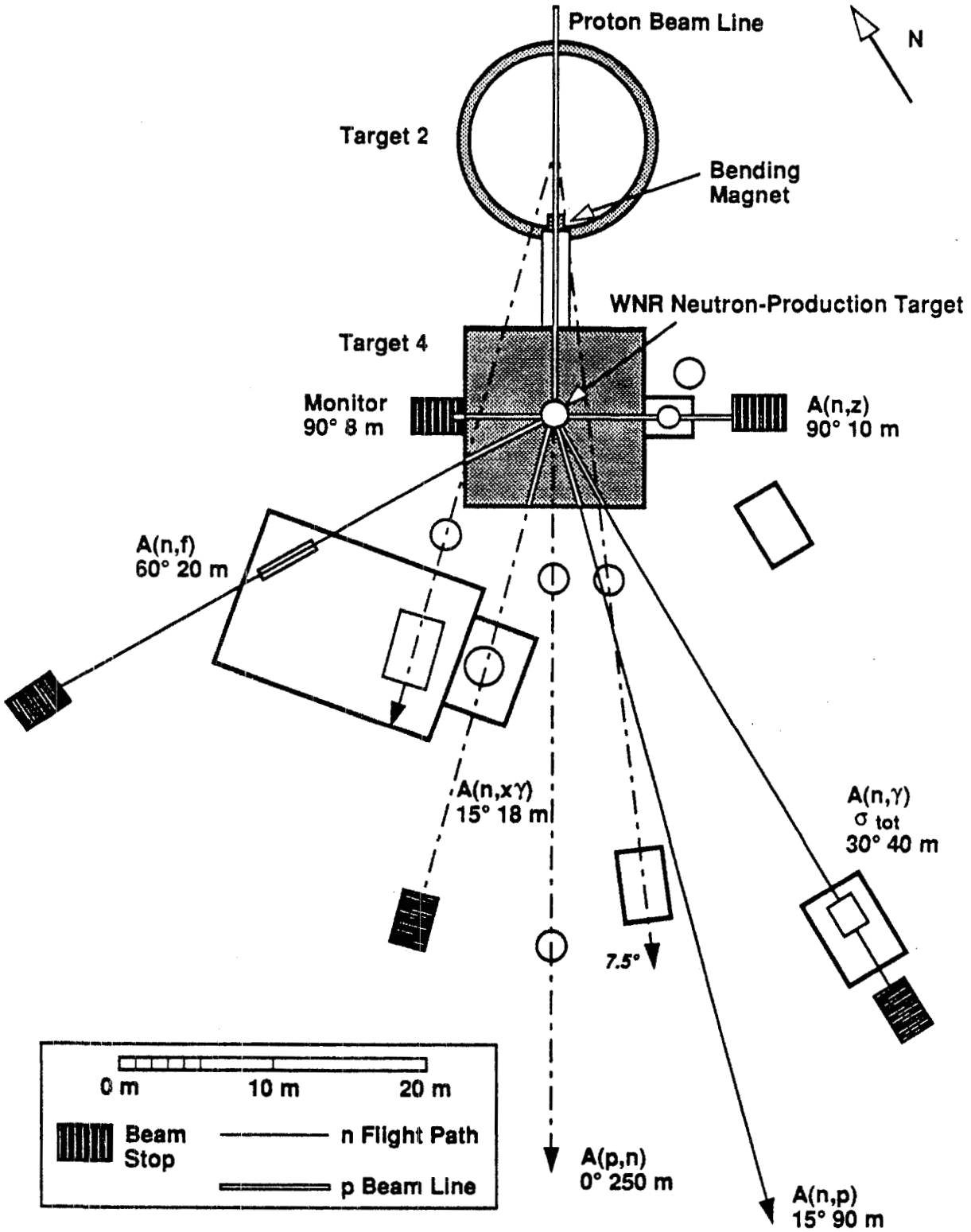

Fig. 4. General layout of the WNR experimental yard.

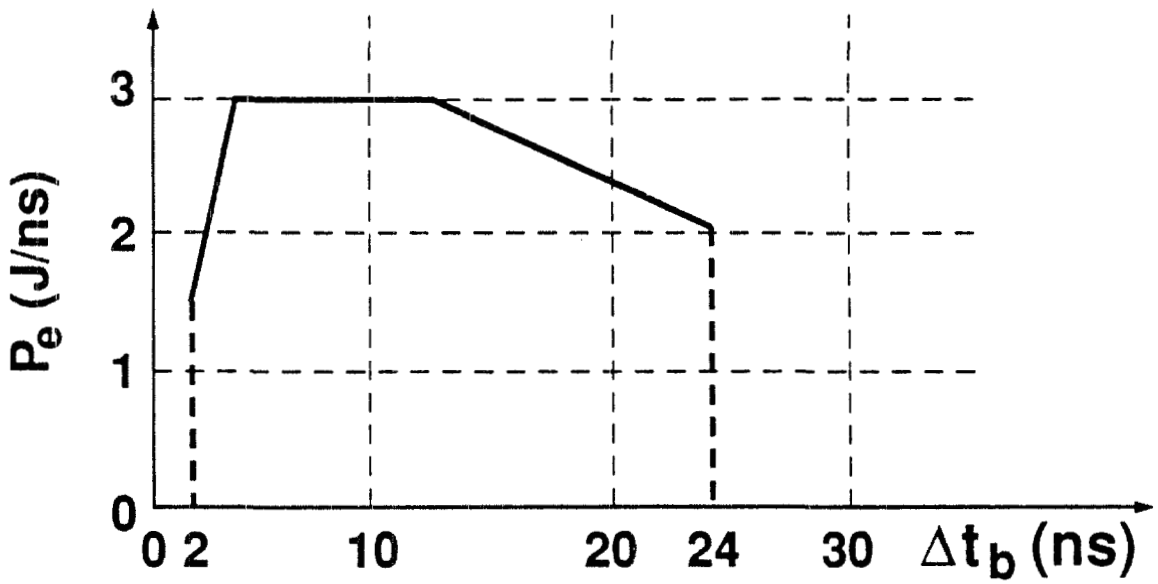

Fig. 5. Simplified representation of the instantaneous power P_e (in joules per nanosecond) in the electron burst at ORELA, averaged over the fine structure in the burst, as a function of the burst width Δt_b (in nanoseconds) between 2 and 24 ns. Bursts shorter than 2 ns cannot be obtained because of limitations in the electron gun. Bursts longer than 24 ns are not worth using for TOF experiments because they do not increase the energy of the electron burst while being detrimental to the energy resolution.

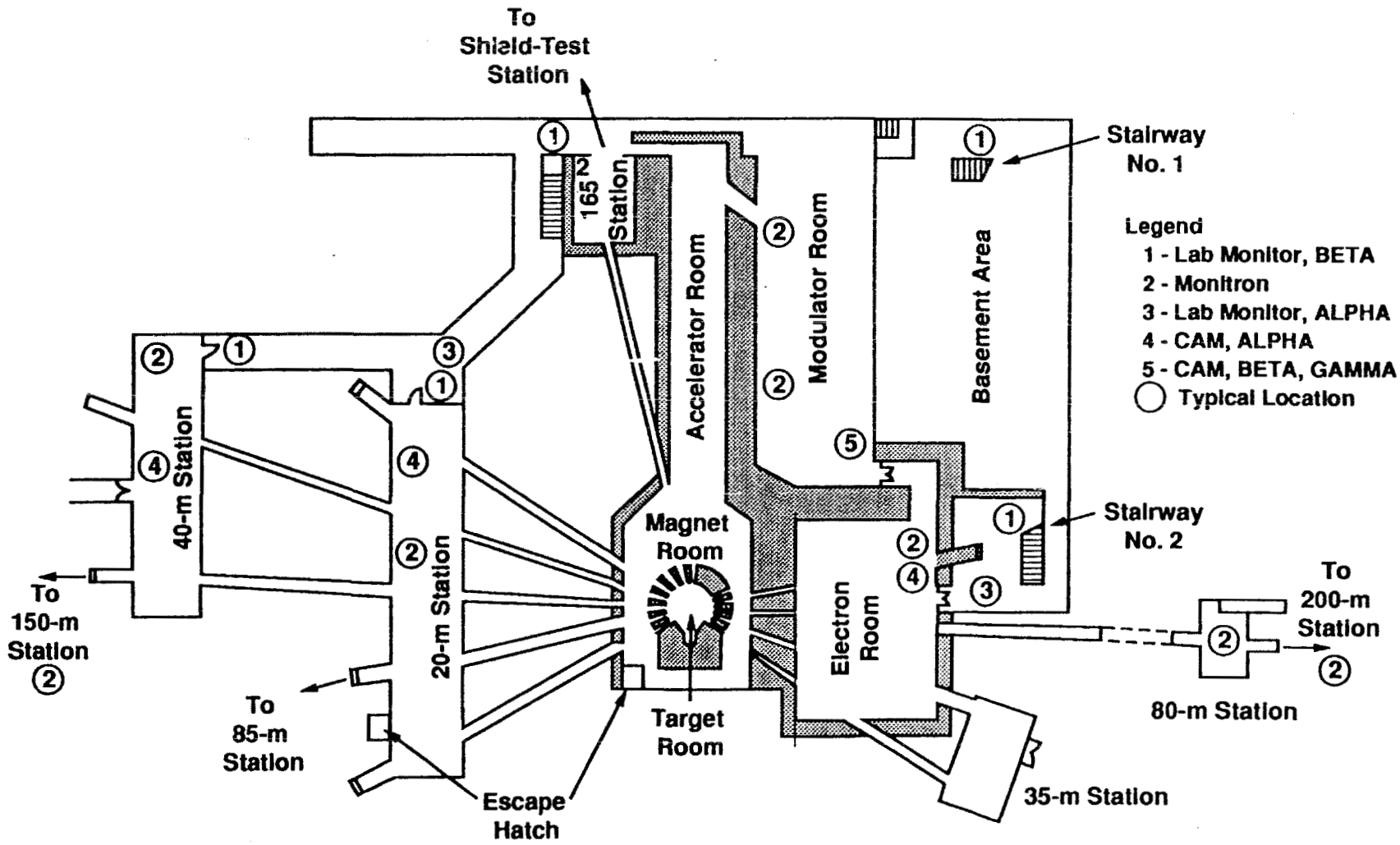

Fig. 6. General layout of the ORELA facility.

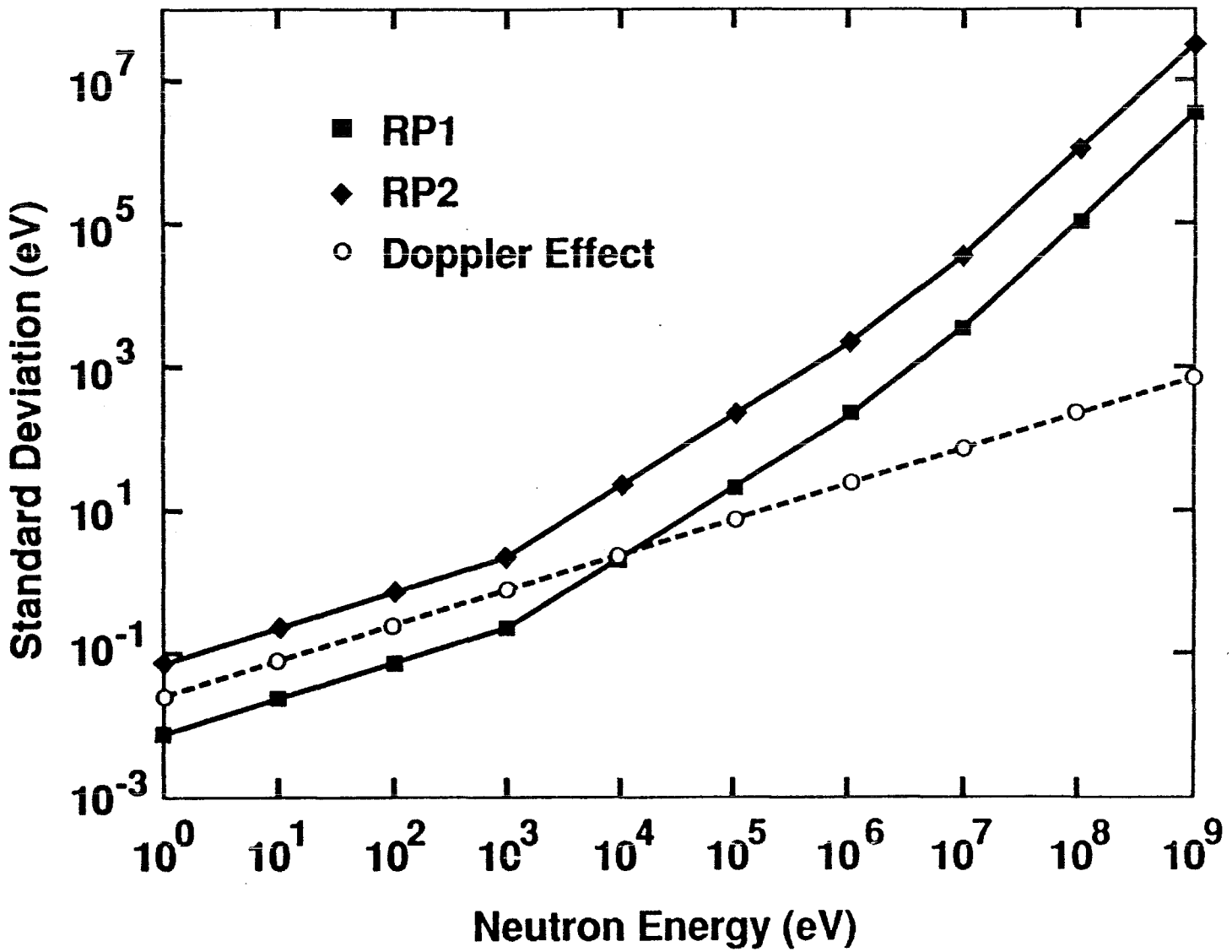

Fig. 7. Standard deviation of the energy-resolution profiles RP1 and RP2. The standard deviation for the Doppler effect calculated with T_{eff} = 300 K, and A = 100 is also shown for comparison.

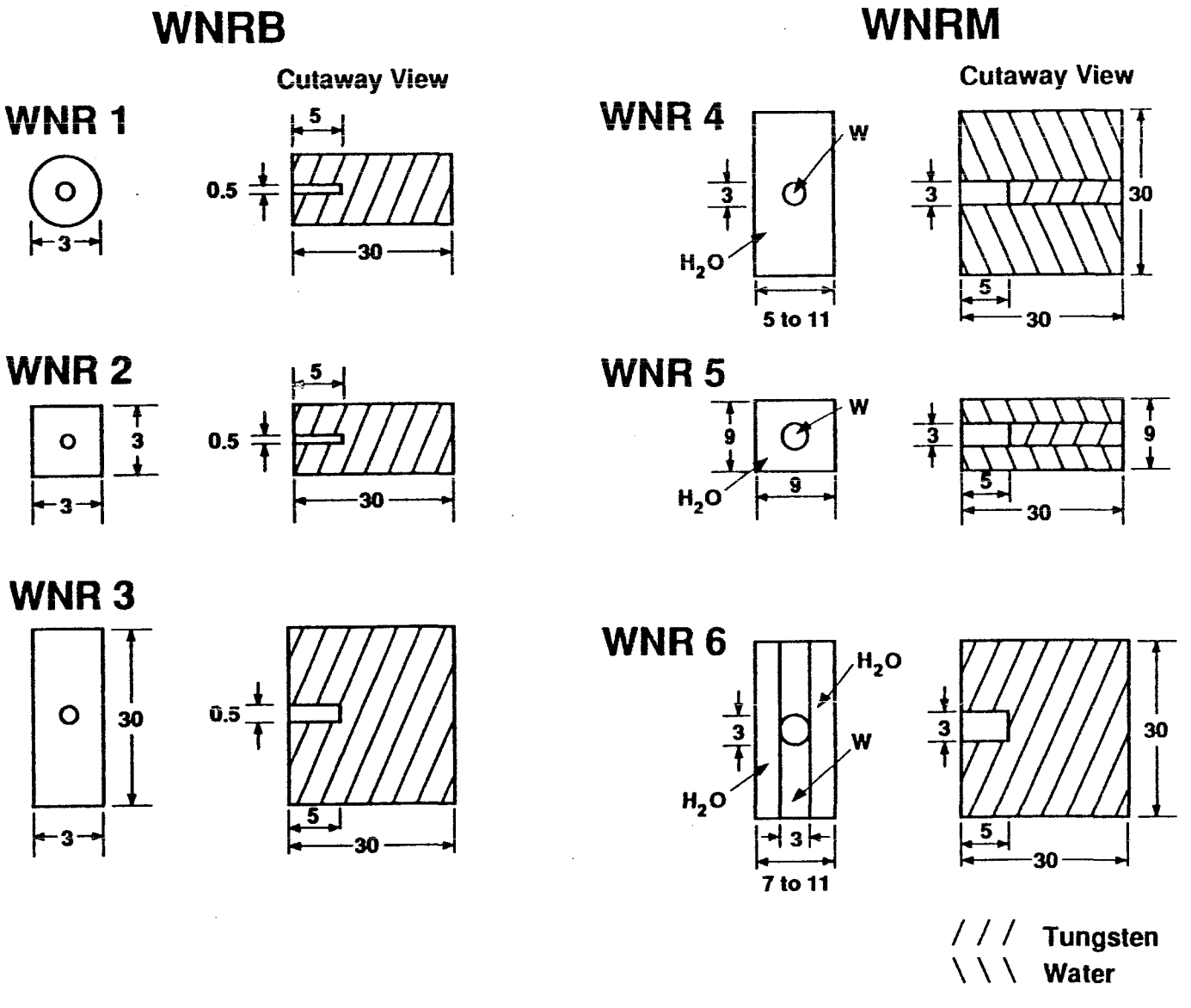

Fig. 8. WNR targets used in the calculations. The WNRB targets are made of tungsten only, whereas the WNRM targets are made of tungsten surrounded by water used as a moderator. All dimensions are given in centimeters.

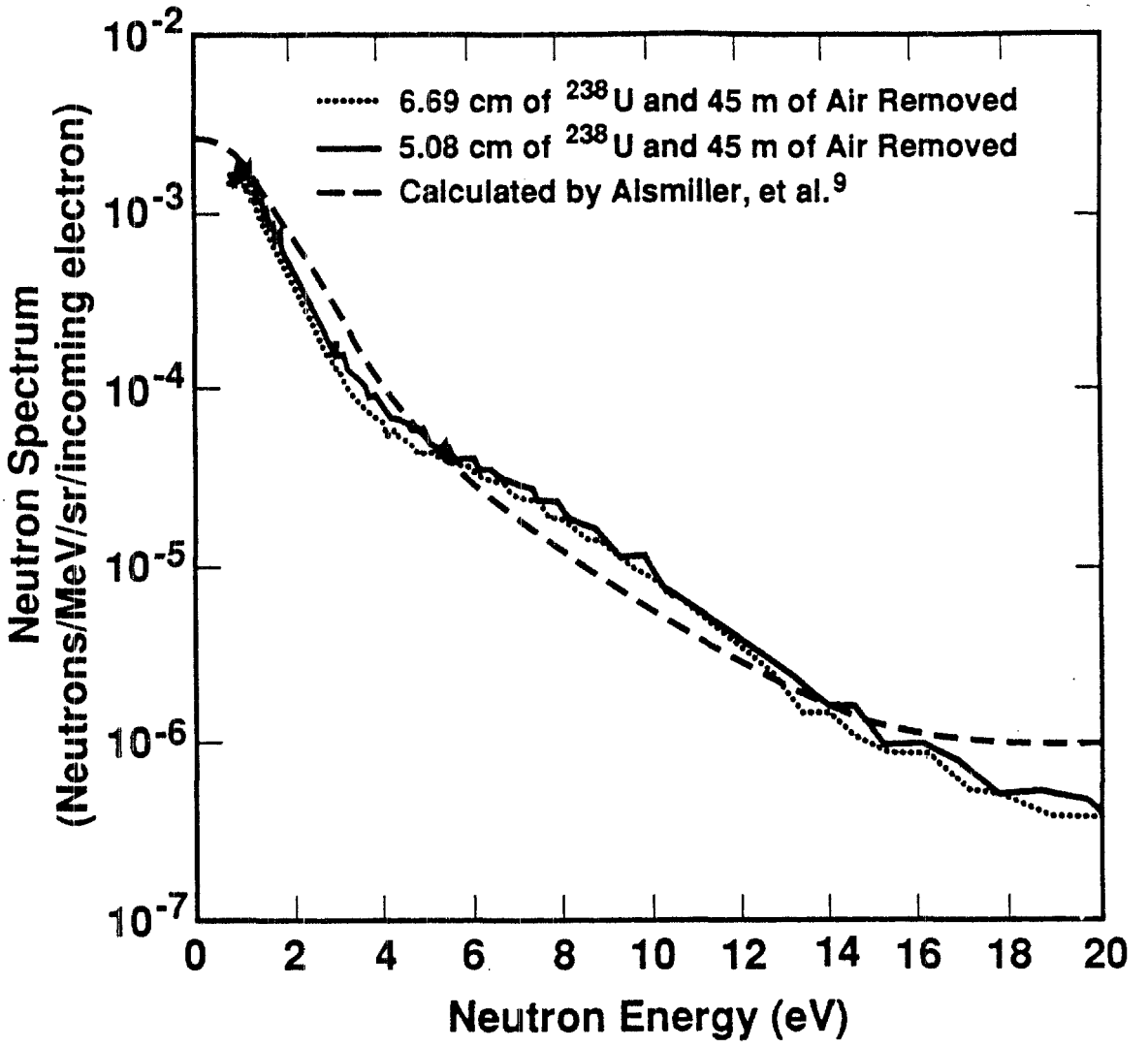

Fig. 9. The calculated and measured fast-neutron energy spectra at ORELA obtained with a Ta target bombarded by 140-MeV electron beam.[10] The dashed line represents the results of the calculations.[9] The solid and dotted lines represent the results of the measurements[10] with corrections to take into account the attenuation of uranium filters and of the air along the flight path.

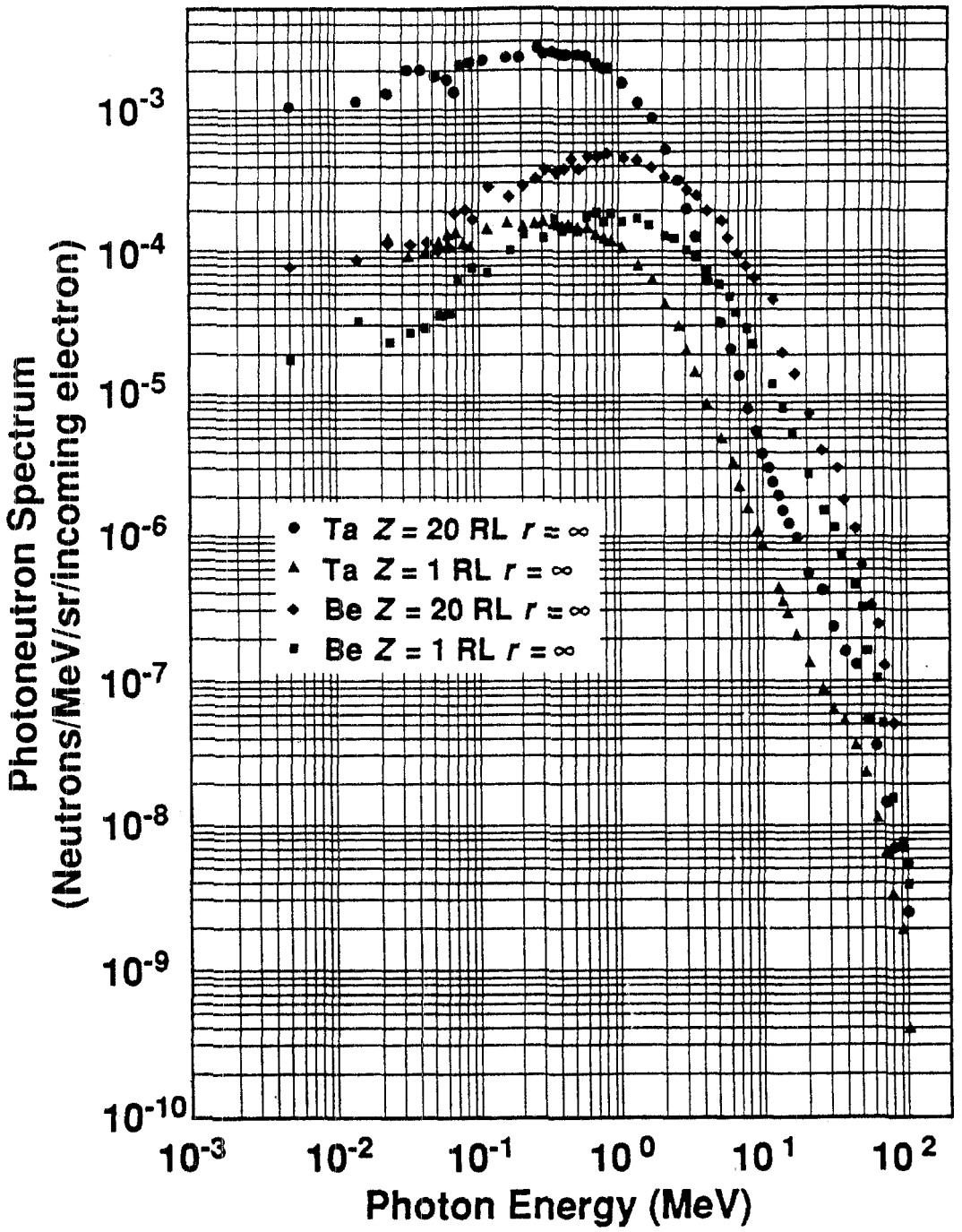

Fig. 10. The calculated fast-neutron spectrum at ORELA with Ta and Be targets bombarded by a 150-MeV electron beam.[9] These targets are supposed to be infinite in the direction perpendicular to that of the incident electron beam ($r = \infty$) but with thicknesses of 1 and 20 radiation lengths (RL) along the direction of the electron beam.

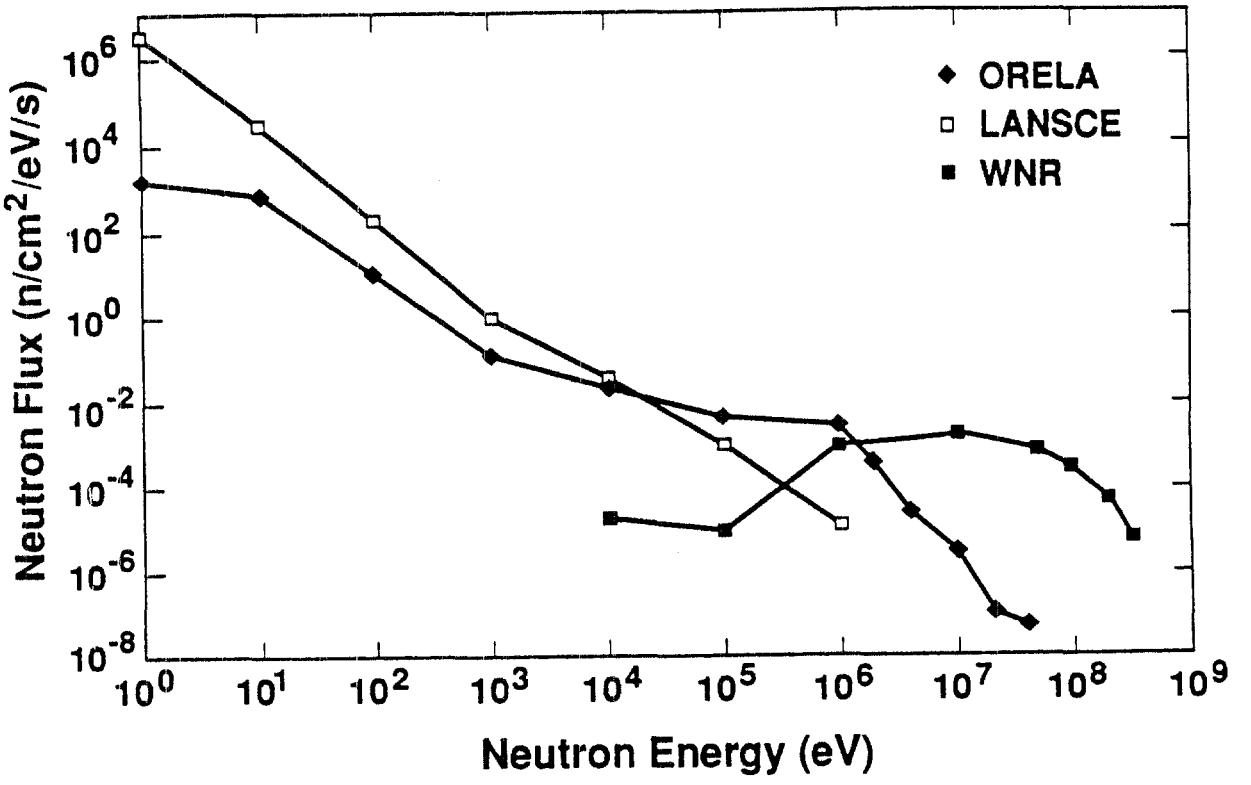

Fig. 11. Neutron flux as a function of neutron energy for the resolution profile RPI (Fig. 7) and for the three facilities: ORELA, LANSCE, and WNR, as they presently exist (A-plot).

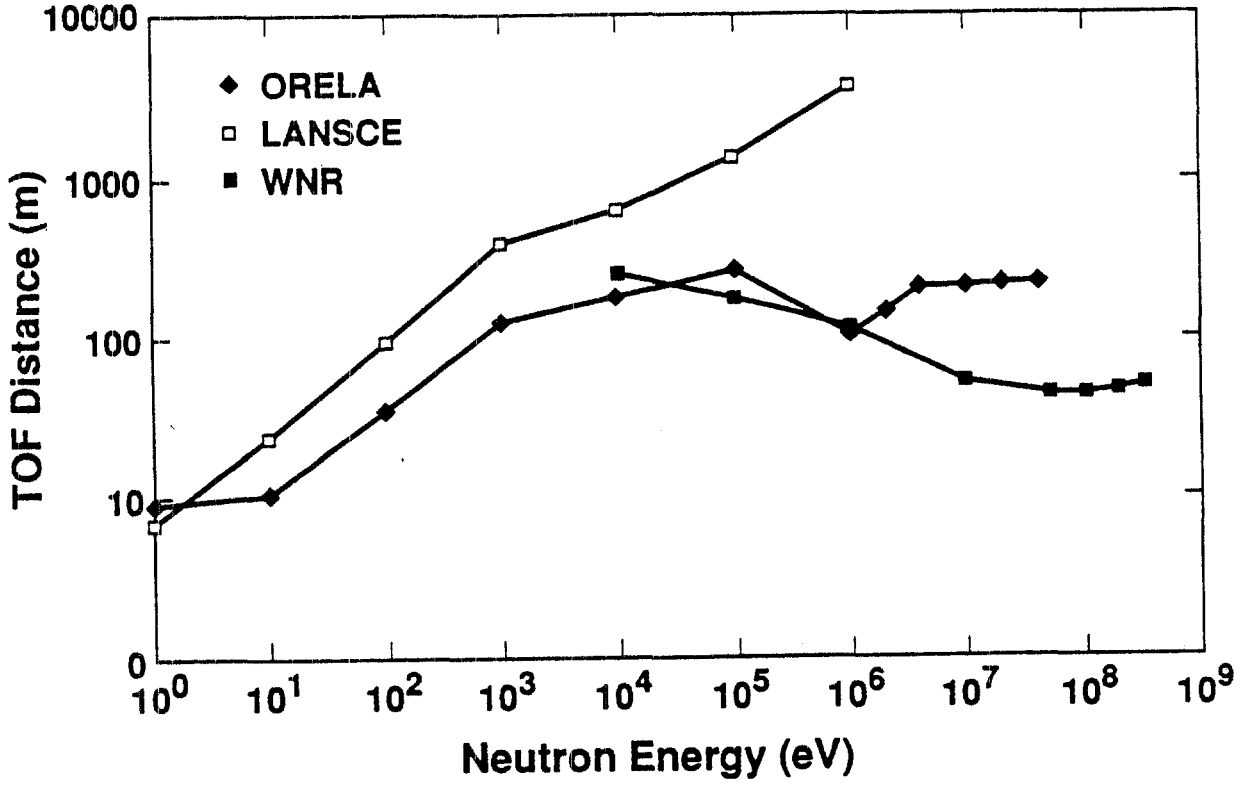

Fig. 12. TOF distance as a function of neutron energy for the resolution profile RP1 (Fig. 7) and for the three facilities: ORELA, LANSCE, and WNR, as they presently exist (A-plot).

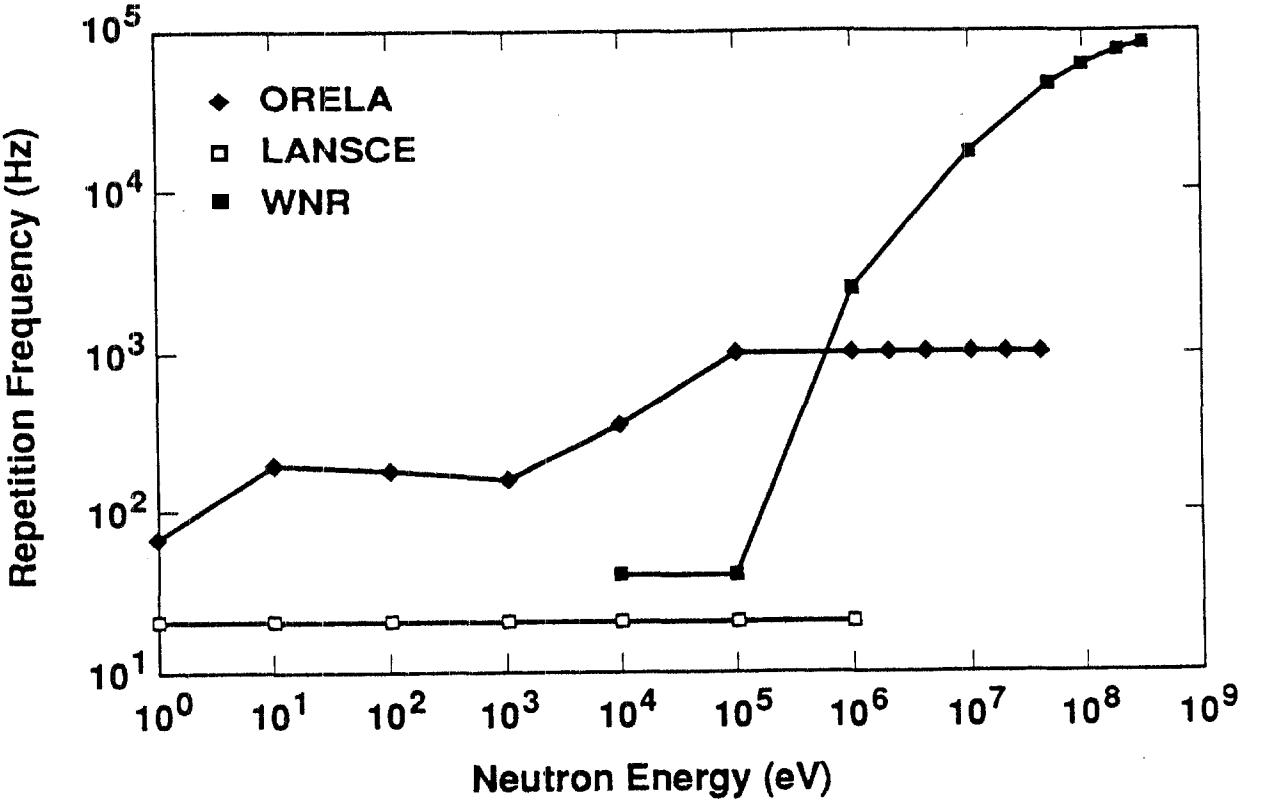

Fig. 13. Repetition frequency as a function of neutron energy for the resolution profile RP1 (Fig. 7) and for the three facilities: ORELA, LANSCE, and WNR, as they presently exist (A-plot).

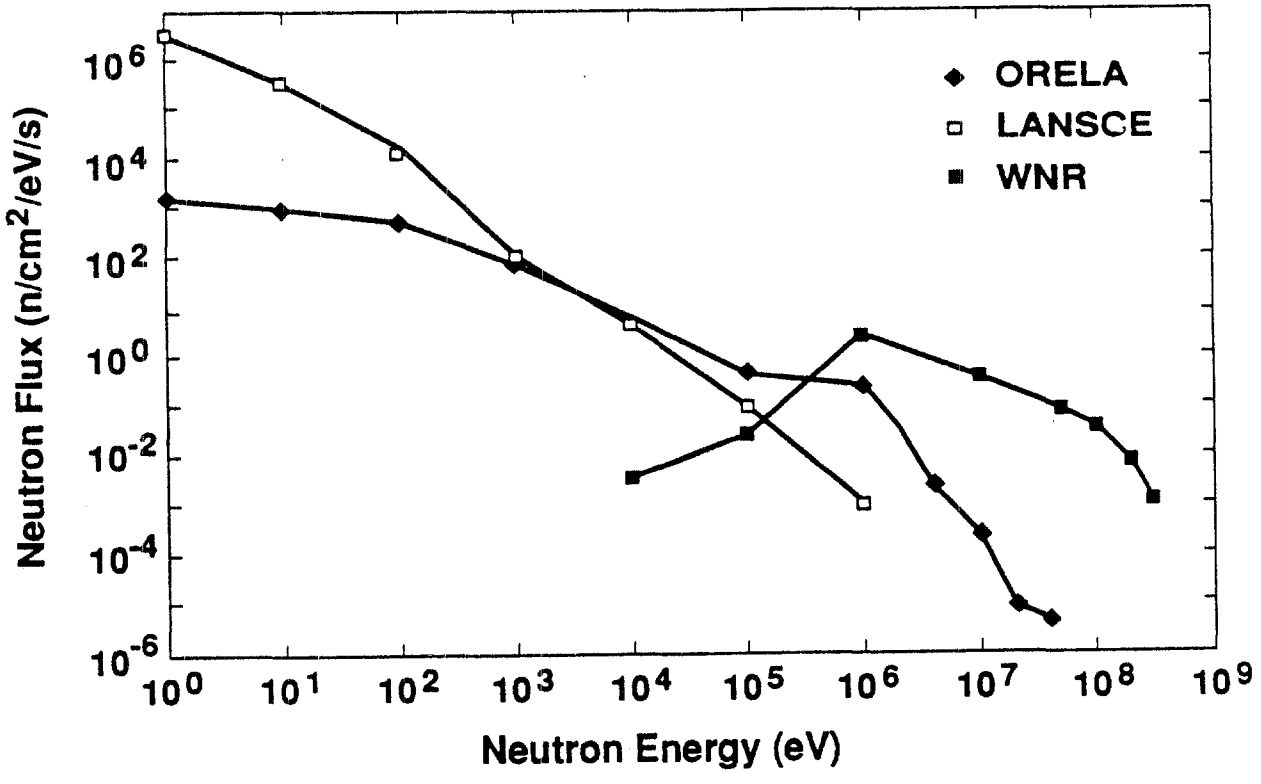

Fig. 14. Neutron flux as a function of neutron energy for the resolution profile RP2 (Fig. 7) and for the three facilities: ORELA, LANSCE, and WNR, as they presently exist (A-plot).

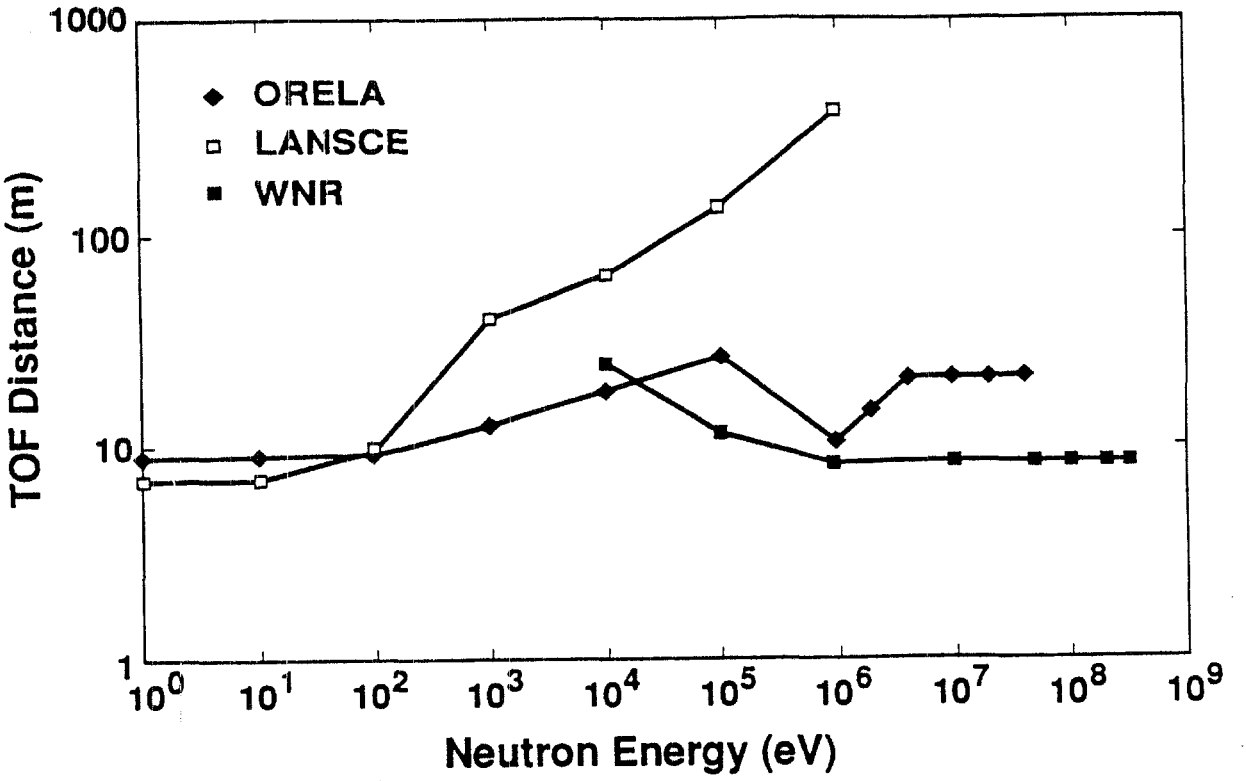

Fig. 15. TOF distance as a function of neutron energy for the resolution profile RP2 (Fig. 7) and for the three facilities: ORELA, LANSCE, and WNR, as they presently exist (A-plot).

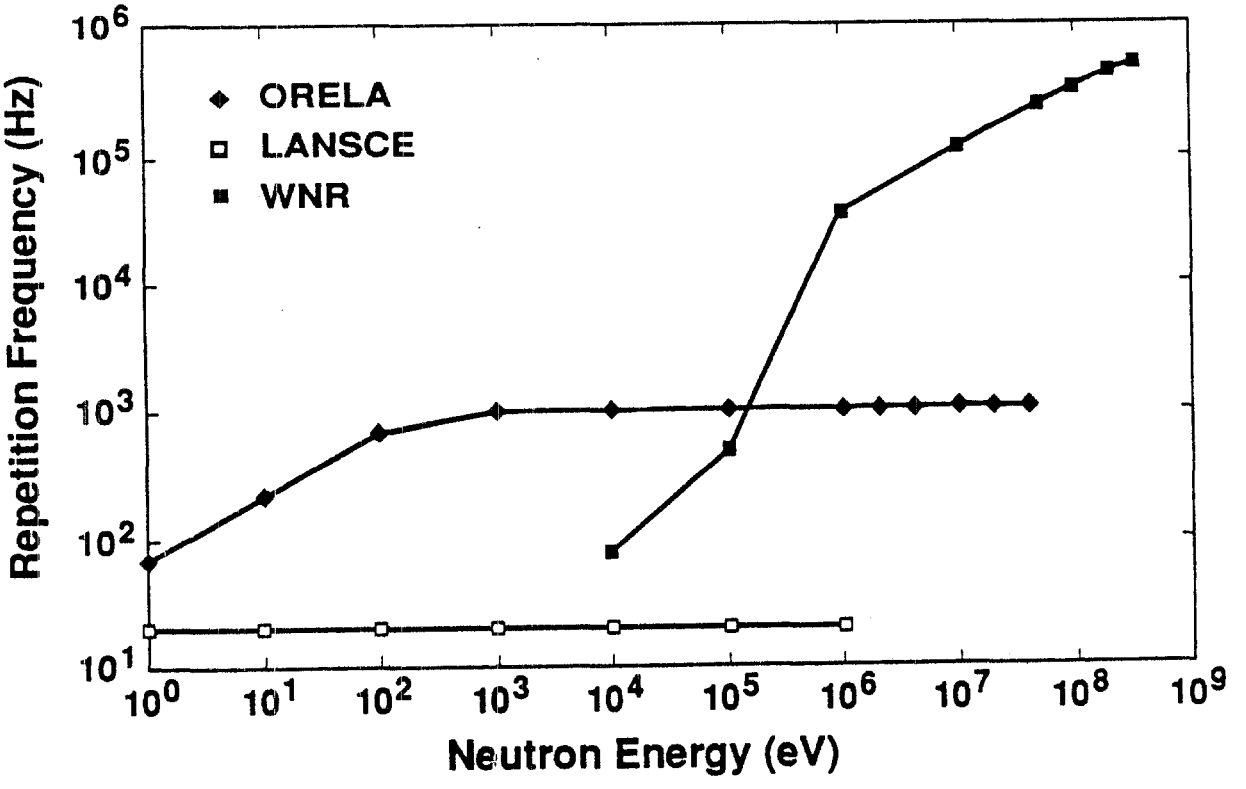

Fig. 16. Repetition frequency as a function of neutron energy for the resolution profile RP2 (Fig. 7) and for the three facilities: ORELA, LANSCE, and WNR, as they presently exist (A-plot).

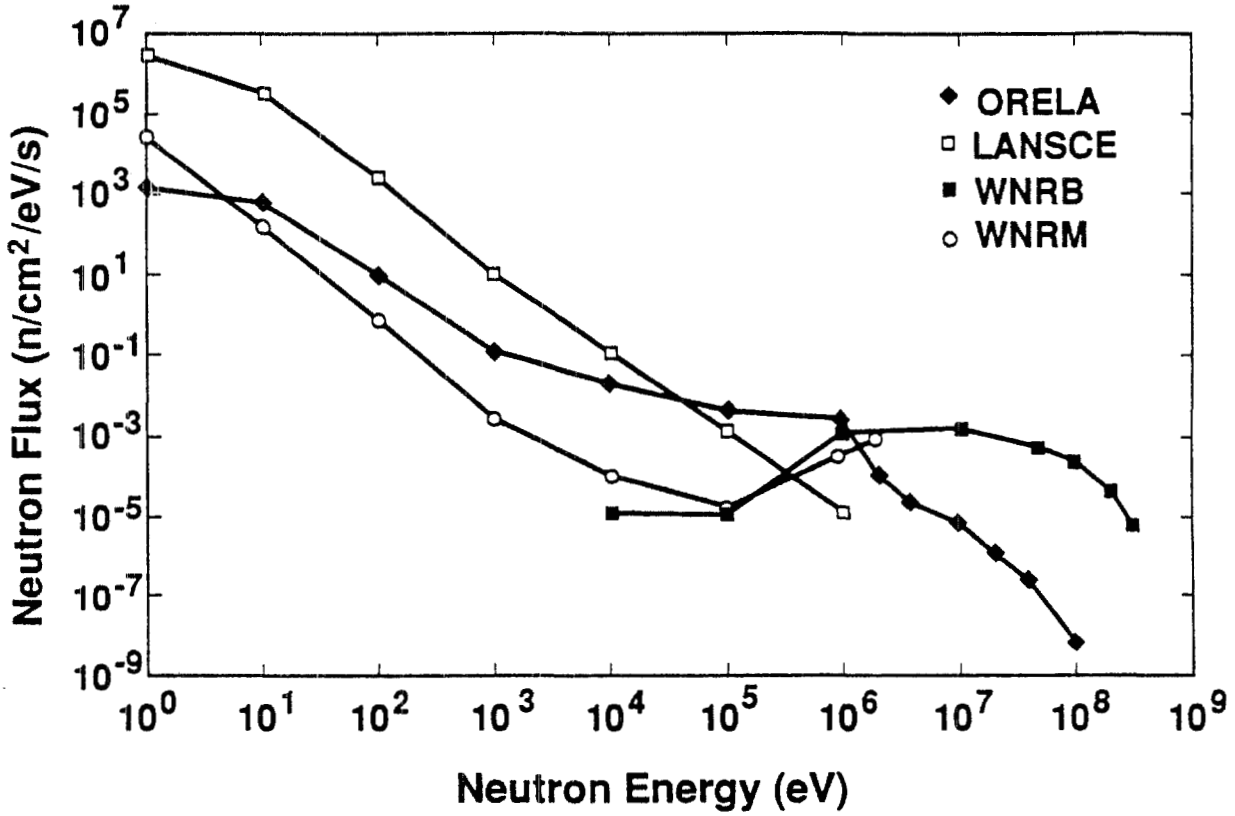

Fig. 17. Neutron flux as a function of neutron energy for the resolution profile RP1 (Fig. 7) and for the three facilities: ORELA, LANSCE, and WNR, slightly upgraded (B-plot).

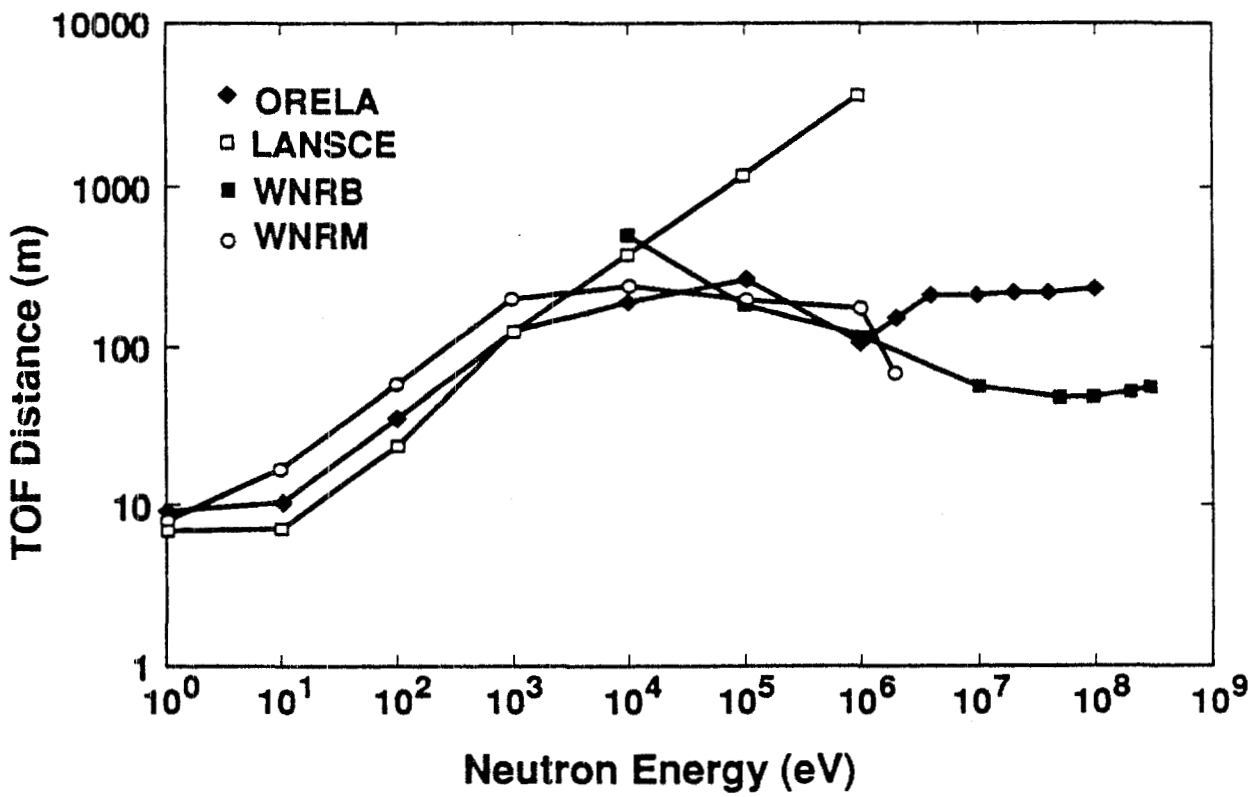

Fig. 18. TOF distance as a function of neutron energy for the resolution profile RP1 (Fig. 7) and for the three facilities: ORELA, LANSCE, and WNR, slightly upgraded (B-plot).

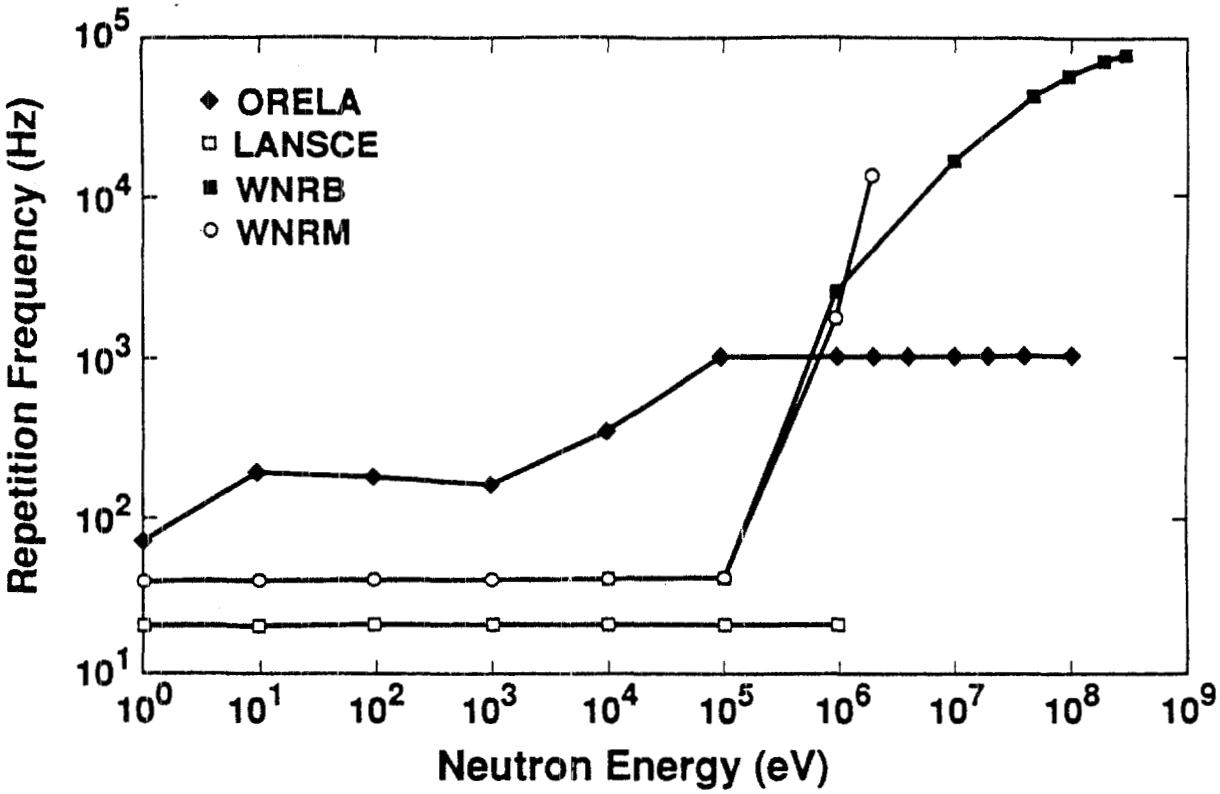

Fig. 19. Repetition frequency as a function of neutron energy for the resolution profile RP1 (Fig. 7) and for the three facilities: ORELA, LANSCE, and WNR, slightly upgraded (B-plot).

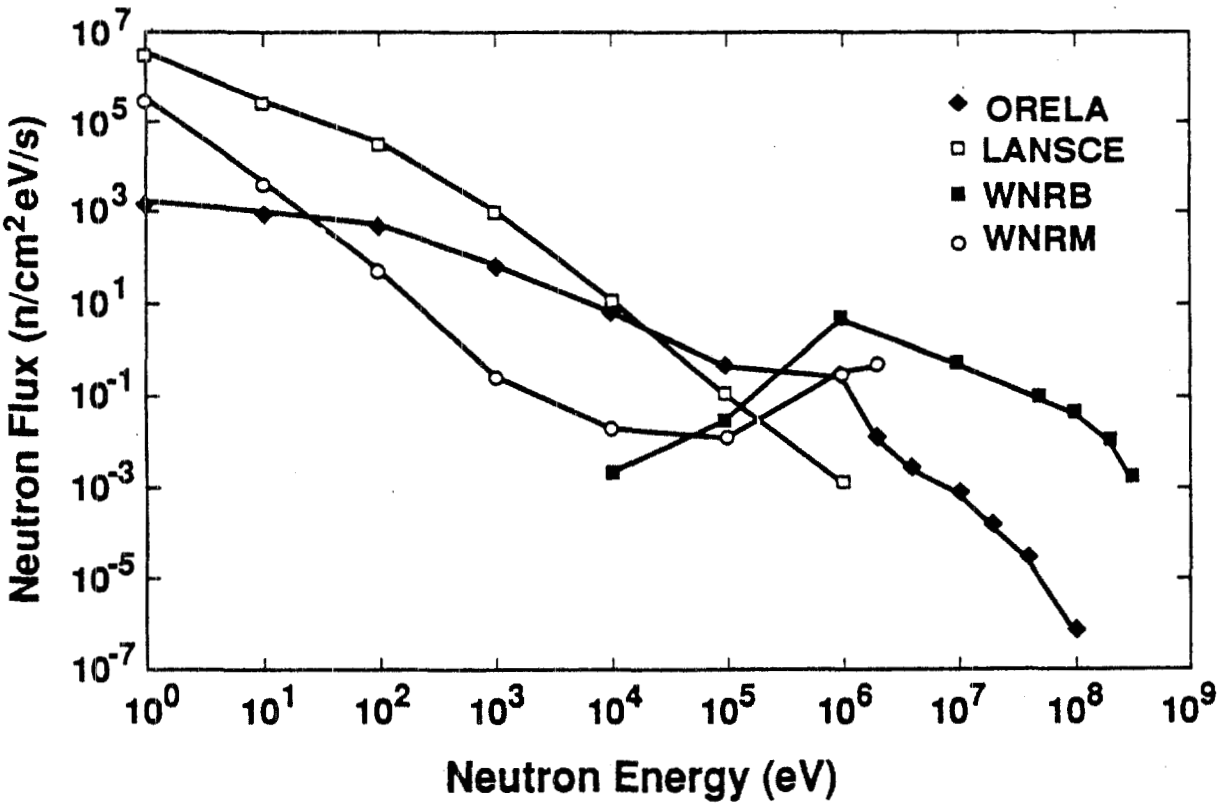

Fig. 20. Neutron flux as a function of neutron energy for the resolution profile RP2 (Fig. 7) and for the three facilities: ORELA, LANSCE, and WNR, slightly upgraded (B-plot).

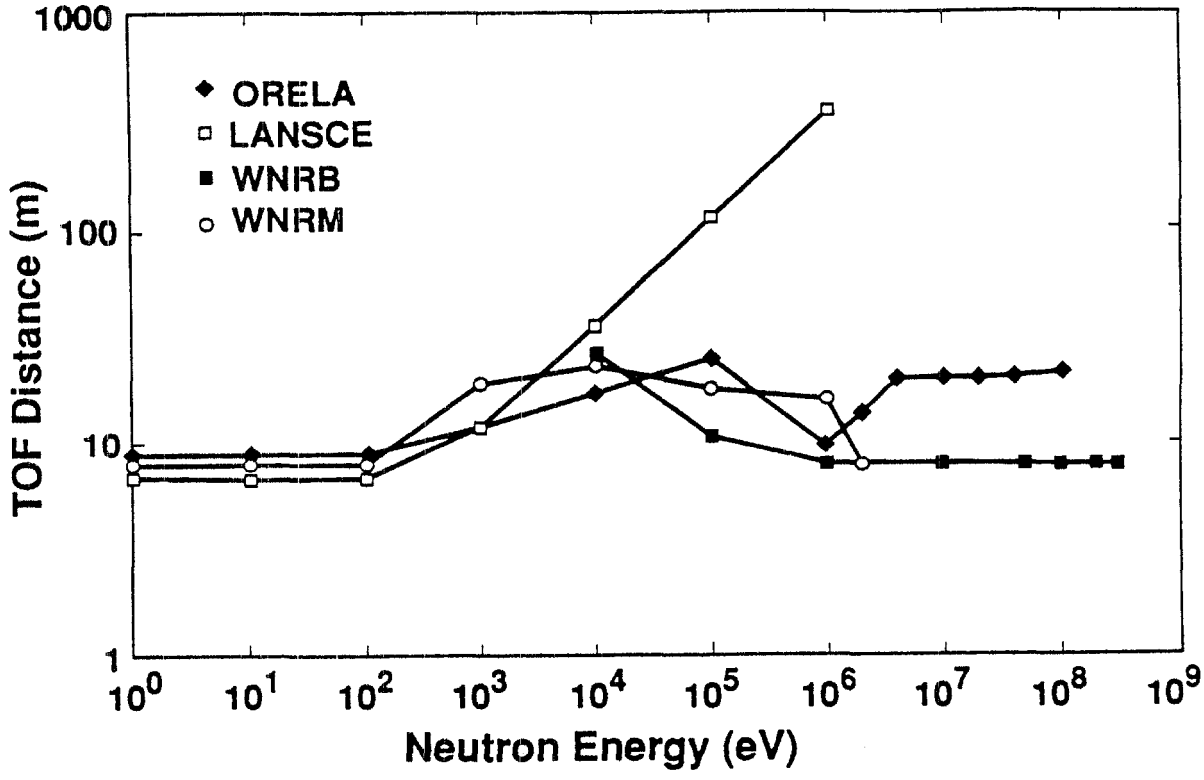

Fig. 21. TOF distance as a function of neutron energy for the resolution profile RP2 (Fig. 7) and for the three facilities: ORELA, LANSCE, and WNR, slightly upgraded (B-plot).

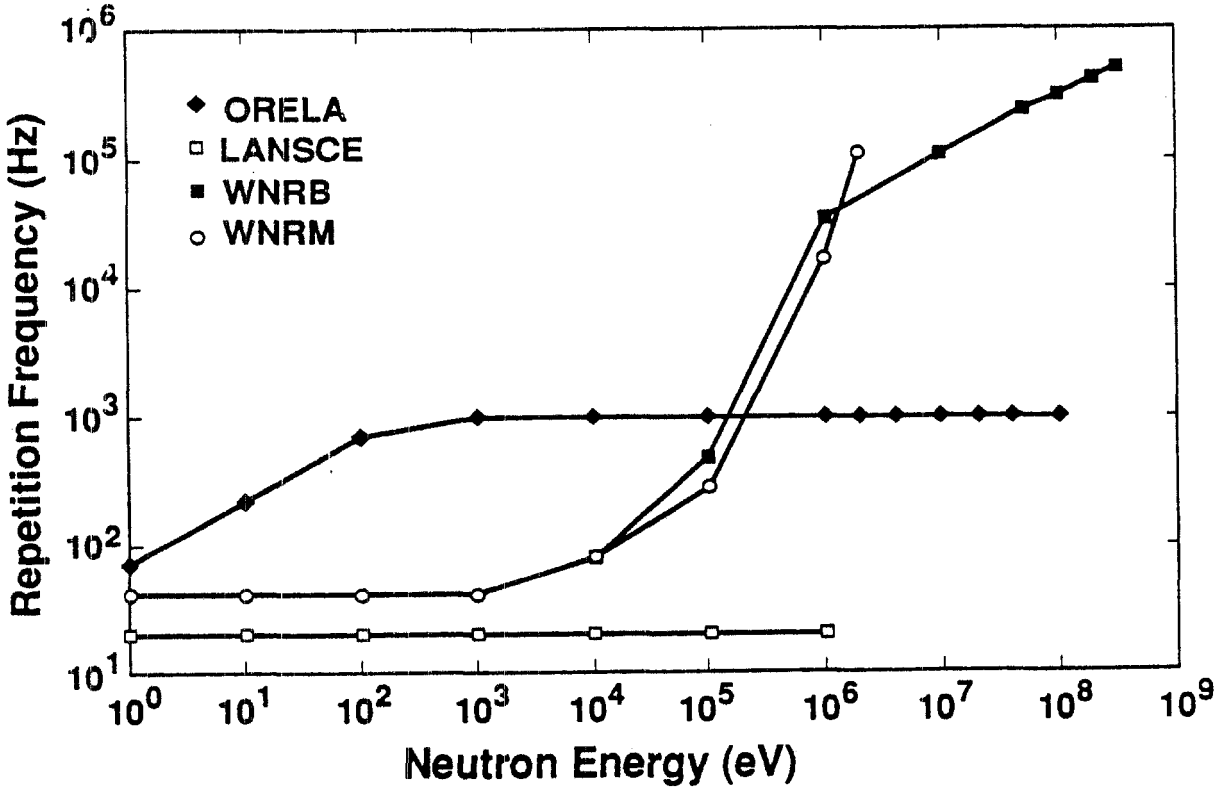

Fig. 22. Repetition frequency as a function of neutron energy for the resolution profile RP2 (Fig. 7) and for the three facilities: ORELA, LANSCE, and WNR, slightly upgraded (B-plot).

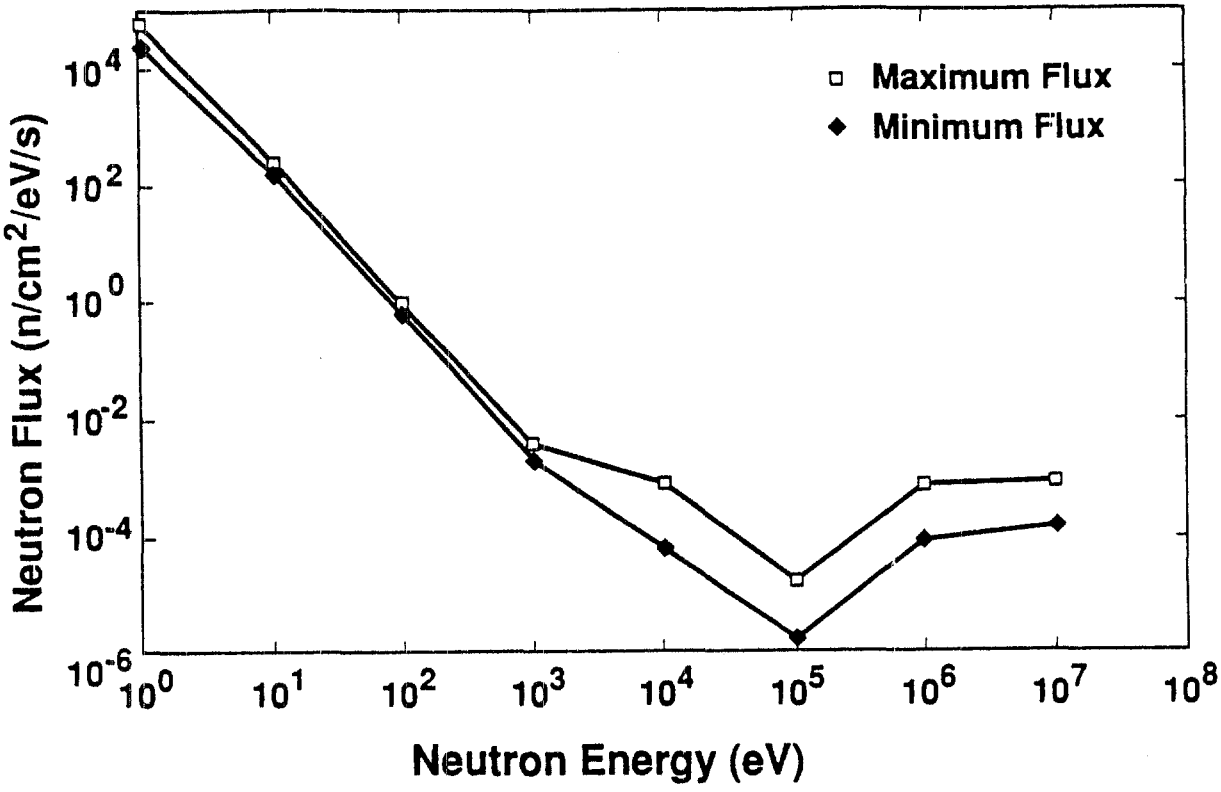

Fig. 23. Comparison of WNRM targets in terms of the maximum and minimum neutron fluxes obtained with all the WNRM targets considered in the calculations.

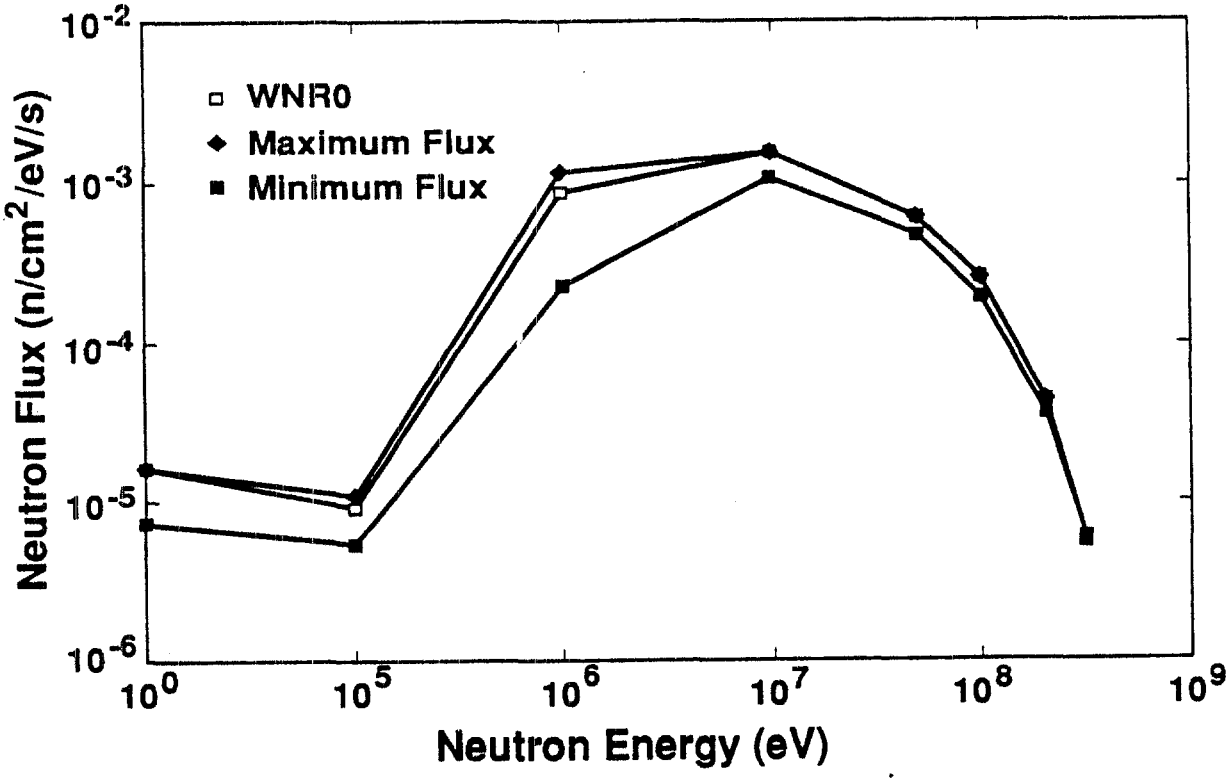

Fig. 24. Comparison of WNRB targets in terms of the maximum and minimum neutron fluxes obtained with all the WNRB targets considered in the calculations. The neutron flux obtained with the WNRO target (presently used at WNR) is also plotted for comparison.

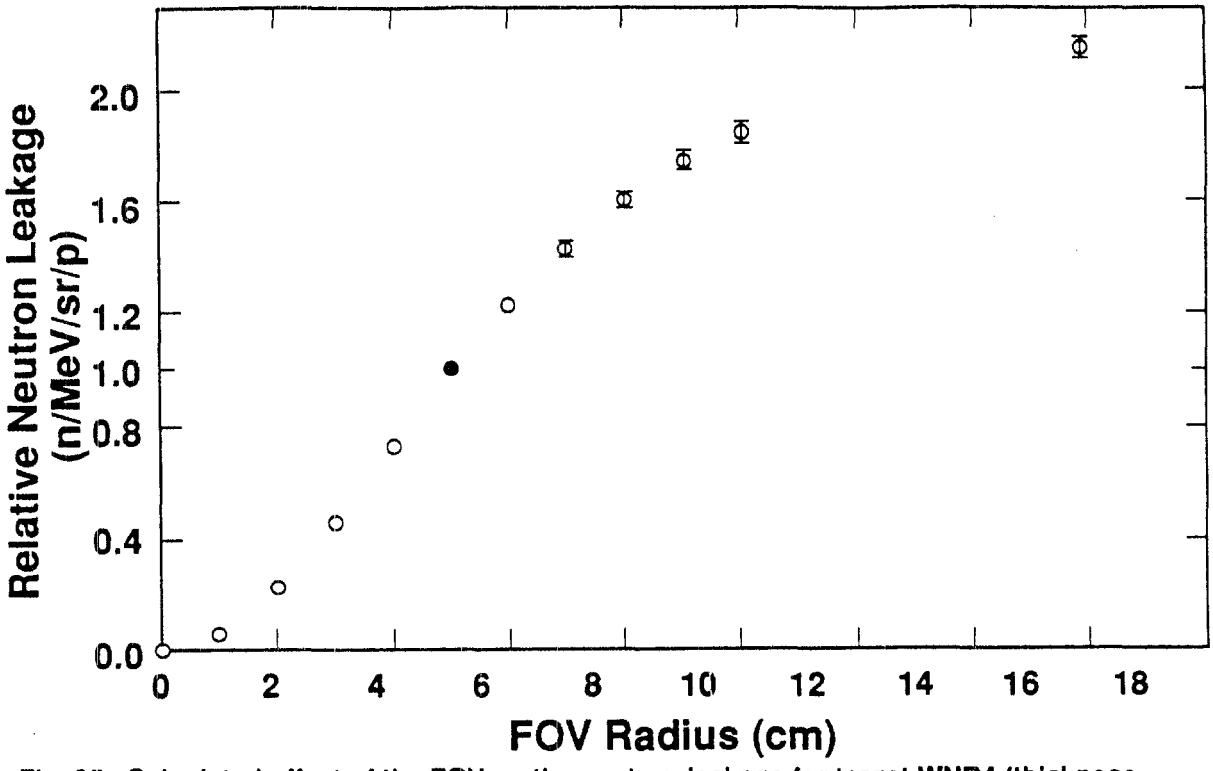

Fig. 25. Calculated effect of the FOV on the neutron leakage for target WNR4 (thickness of 5 cm). The FOV is supposed to be circular, and the neutron leakage is plotted as a function of the FOV radius. The neutron leakage is normalized to that for a FOV radius of 5 cm (the maximum FOV available at WNR).

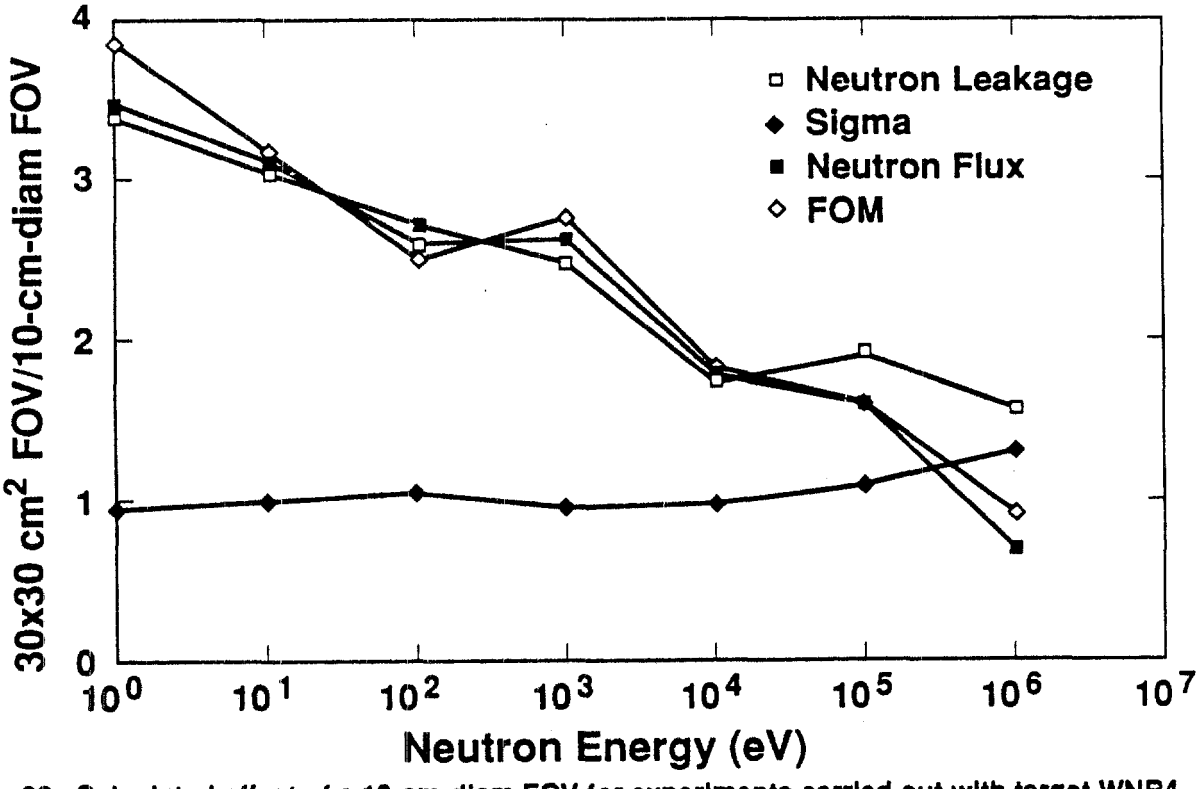

Fig. 26. Calculated effect of a 10-cm-diam FOV for experiments carried out with target WNR4 (thickness of 5 cm). This effect is calculated by making the ratios of the neutron leakage, the standard deviation of the neuton time distribution, the neutron flux, and the figure of merit (defined in the text), as calculated with a fully open FOV of 30 x 30 cm^2 to those obtained with a 10-cm-diam FOV, respectively. The calculations are made for the resolution profile RP1.

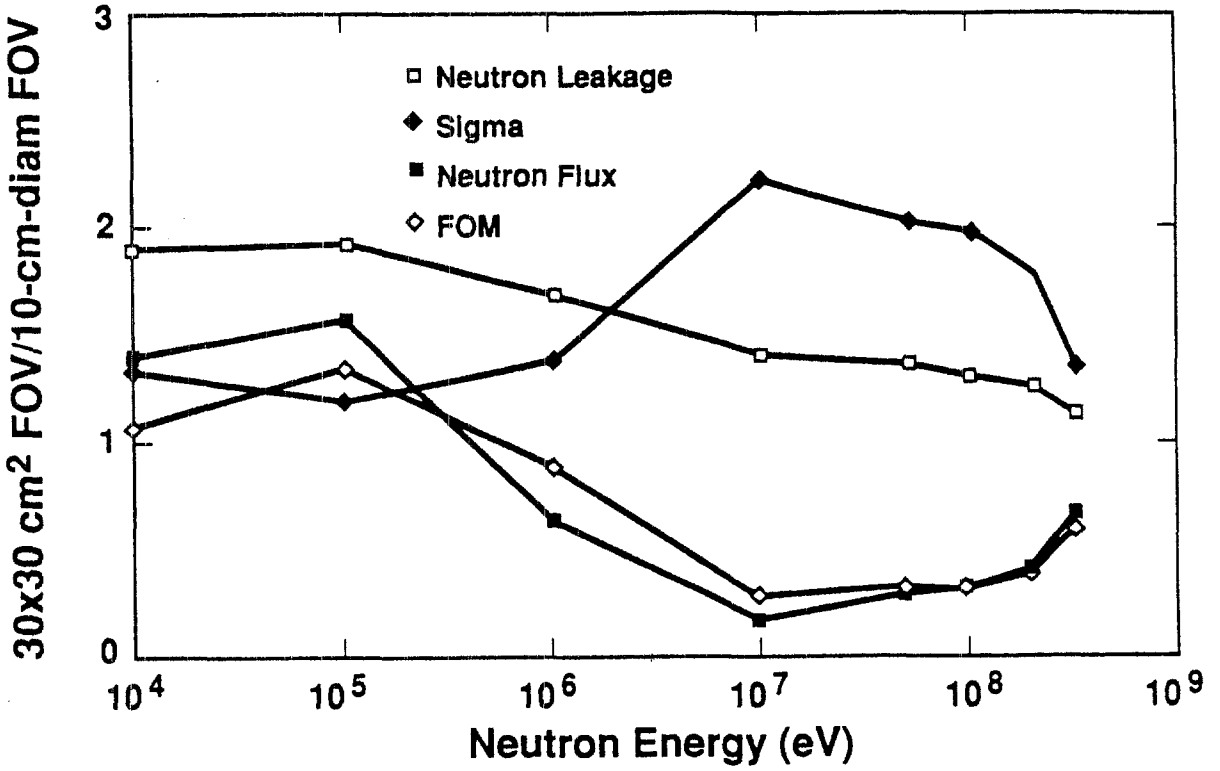

Fig. 27. Calculated effect of a 10-cm-diam FOV for experiments carried out with target WNR3 (thickness of 5 cm). This effect is calculated by making the ratio of the neutron leakage, the standard deviation of the neutron time distribution, the neutron flux, and the figure of merit (defined in the text), as calculated with a fully open FOV of 30 x 30 cm^2 to those obtained with a 10-cm-diam FOV, respectively. The calculations are made for the resolution profile RP1.

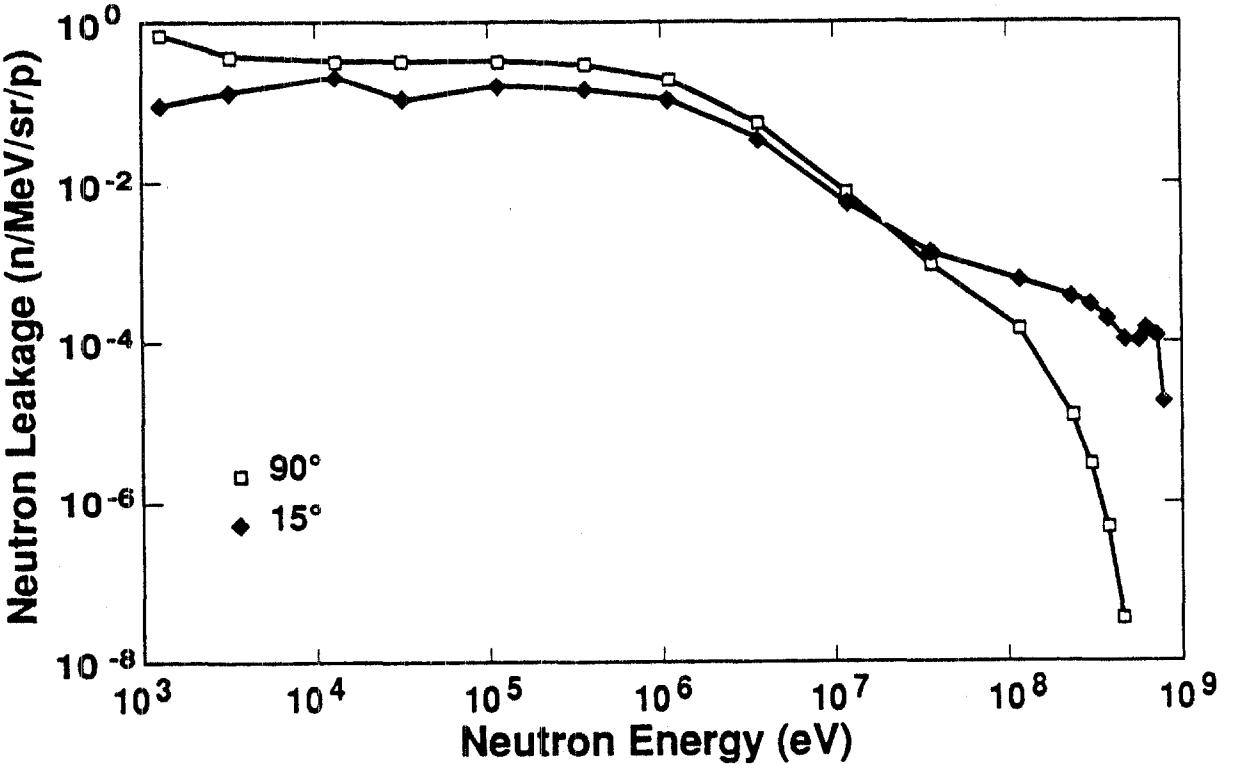

Fig. 28. Effect of the emission angle on the neutron spectrum. This figure represents the calculated neutron energy spectra for target WNR0 (presently used at WNR) at 90° and 15° relative to the incident proton beam.

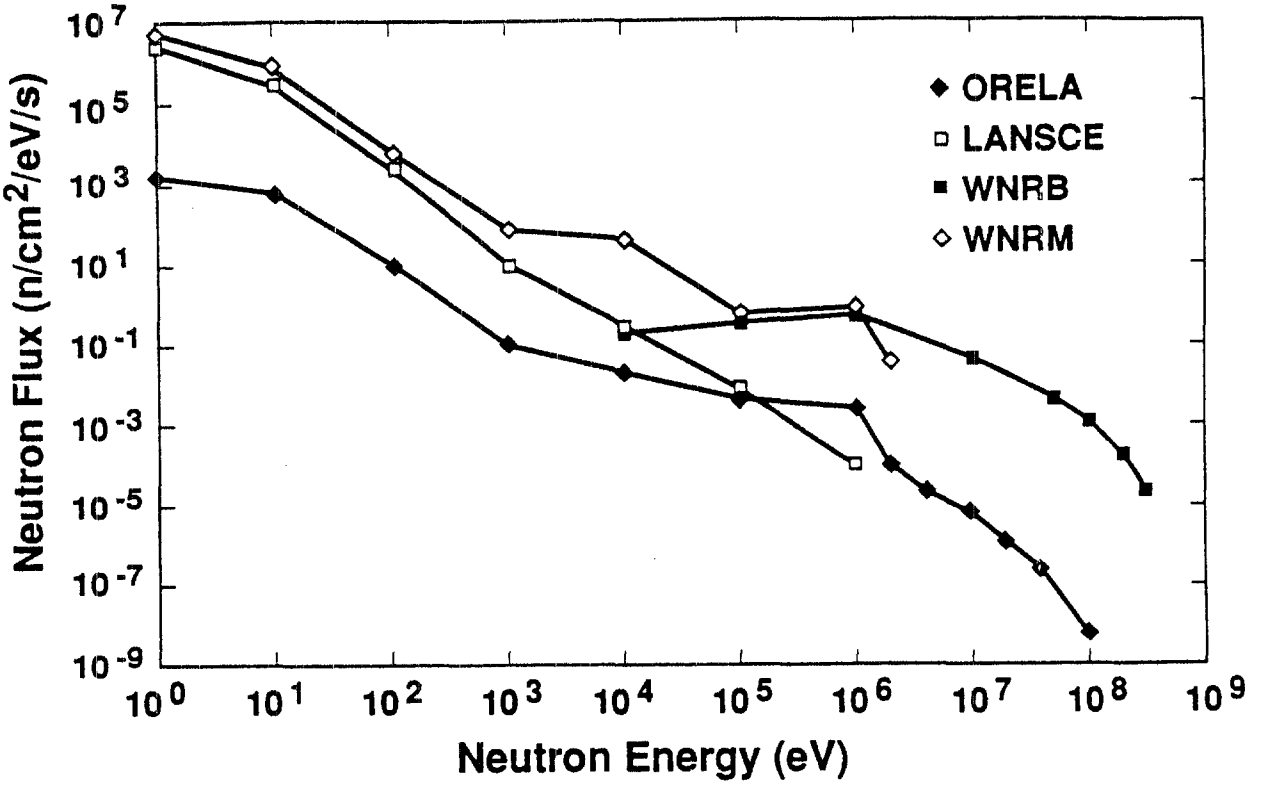

Fig. 29. Neutron flux as a function of neutron energy for the resolution profile RP1 (Fig. 7) and for the three facilities: ORELA, LANSCE, and WNR, upgraded as described in the text (C-plot).

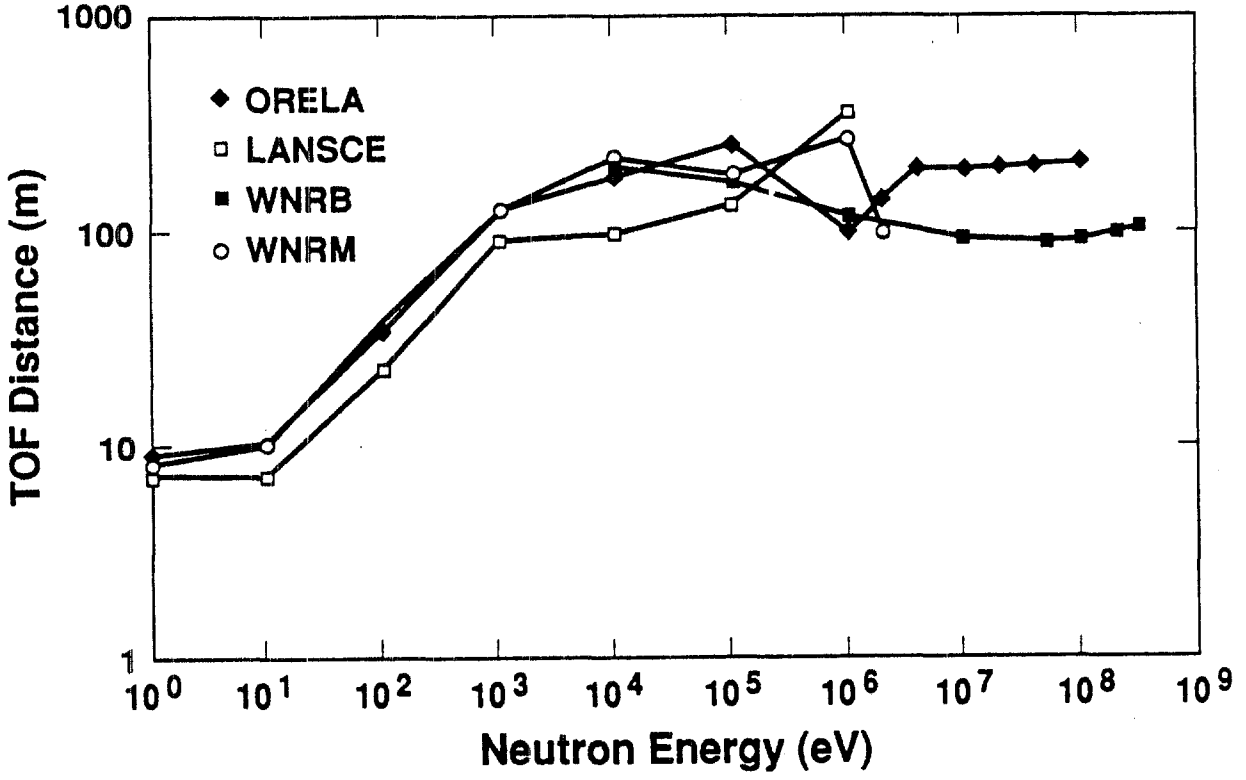

Fig. 30. TOF distance as a function of neutron energy for the resolution profile RP1 (Fig. 7) and for the three facilities: ORELA, LANSCE, and WNR, upgraded as described in the text (C-plot).

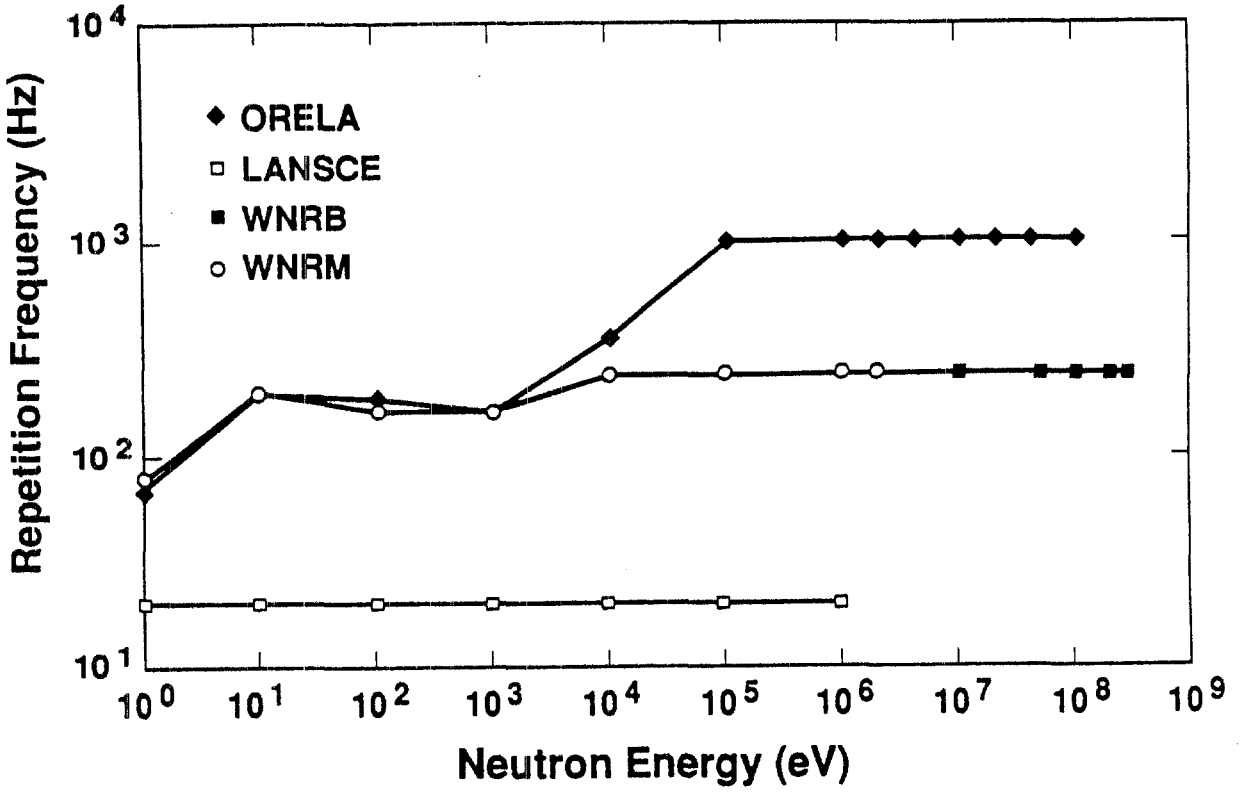

Fig. 31. Repetition frequency as a function of neutron energy for the resolution profile RP1 (Fig. 7) and for the three facilities: ORELA, LANSCE, and WNR, upgraded as described in the text (C-plot).

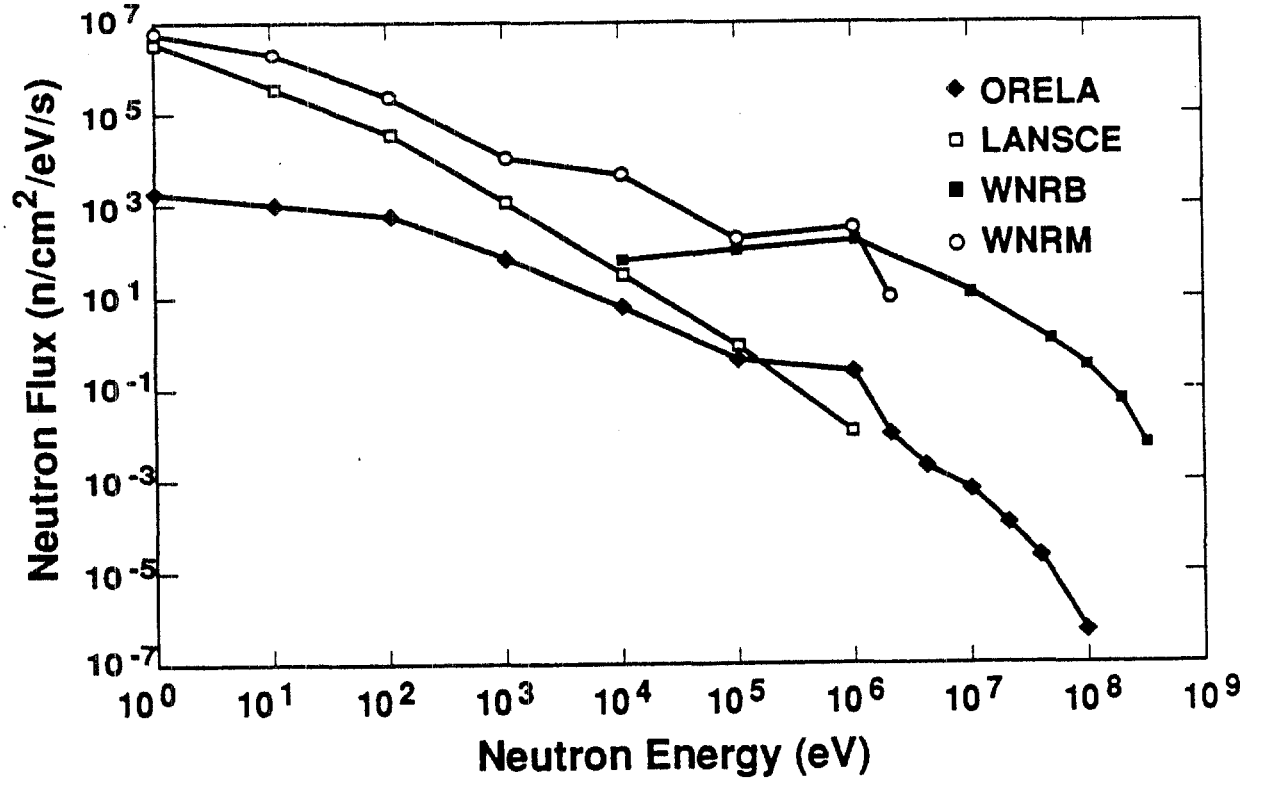

Fig. 32. Neutron flux as a function of neutron energy for the resolution profile RP2 (Fig. 7) and for the three facilities: ORELA, LANSCE, and WNR, upgraded as described in the text (C-plot).

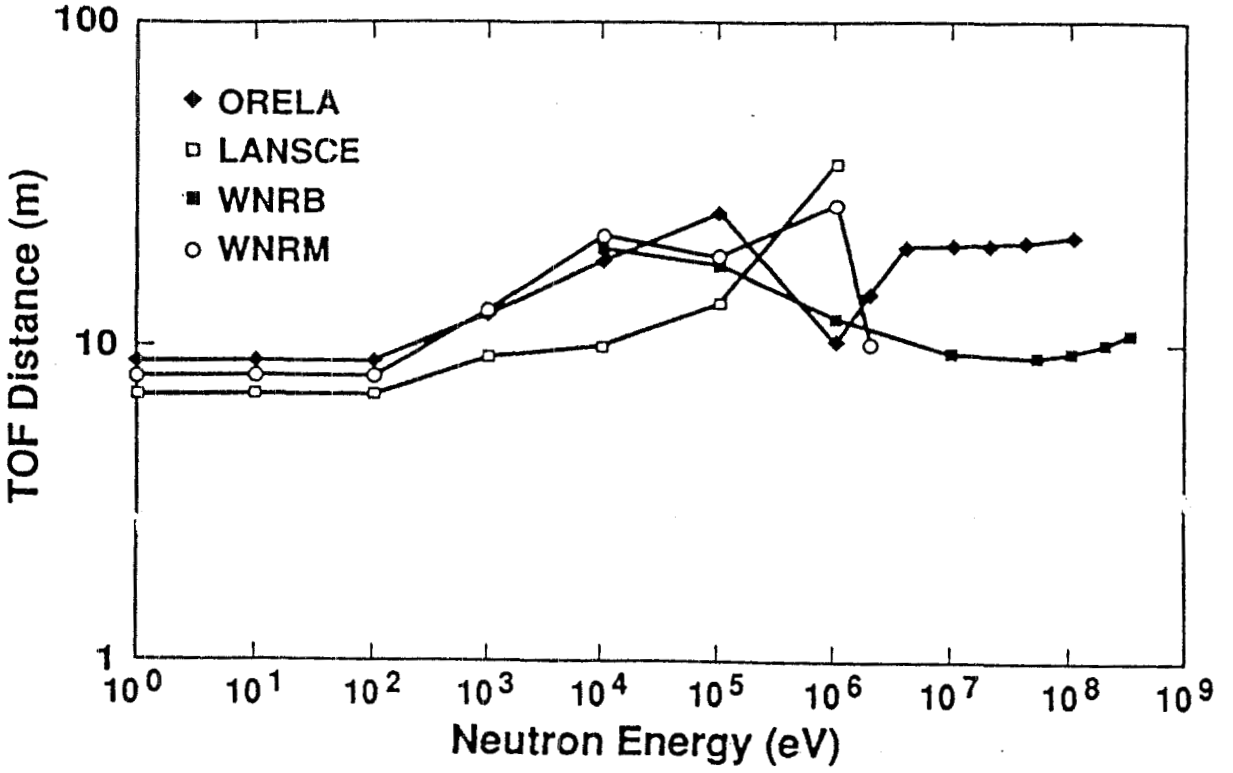

Fig. 33. TOF distance as a function of neutron energy for the resolution profile RP2 (Fig. 7) and for the three facilities: ORELA, LANSCE, and WNR, upgraded as described in the text (C-plot).

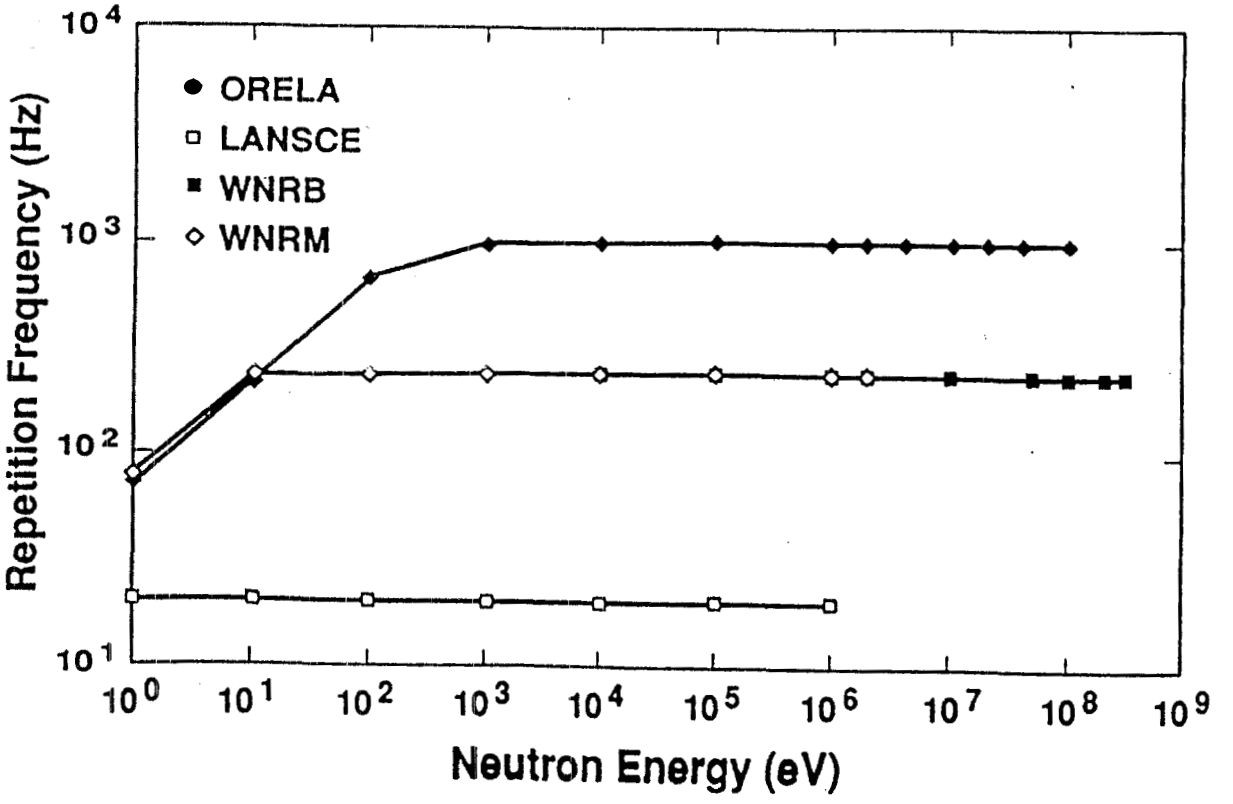

Fig. 34. Repetition frequency as a function of neutron energy for the resolution profile RP2 (Fig. 7) and for the three facilities: ORELA, LANSCE, and WNR, upgraded as described in the text (C-plot).

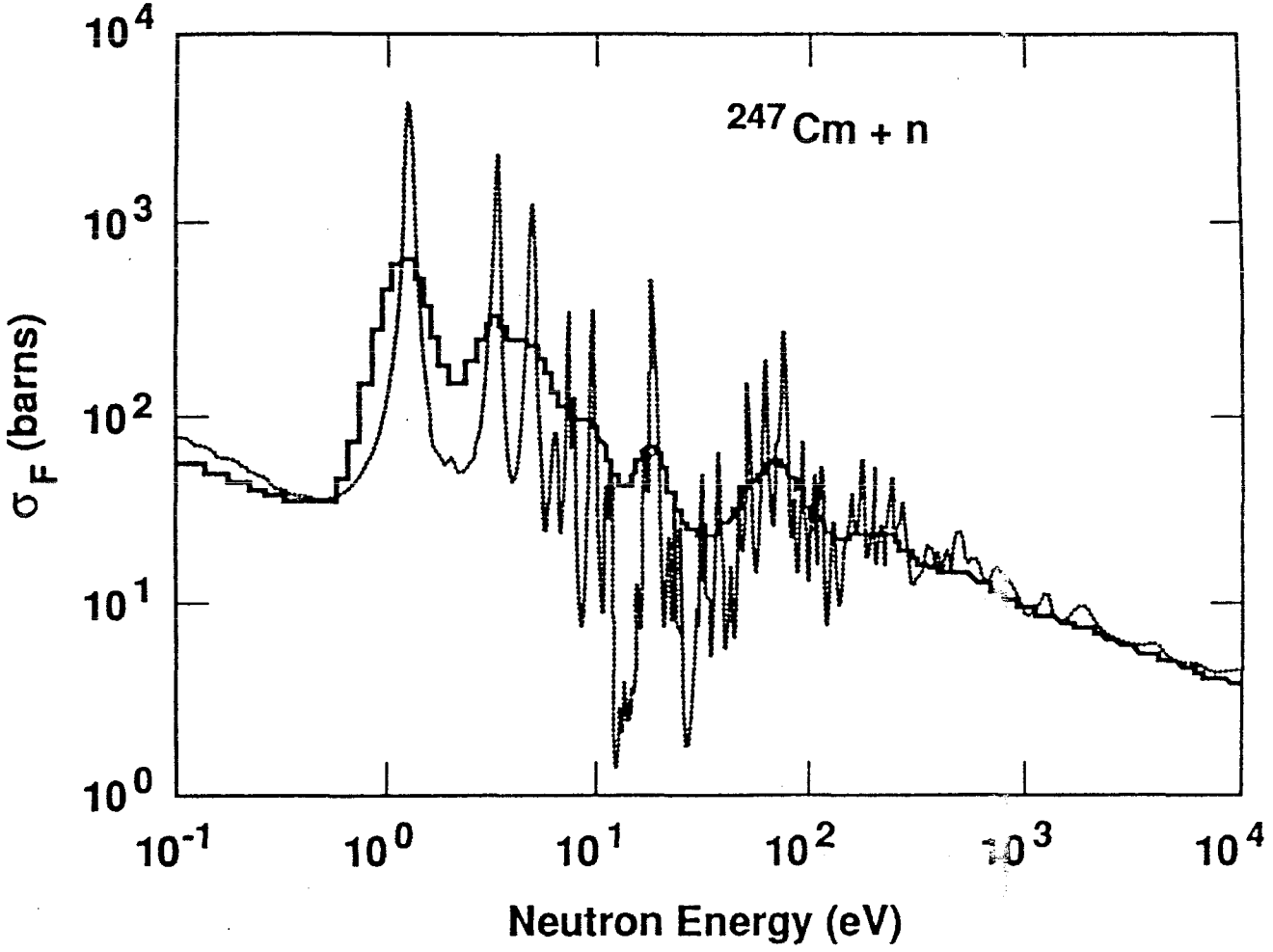

Fig. 35. Neutron-induced fission cross section of ^{247}Cm between 0.1 eV and 10 keV, as measured with the same fission chamber with the RINS at RPI (solid line) and in a conventional geometry at LANSCE (dotted line).[15]